2017-03-09

Small Deformation Detected from InSAR Time-Series and Their Applications in Geophysics

Wenliang Zhao
University of Miami, wenliang.zhao.nyu@gmail.com

UNIVERSITY OF MIAMI

SMALL DEFORMATION DETECTED FROM INSAR TIME-SERIES AND THEIR APPLICATIONS IN GEOPHYSICS

By
Wenliang Zhao

A DISSERTATION

Submitted to the Faculty
of the University of Miami
in partial fulfillment of the requirements for
the degree of Doctor of Philosophy

Coral Gables, Florida

May 2017

UNIVERSITY OF MIAMI

A dissertation submitted in partial fulfillment of
the requirements for the degree of
Doctor of Philosophy

SMALL DEFORMATION DETECTED FROM INSAR TIME-SERIES AND THEIR APPLICATIONS IN GEOPHYSICS

Wenliang Zhao

Approved:

_____ Falk Amelung, Ph.D. Professor of Marine Geosciences	_____ Shimon Wdowinski, Ph.D. Professor of Marine Geosciences
_____ Guoqing Lin, Ph.D. Associate Professor of Marine Geosciences	_____ Guillermo J. Prado, Ph.D. Dean of the Graduate School

_____
Timothy H. Dixon, Ph.D.
Professor of Geophysics
University of South Florida

ZHAO, WENLIANG (Ph.D., Marine Geology and Geophysics)
Small Deformation Detected from InSAR Time-Series and Their Applications in Geophysics (May 2017)

Abstract of a dissertation at the University of Miami.

Dissertation supervised by Professor Falk Amelung.
No. of pages in text. (139)

InSAR has been proved to be useful for detecting large scale small surface motion from space. For a series of environmental phenomenon and their associated geomechanical processes, new insights are obtained from spatio-temporal information provided by InSAR. However, for some applications, how to get reliable deformation signal, how to use these information, and how to build the mechanical models remain some questions. For ice mass loss estimation problem, it is easy to build a linear inverse model from observed deformation. Unfortunately, this model is highly under-determined, which means the places far from the ice margin are usually poorly constrained while the places close to the ice margin are underestimated. For present-day hydraulic fracturing problem, only the upper crust is sensitive to the load change. But the existing global 1-D earth models usually have a coarse resolution in crust. Moreover, these models are typically from seismic wave velocities representing the dynamic moduli instead of the static moduli required for the hydraulic fracturing modeling. For geological carbon sequestration study, there was one successful attempt based on InSAR in the desert in 2008 and almost no new result comes out after that.

The main problem is that most carbon sequestration projects are located in rural areas where less stable reflection targets can be found.

In this dissertation I will try to answer the questions listed above. I will discuss two different methods solving the under-determined linear inverse problem for ice mass loss estimation in chapter 2 and 3. For the second question, I will discuss two different test sites and their crustal elasticity in chapter 4 and 5. In chapter 6 I will discuss the development of a time-series analysis method for retrieving small surface deformation at carbon sequestration injection sites in north America.

Table of Contents

List of Figures

List of Tables

Chapter 1

Introduction

1.1. Background

Developed in 1970s [*Graham*, 1974], repeat-pass synthetic aperture radar interferometry (InSAR) was a technique retrieves surface topography at large scale (hundreds of kilometers) and high resolution (several tens of meters). By subtracting an existing digital model (DEM), the differential InSAR (D-InSAR) technique was used to measure centimeter level surface motions such as co-seismic deformation [*Massonnet et al.*, 1993] and volcanic eruption [*Amelung et al.*, 2000]. In early 2000s, time-series analysis analysis algorithms [*Ferretti et al.*, 2000; *Berardino et al.*, 2002] significantly increased the accuracy of InSAR products to 1-2 cm. More developments [*Hooper et al.*, 2006; *Hong et al.*, 2008] based on these algorithms further pushed the frontier of InSAR study to detecting smaller geomechanical signals, and after late 2000s, the InSAR community started to focus on sub-centimeter surface deformation [*Zhao et al.*, 2014] and time-dependent modeling [*Chaussard et al.*, 2014].

Because of the unprecedented sensitivity to surface movements based on these techniques, new applications and models in geophysics can be potentially developed. In this dissertation, we discuss 5 different applications on ice mass balance estimation, effective firn density constraining, earth's rheology constraining, and carbon sequestration (CCS) sites monitoring. In some applications, we make fundamental contributions by defining completely new models. In other applications, we modify previous methods in order to satisfy the local environmental and data requirements.

1.2. Objectives

Space geodetic techniques commonly used to estimate ice mass loss are the GRAvity and Climate recovery Experiment (GRACE), laser and radar altimetry, and InSAR. The study of using bed-rock deformation measured from InSAR to estimate the ice loss on ice-sheets started since *Liu et al.* [2012], who use 5 years Radarsat-1 data and stacking method to generate radar line-of-sight (LOS) velocity. The major challenge is there is no observation on the ice sheet, so that the places far from the ice margin are poorly constrained represented by an under-determined system in the inversion. The solution suggested by *Liu et al.* [2012] is to introduce a penalty function regularizing the neighboring smoothness of each ice block. In my dissertation, I am going to introduce two different methods solving this problem. The first method is based on an assumption of the spatial distribution of thinning rates – we define the thinning rate following an exponential law as a function of distance from the ice margin.

The inverse problem becomes over-determined based on this assumption. The second method is based on a series of constraints added into the linear system. The first constraint is implemented by a quadtree down sampling in order to reduce the model complexity especially at the center of the load. The second constraint is a modified penalty function controlling the local smoothness of the ice thinning rates. The last constraint is for the variability of thinning rates and total ice loss inferred from altimetry and gravity products. I tested this method on simulation data and will apply it to Barnes ice cap, Canada.

Ice mass balance is combined process including dynamic ice motion, runoff due to melting, evaporation/sublimation, snow accumulation. The ice thinning rate is also affected by firn compaction, glacial isostatic adjustment which are uncorrelated to mass loss. All these processes lead to an effective density for the elevation change [*Li and Zwally*, 2011]. Several climate models are used to build the model of density, such as Box [*Box*, 2013; *Box et al.*, 2013], MAR [*Fettweis et al.*, 2011], RACMO2 [*Ettema et al.*, 2009] and HIRHAM [*Christensen et al.*, 2006]. And several firn models are suggested by Li and Zwally [2011], Zwally et al. [2011], Khan et al. [2014]. However, there is no existing method to validate these models. For InSAR based ice loading/unloading problem, when displacement, volume change and earth model are fixed, the effective density of the ice /firn is the only unknown parameter. InSAR is thus able to validate the firn model and find large scale error if there is any in the firn model.

Accurate earth model is important for geomechanical studies, especially for surface loading problem, in which the error of Young's modulus can proportionally propagate into the model [*Zhao et al.*, 2014]. The global 1-D model (PREM) derived from seismic velocities has been available since 1980s [*Dziewonski and Anderson*, 1981]. However, for present-day surface loading problem, the upper crust is more sensitive to the load change, but global 1-D model does not provide a good resolution in the crust. For small loads, there may be some lateral heterogeneity at different locations of the world. Moreover, Elastic moduli calculated from seismic velocities are dynamic moduli, while only static moduli derived from stress-strain relation are useful for the problem like hydraulic fracturing. However, static moduli are usually not easy to be obtained in real world environment. When the load changes are known, geodetic techniques are able to measure the long-term deformation and gravity changes due to these changes. Thus static moduli can be constrained by these measurements. Typical geodetic measurements for these studies include GPS [*Bevis et al.*, 2004], GRACE [*Steckler et al.*, 2010; *Fu et al.*, 2011] and InSAR [*Cavalie et al.*, 2005; *Nof et al.*, 2012 and *Aruiac et al.*, 2013]. In this dissertation, I will use InSAR to detect surface deformation due to ice loss on Petermann glacier, Greenland and water level drop at Yangzhoyong lake, China, and then test the elastic parameters at these two sites.

InSAR has been proved to be useful for monitoring surface deformation associated with geological CCS [*Vasco et al.*, 2008]. A series of reservoir simulations based on the first success of InSAR in In Salah, Algeria were built

[*Vasco et al., 2010*; *Rutqvist et al.*, 2010; *Rucci et al.*, 2010; *Tamburini et al.*, 2010*; Bissell et al.*, 2011; *Shi et al.*, 2012; *Rinaldi and Rutqvist*, 2013]. The CCS induced surface deformation is usually at a magnitude of several millimeters, requiring high stability of the interferometric phase. In this dissertation I will discuss the usefulness of low frequency data in rural or vegetated areas because of its ability of keeping coherence. I will also discuss the application of new generation TerraSAR-X data used for CCS monitoring.

1.3. Road map

The dissertation includes 7 chapters. The first chapter will be introduction; chapter 2 will describe a method for constraining ice mass loss and its application at Vatnajokull, Iceland; chapter 3 will be another method for ice mass loss estimation and its application at Barnes ice cap, Canada; chapter 4 will be about constraining firn density at Petermann, Greenland; chapter 5 will be about constraining the crustal elasticity at Yangzhuoyong lake, China; chapter 6 will be about detecting ground deformation due to CCS injection using InSAR in north America; and the last chapter will be conclusions.

Chapter 2

A method for estimating ice mass loss from relative InSAR observations: Application to the Vatnajökull ice cap, Iceland

Summary

We present a new method for estimating ice mass loss from glaciers and ice sheets using Interferometric Synthetic Aperture Radar (InSAR) time-series data. We use a linear inversion method based on observations of nearby bedrock uplift and a solution for surface loading of an elastic half-space. The method assumes that mass loss is focused on lower elevation terminal regions of the glacier or ice sheet, and that there is an exponential decrease in thinning rate towards the higher elevation interior. We apply the method to uplift rates between 1995-2009 near Vatnajökull, Iceland. The data reveal up to 13 mm/yr relative line-of-sight (LOS) velocity around the south-western edge of Vatnajökull. We find an ice mass loss rate of Gt/yr, in approximate agreement with other estimates.

2.1. Overview

The mass balance of ice sheets, ice caps, and glaciers is one expression of global climate change. Many recent studies suggest rapid acceleration of cryosphere melting since the late 1990s [*Khan et al.*, 2007, 2010; *Howat et al.*, 2008; *Wouters et al.*, 2008; *Chen et al.*, 2009; *Jiang et al.*, 2010; *Sorensen et al.*, 2011; *Ewert et al.*, 2011; *Shepherd et al.*, 2012; *Lenaerts et al.*, 2013; *Yang et al.*, 2013]. Ice loss currently contributes 0.7–1.8 mm/yr to present-day global sea level rise [Meier et al., 2007; Gardner et al., 2013] and this is likely to increase in the future.

Space geodetic techniques commonly used to estimate ice mass balance include the Gravity Recovery and Climate Experiment (GRACE) [*Velicogna and Wahr*, 2006; *Chen et al.*, 2006; *Ramillien et al.*, 2006; *Wouters et al.*, 2008; *Slobbe et al.*, 2009] and laser and radar altimetry [*Howat et al.*, 2008; *Pritchard et al.*, 2009; *Sorensen et al.*, 2011]. These techniques typically have limited spatial resolution. InSAR and speckle tracking can be used to measure ice flow velocities and their temporal changes [*Joughin*, 2002; *Rignot et al.*, 2011b, 2013] from which, combined with ice thickness data and regional models, changes in mass balance can be inferred [*Rignot et al.*, 2008; *Osmanoglu et al.*, 2013]. The main challenge of InSAR-based ice flow measurements is poor temporal resolution (sampling intervals of several weeks), although this recently was improved with the launch of TerraSAR-X [*Joughin et al.*, 2011]. InSAR and GPS have also been used to directly measure uplift at the edge of glaciers [*Jiang et*

al., 2010; *Bevis et al.*, 2012; *Liu et al.*, 2012; *Auriac et al.*, 2013; *Yang et al.*, 2013], from which mass balance can be inferred, as described below.

The mass loss of a glacier results in uplift of nearby crust, due to isostasy and local deformation, a process known as glacial isostatic adjustment (GIA). Hence, uplift measurements can constrain mass balance [e.g., *Jiang et al.*, 2010]. However, these methods have two limitations. First, they require independent information (or assumptions) on load distribution in areas where no geodetic observations are available, for example assuming a homogenous unloading slab [*Jiang et al.*, 2010]. Second, the observed ground deformation consists of both an instantaneous elastic and a delayed viscous component (Figure 1) [e.g., *Peltier*, 1974; *Wu*, 1992; *Mitrovica et al.*, 2001]. The elastic deformation can be assumed to represent contemporaneous uplift in response to current melting. The viscous deformation may have two components, a long delayed component due to melting of ice sheets from Earth's last glacial maximum, approximately 20,000 years ago, and a more recent component in response to the early phases of the current melting period. For example, in Iceland, the current melting period started at the end of the Little Ice Age at ~1890 AD [*Sigmundsson*, 1991]. This is long enough before present that viscous response of the lower crust and upper mantle might contribute to the contemporary surface deformation field. The viscous component has a long-wavelength signal (spatial extent larger than 40 km) because it occurs in response to flow in the mantle (mainly below 40 km). The interpretation of ground

deformation in terms of mass balance requires separation of these various spatial and temporal components [*Jiang et al.*, 2010; *Bevis et al.*, 2012].

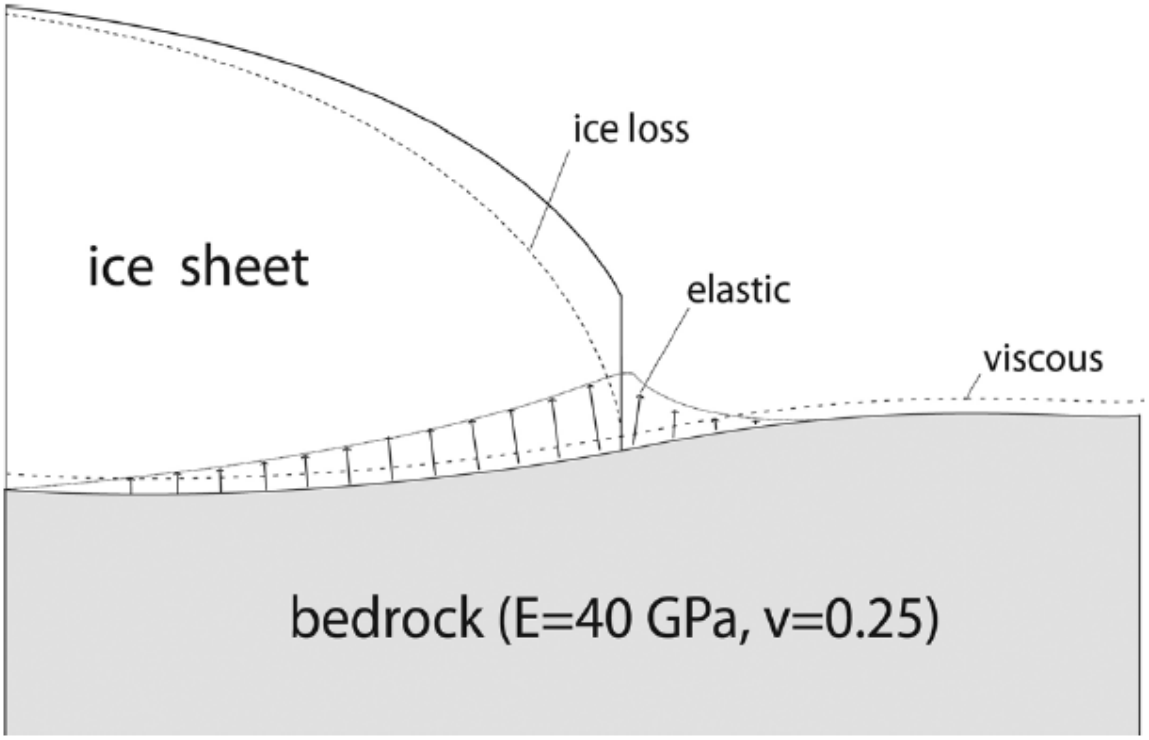

Figure 2.1. *Schematic illustration summarizing the ice mass loss estimation approach. Glacial isostatic adjustment (GIA) has two components, contemporaneous elastic response due to current melting and longer-term viscous response due to prior melting and early phases of current melting. Melting at the edge of an ice sheet results in short wavelength elastic response, whereas viscous response is a longer-wavelength signal. Relative InSAR measurements are sensitive to short but not to long wavelength signal. The method works only for ice loss along the ice edge where elastic response has much shorter wavelength than viscous response. We use an elastic half-space model with a Young's modulus of 40 GPa and Poisson's ratio of 0.25. Shrinking of the ice cap surface area is exaggerated.*

This paper presents a new approach for mass balance estimation from geodetic observations (Figure 1). We use InSAR, which measures relative displacements across a SAR scene and is sensitive to local deformation differences. Since ice melting occurs primarily at lower elevations near the ice edge, the short wavelength contemporaneous deformation (spatial extent a few tens of kilometers or less), is resolvable with InSAR and is dominated by the contemporary elastic component of deformation.

The chapter is organized as follows. We first describe the geological background (section 2.) and then introduce the theory of our ice mass loss estimation method (section 3.). We then present the InSAR observations and ice mass loss estimation for the Vatnajökull ice cap in Iceland (sections 4. and 5.), followed by a discussion of the sensitivity and potential error sources for the technique (section 6.).

2.2. Background

The Icelandic ice caps were the 7th largest contributor to global sea level rise between 2003 and 2010 [*Jacob et al.*, 2012]. Vatnajökull is the largest ice cap in Iceland, with a mean elevation of 1215 m and a maximum ice thickness of 950 m [*Björnsson and Palsson*, 2008]. The other three big Icelandic ice caps, Hofsjökull, Myrdalsjökull, and Langjökull, are located further west (Figure 2). The western part of Vatnajökull is underlain by the mid-Atlantic-ridge, which spreads at a half rate of about 1 cm/yr [*LaFemina et al.*, 2005; *Jonsson*, 2008], and by the Icelandic hot spot, coincident with the ridge. GIA following the last deglaciation

ended at ~9000 BP [*Sigmundsson*, 1991], reflecting the thermal influence of the spreading ridge and hot spot, and the corresponding low viscosity of the Icelandic upper mantle. Vatnajökull started its most recent retreat at the end of the little ice age, ~1890 [*Sigmundsson*, 1991], when its surface area was ~8600 km2 [*Björnsson and Palsson*, 2008]. From 1890 to 2003, Vatnajökull lost 435 km3 ice. Its surface area in 2007 was ~8100 km2 [*Pagli et al.*, 2007a, *Arnadottir et al.*, 2009]. The corresponding average thinning rate since 1890 is 0.5 m/yr (Table 1). Vatnajökull's ice loss and accumulation has varied in time, e.g., there was net growth from 1991 to 1994 [*Björnsson and Palsson*, 2008]. The ice loss from 1994 to 2005 was 84 km3, corresponding to an average thinning rate of 0.84 m/yr [*Björnsson and Palsson*, 2008], almost half of the maximum rate following the last glacial maximum [2 m/yr; *Pagli and Sigmundsson*, 2008].

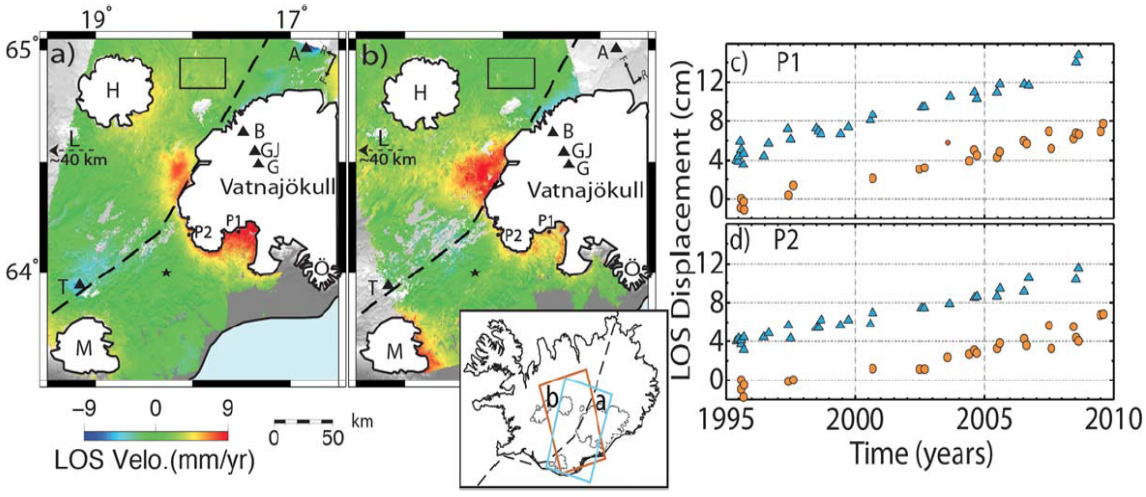

Figure 2.2. *Averaged 1995–2009 LOS velocities around Vatnajökull from (a) descending track 281 and (b) ascending track 316 and location map. Dashed line marks mid-Atlantic ridge. Star marks the reference point (near GPS station 7485). Black rectangle (east of H): area used for error estimation. A, B, G, GJ, ö,*

T: Askja, Bardarbunga Grimsvötn, Gjalp, Oraefajökull, Torfajökull volcanoes. H, L, M: Hofsjökull, Langjökull and Myrdalsjökull ice caps. (c and d) LOS displacement time series for locations P1 and P2. Blue triangles: descending orbit (shifted upward 4 mm/yr for visualization). Red circles: ascending orbit. Arrows at lower right corners of Figures 2a and 2b indicate flight directions (F) and the range (R5LOS) directions. Background of Figures 2a and 2b shows DEM of the study area.

Table 1. Ice Mass Loss Rates of the Vatnajökull Ice Cap and Whole Iceland

Period	Ice Loss Rate(Gt/yr)	Volume Loss (km^3)	Average Thinning Rate (m/yr)	Reference
Vatnajoekull				
1890–2003	3.5	435[a]	0.46	*Pagli et al.* [2007a] and *Árnadóttir et al.* [2009]
1994–2005	6.4	84[a]	0.84[b]	*Björnsson and Pálsson* [2008]
1995–2009	$6.8^{+0.8}_{-0.7}$	~110	~0.9[c]	This study
Whole Iceland				
2003–2010	11 ± 2[a]	84	N/A	*Jacob et al.* [2012]
1995–2010	9.5 ± 1.5	166	N/A	*Björnsson et al.* [2013]
1995–2009	10.3 ± 1	150	N/A	This study

[a]*Parameter given in reference.*

[b]*Calculated from total thinning of 9.2 m water equivalent thickness.*

[c]*Calculated from the mass loss rate. Other parameters are calculated using an ice density of 917 kg/m3 and a surface area of Vatnajökull of 8100 km2 (post-1990).*

In this section, we have reported average ice thinning rates. In the following sections, we consider spatially varying thinning rates following an exponential model, except for special cases of uniform thinning, when we quote the results of *Grapenthin et al.* [2006], and in Table 1, where we have converted

the estimated mass loss rate into an average thinning rate. Throughout this paper ice thinning stands for ice elevation change.

2.3. Ice mass loss rate estimation from InSAR observations

Crustal uplift due to ice melting is a surface unloading problem, similar to loading the crust by water level changes in artificial or natural lakes [*Kaufmann and Amelung*, 2000; *Cavalie et al.*, 2007; *Nof et al.*, 2012]. We use the solution for the surface displacement of an elastic half space due to a point source with a unit mass in cylindrical coordinates assuming axial symmetry [*Sneddon*, 1951; *Pinel et al.*, 2007]:

$$V(r)=\frac{g}{\pi}\frac{1-\upsilon^2}{E}\frac{1}{r} \quad (1)$$

$$U(r)=\frac{g}{2\pi}\frac{(1+\upsilon)(1-2\upsilon)}{E}\frac{1}{r} \quad (2)$$

where V and U are the vertical and radial displacements, g is the gravitational acceleration, t is the Poisson's ratio, E is the Young's modulus, and r is the distance from the point source. We assume that the load change (mass loss rate) is constant with time and use velocities instead of displacements. In the following,

we formulate a linear inverse problem to estimate the load change from surface

velocities.

Glaciers and ice sheets generally melt from the edge toward the interior [*Sigmundsson and Einarsson*, 1992; *Marshall et al.*, 2005]. We assume that the

mass loss rate decreases exponentially with distance from the ice edge and describe it using the thinning rate h(x),

$$h(x)=c+(a-c)e^{-x/k} \tag{3}$$

where k is the decay distance (the distance where the thinning rate reduces to 1/e of the rate at the edge), x is the distance from the ice edge, c is the thinning rate at the inland portion of a glacier (x >> k), and a is the thinning rate at the ice edge (x50). The units of h, a, and c are m/yr (positive for thinning), and k is in meters. Ice accumulation far from the ice edge is represented by negative c. We can expand this one-dimensional model to a two-dimensional model by dividing the load change into a series of square blocks, calculating the displacement rate due to point loads with the corresponding masses for each block, and superposing the solutions for all blocks. The ground velocities $d_l^{v,e,n}$ for such a model are calculated as

$$d_l^v=\sum_{i=1}^{N}(c+(a-c)\exp(-x_i/k))\frac{\delta^2\rho g(1-\upsilon^2)}{\pi E r_{li}} \tag{4}$$

$$d_l^{e,n}=\sum_{i=1}^{N}(c+(a-c)\exp(-x_i/k))\frac{\delta^2\rho g(1+\upsilon)(1-2\upsilon)}{2\pi E r_{li}} \tag{5}$$

where superscripts *v*, *e*, *n* represent vertical, east, and north directions, x_i is the distance of an ice block to the ice edge, i = 1,. . ., N with N the number of blocks, δ is the block spacing, ρ is the density of ice, and r_{li} the distance between the

point load representing block i and observation point l = 1,. . ., L with L the number of observations.

The ground velocity is linear with respect to parameters a and c and nonlinear with respect to k. InSAR measures velocities in the radar line-of-sight direction (LOS). For a given k, we have a linear system,

$$\mathbf{d}=\mathbf{AM} \qquad (6)$$

where $\mathbf{d}=[d_1,\cdots,d_L]^T$ is the L × 1 vector of observations (LOS velocities) and $m=[a,c]^T$ the 2 × 1 vector of model parameters. We use the least-square solution

$$\mathbf{m}=\mathbf{A}^{-g}\mathbf{d} \qquad (7)$$

with $\mathbf{A}^{-g}$ the generalized inverse. The model variance is given by [*Snieder and Trampert*, 1999]

$$\sigma_{m_i}^2=\sum_l\left(A_{li}^{-g}\sigma_{d_l}\right)^2 \qquad (8)$$

where σ_{m_i} is the model standard error of the ith ice block, σ_{d_l} is the standard error of lth velocity field. The design matrix **A** can be written as

$$\mathbf{A}=\mathbf{B}\cdot\mathbf{C}\times\mathbf{D} \qquad (9)$$

where **A** is a L × 2 matrix, and each line represents the mapping relationship between independent variables and observation at location l. The *l*th line of **A** represents the mapping from mass loss rate to the lth absolute velocity field. By subtracting the line representing the reference point from each line, **A** is then a relative mapping matrix. The dot operator represents matrix elementary multiplication, and the cross operator represents matrix multiplication.

$$\mathbf{B}=\begin{bmatrix} \cos\theta_1 & \dots & \cos\theta_1 & -\sin\theta_1\cos\alpha_1 & \dots & -\sin\theta_1\cos\alpha_1 & \sin\theta_1\sin\alpha_1 & \dots & \sin\theta_1\sin\alpha_1 \\ \vdots & \vdots & \vdots & \vdots & \vdots & \vdots & \vdots & \vdots & \vdots \\ \cos\theta_L & \dots & \cos\theta_L & -\sin\theta_L\cos\alpha_L & \dots & -\sin\theta_L\cos\alpha_L & \sin\theta_L\cos\alpha_L & \dots & \sin\theta_L\cos\alpha_L \end{bmatrix} \tag{10}$$

$$C=\frac{\rho g}{\pi E}\begin{bmatrix} \frac{1-\upsilon^2}{r_{11}} & \dots & \frac{1-\upsilon^2}{r_{1N}} & \frac{(1+\upsilon)(1-2\upsilon)}{2r_{11}} & \dots & \frac{(1+\upsilon)(1-2\upsilon)}{2r_{1N}} & \frac{(1+\upsilon)(1-2\upsilon)}{2r_{11}} & \dots & \frac{(1+\upsilon)(1-2\upsilon)}{2r_{1N}} \\ \vdots & \vdots & \vdots & \vdots & \vdots & \vdots & \vdots & \vdots & \vdots \\ \frac{1-\upsilon^2}{r_{L1}} & \dots & \frac{1-\upsilon^2}{r_{LN}} & \frac{(1+\upsilon)(1-2\upsilon)}{2r_{L1}} & \dots & \frac{(1+\upsilon)(1-2\upsilon)}{2r_{LN}} & \frac{(1+\upsilon)(1-2\upsilon)}{2r_{L1}} & \dots & \frac{(1+\upsilon)(1-2\upsilon)}{2r_{LN}} \end{bmatrix} \tag{11}$$

$$\mathbf{D}=\begin{bmatrix} \exp\left(-\frac{x_1}{k}\right) & 1-\exp\left(-\frac{x_1}{k}\right) \\ \vdots & \vdots \\ \exp\left(-\frac{x_N}{k}\right) & 1-\exp\left(-\frac{x_N}{k}\right) \\ \exp\left(-\frac{x_1}{k}\right) & 1-\exp\left(-\frac{x_1}{k}\right) \\ \vdots & \vdots \\ \exp\left(-\frac{x_N}{k}\right) & 1-\exp\left(-\frac{x_N}{k}\right) \\ \exp\left(-\frac{x_1}{k}\right) & 1-\exp\left(-\frac{x_1}{k}\right) \\ \vdots & \vdots \\ \exp\left(-\frac{x_N}{k}\right) & 1-\exp\left(-\frac{x_N}{k}\right) \end{bmatrix} \quad (12)$$

where **B** and **C** are 2 L × 3N matrices, in which the first N columns correspond to vertical component, the second N columns correspond to east component, and the third N columns correspond to north component. **B** contains the mapping parameters from three-dimensional velocities to LOS direction. **C** is generated from equations (4) and (5). θ is the look angle of the radar beam and a is the azimuth angle representing the flight direction. **D** is a 3N × 2 matrix for parameters describing the exponential unloading model.

We establish a series of linear inversions by searching each possible value of k with reasonable stepping (5000 m). For a given k, we thus solve for a

and *c*. Although the inversion problem is overdetermined, the sensitivity of the data for predicting the model varies spatially. In the far field (far from the ice edge), the data resolutions [*Menke*, 1989] are very poor. Low data resolution can bias the model predictions [*Lohman and Simons*, 2005; *Xia et al.*, 2008]. We thus use a weighting approach according to the diagonal values of the data resolution matrix $w = (\mathrm{diag}(\mathbf{N}))^p$, where *w* is the weighting vector, **N** is the data resolution matrix, diag() represents the process of retrieving the diagonal vector of **N**, and *p* is a amplification factor. We use $p = 2$ for this study.

The estimated mass loss rate thus should depend on *k*. In practice, we find that although *a* and *c* are sensitive to *k*, the estimated mass loss rate is not (see section 5.). We conclude that the proposed approach allows a reliable estimation for glaciers and ice sheets with exponential thinning from edge to interior.

2.4. InSAR data

We use 1995–2009 C-band ERS imagery and the Small Baseline InSAR time-series method [*Berardino et al.*, 2002; *Fattahi and Amelung*, 2013] for measuring the contemporaneous deformation around Vatnajökull. In Iceland, only summer acquisitions (late June to early October) are suitable for InSAR because of snow cover during other seasons; the typical temporal density is three images per year for each track. We combine the SAR acquisitions to form interferogram networks using thresholds in perpendicular spatial baseline of 300

m and temporal baseline of 3 years, supplemented by a few longer temporal or spatial baseline interferograms to ensure full network connection (110 and 43 interferograms on descending and ascending tracks, see Figure 2.3.). We estimate ground velocity assuming linear deformation (neglecting seasonal effects although they are known to be significant) [*Grapenthin et al.*, 2006]. We eliminate long-wavelength phase contributions (the signal across the two SAR frames) by removing quadratic surfaces in range and azimuth directions, estimated at each epoch of the InSAR time-series after masking out the deforming areas near the ice edge. The long-wavelength phase contributions are due to plate motion [*LaFemina et al.*, 2006; *Geirsson et al.*, 2012], viscous deformation, and possibly orbital uncertainties [*Gourmelen et al.*, 2010]. The effect of stratified atmospheric delays is small because of limited topographic relief in the study area. InSAR measurements, in particular at high latitudes, can be affected by ionospheric disturbances but this effect is generally small for C-band data [*Meyer*, 2011].

Figures 2a and 2b show the 1995–2009 relative LOS velocities for the descending and ascending tracks. The InSAR measurements are relative to a reference point, which is a point near GPS station 7485 of *Arnadottir et al.* [2009]. Although the relative velocities could be transferred into absolute velocities using the motion of this station, it is not needed, because our modeling approach uses relative velocities only.

Figure 2 shows a 5–10 km wide yellow-red band around the southwestern edge

of Vatnajökull, corresponding to relative LOS velocities up to 13 mm/yr and a large area of uplift west of the ice cap. The standard error of the LOS velocity fields are ~0.4 mm/yr and ~0.7 mm/yr for the descending and ascending tracks, respectively, estimated following Gourmelen et al. [2007] in an 18 × 18 km2 nondeforming area (marked by the rectangle in Figures 2a and 2b). The displacement histories shown for two points near the ice edge suggest almost constant LOS annual velocity during the observation period (Figures 2c and 2d). Deviations up to 3 cm are most likely due to atmospheric effects and seasonal loading variations. The spatial extent of uplift is clearly represented in a map of vertical velocity (Figure 3), obtained by combining the descending and ascending LOS velocities vertical and horizontal velocities. The vertical ground velocity from InSAR is consistent with the relative changes in GPS velocities of *Arnadottir et al.* [2009] (the root-mean-square deviation is 2.1 mm/yr, see Figure 2.4).

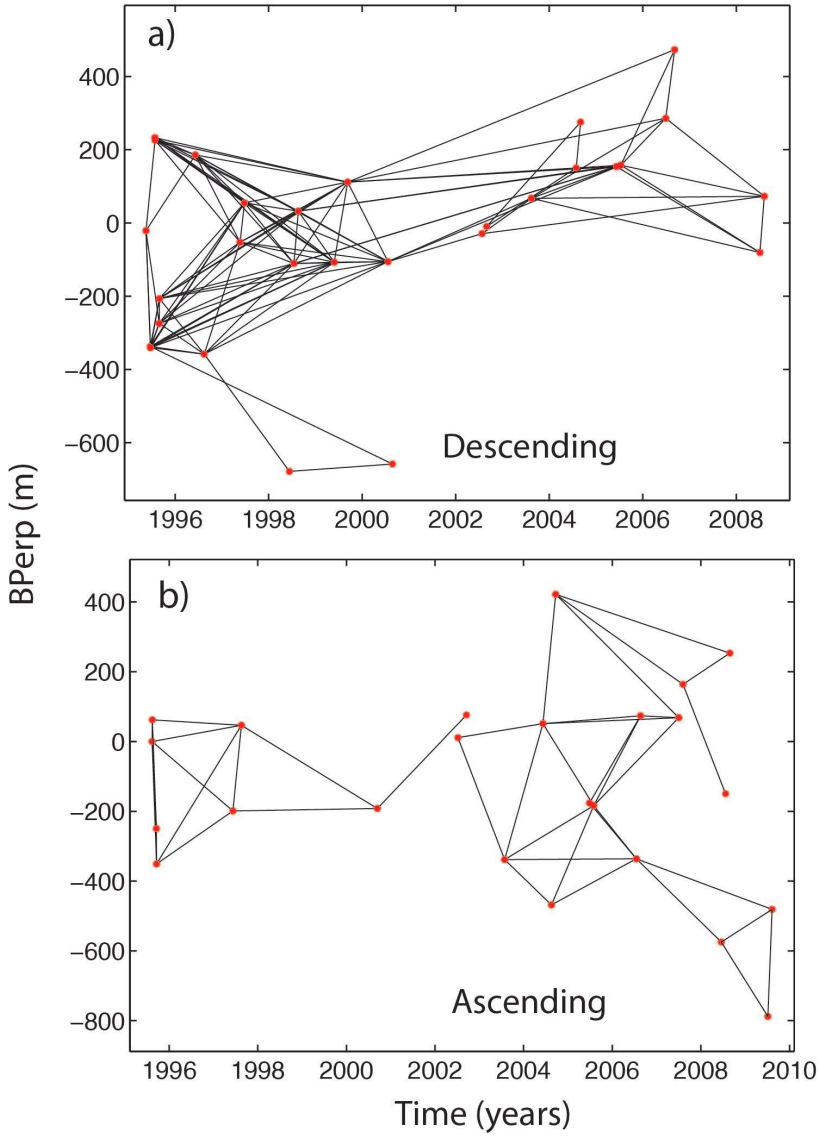

Figure 2.3. *Baseline-time plot of the network of SAR acquisitions (red dots) and interferograms (black lines) used for the time-series inversion.*

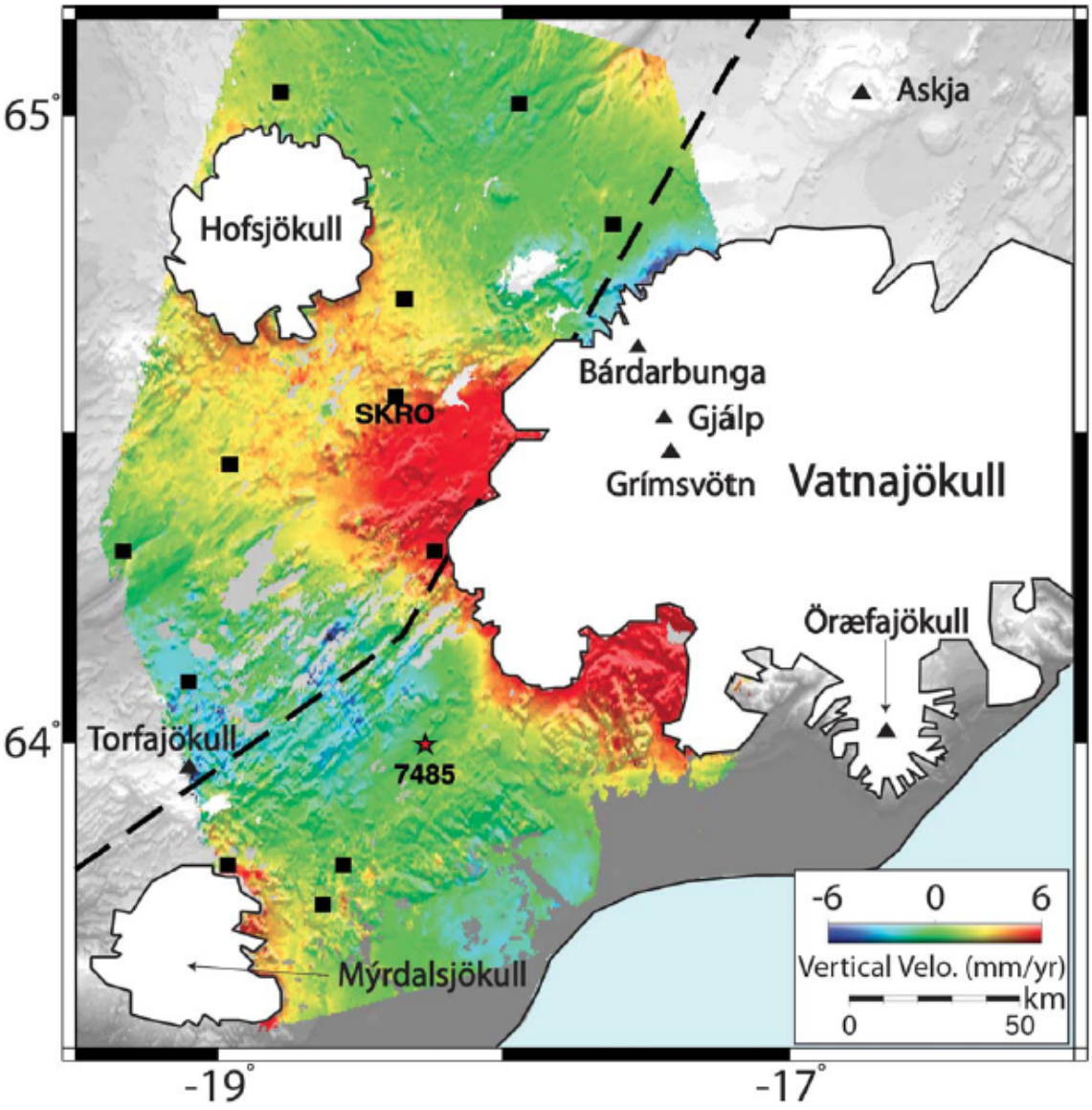

Figure 2.4. *Vertical velocity map derived from descending and ascending LOS velocity fields. Dashed line: axis of mid-Atlantic-ridge. Red star : reference point. Black squares: GPS stations. SKRO: a continuous GPS station. Black triangles are volcanoes.*

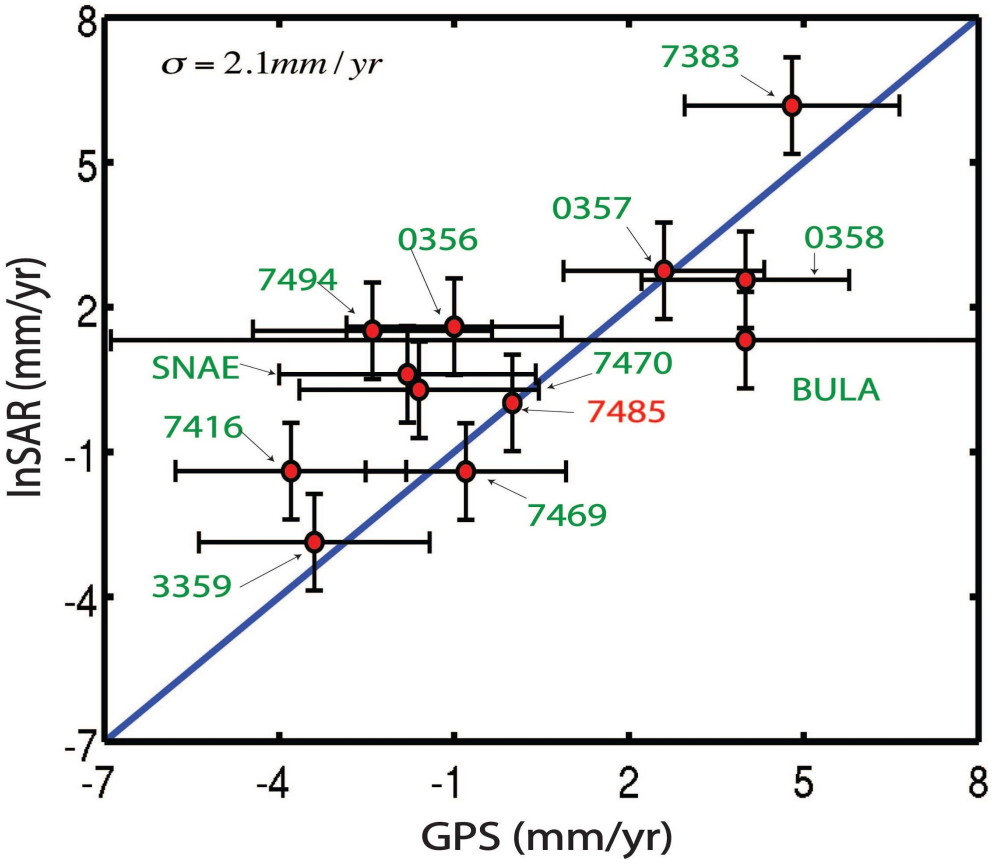

Figure 2.5. *InSAR – GPS comparison for vertical velocities. The numbers mark the names of the GPS stations. Station 7485 is used as reference for all points.*

2.5. Ice mass loss rate estimation

We estimate the ice mass loss rate using equation (7) for thinning rate models with different decay distances k. To build matrices B and C, we represent the load change (the change of ice mass) by a series of 1.4 km2 square blocks, each of which is approximated by a point load. We do not consider changes in surface area because the associated mass change is small. We select an area not influenced by recent volcanic activity southwest of Vatnajökull (the rectangle in Figure 5, surface area ~2500 km2) and sample the velocity fields using a

uniform grid to obtain a data vector consisting of 478 descending and 454 ascending LOS velocities. The fit of a model to the data is described by the Root Mean Square Error, $RMSE = \sqrt{\sum_{l=1}^{L} (d_l - p_l)^2 / L}$, with d_l is the observations, p_l is the model predictions, and L is the number of observations. We assume unit variance for all data points.

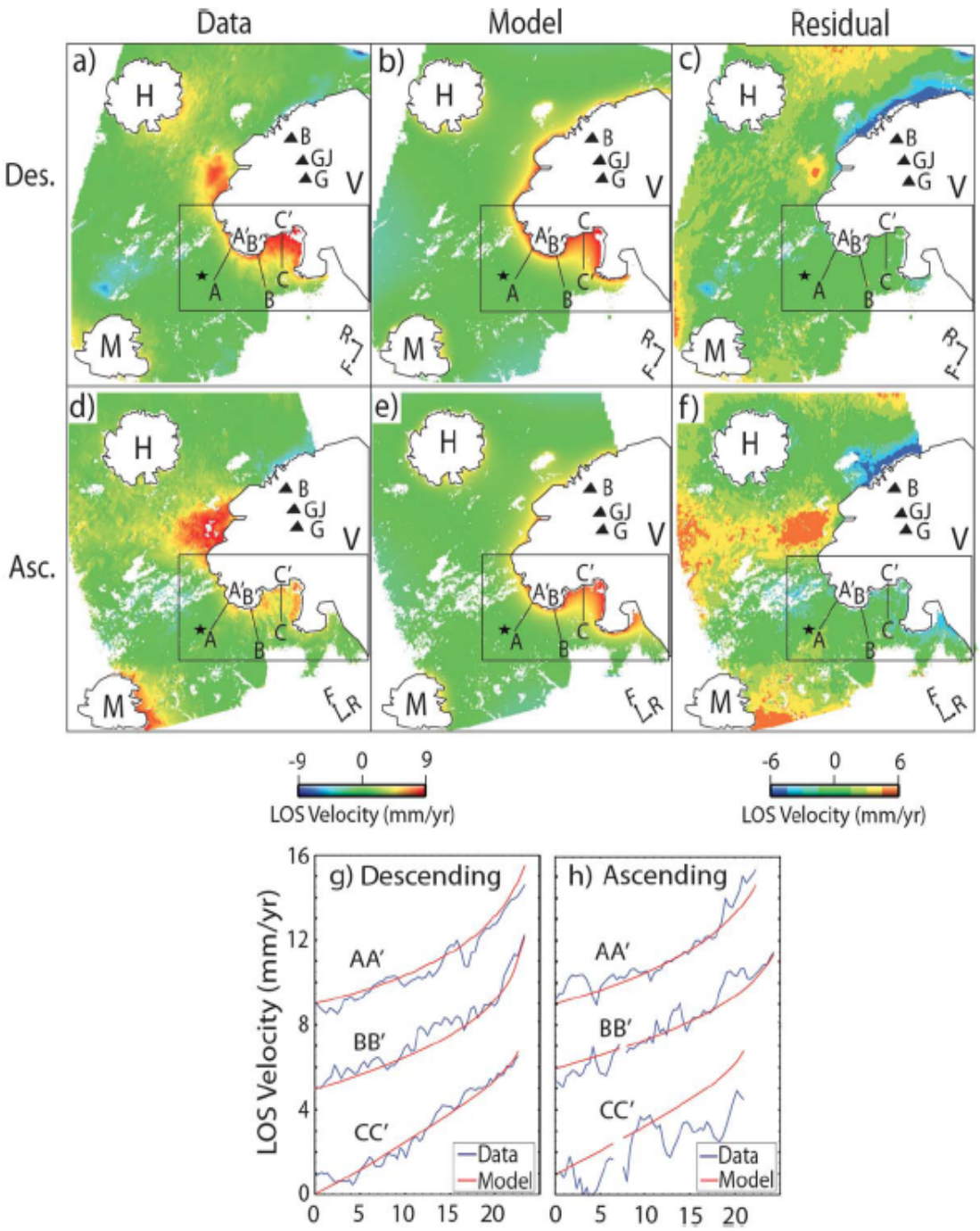

Figure 2.6. *(a and d) Observations, (b and e) models, and (c and f) residuals. The modeled velocities were calculated for decay distance 57.5 km. Star: reference point. Black triangles: areas used for modeling. (g and h) LOS velocities along profiles for descending and ascending track. The AA' and BB'*

profiles are shifted by several mm/yr. The descending track generally fits the model better than the ascending track because of more interferograms generated on this track. B: Bardarbunga volcano, G: Grimsvötn volcano, GJ: Gjalp volcano, H: Hofsjökull ice cap, M: Myrdalsjökull ice cap, and V: Vatnajökull ice cap. Red star : reference point.

We first test an unrealistic spatially uniform thinning rate model ($k \to \infty$ in equation (3)). The solution suggests an ice mass loss rate of 20.8 Gt/yr (corresponding to an average thinning rate of 2.8 m/yr), significantly higher than previous mass loss rate estimates (Table 1). This model is characterized by an RMSE of 4.3 mm/yr, suggesting a relatively poor fit to the observations, and suggesting that a spatially uniform thinning rate model is not appropriate.

We next consider exponential thinning rate models. We conduct a grid search over the decay distance *k*, and estimate for each *k* the parameters *a* and *c* using equation (6), varying *k* from 1 to 30 km with a step size of 0.5 km. The estimated mass loss rate depending on *k* is 6.8–7.3 Gt/yr (Figure 6). This narrow range of 0.5 Gt/yr suggests that variations in *k* are largely compensated by variations of *a* and *c*. We also found that RMSE does not vary significantly with *k*, i.e., the data are not sufficient to resolve *k*. *Björnsson and Palsson* [2008] present a thinning rate model that can approximated by an exponential model with *k* = 7.5 km, *a* = 5.5 m/yr, and *c* = 21.6 m/yr (Figure 7). We thus use *k* = 7.5 km and invert for *a* and *c*. We find *a* = 3.75 m/yr and *c* = 20.75 m/yr, similar to values calculated by *Björnsson and Palsson* [2008].

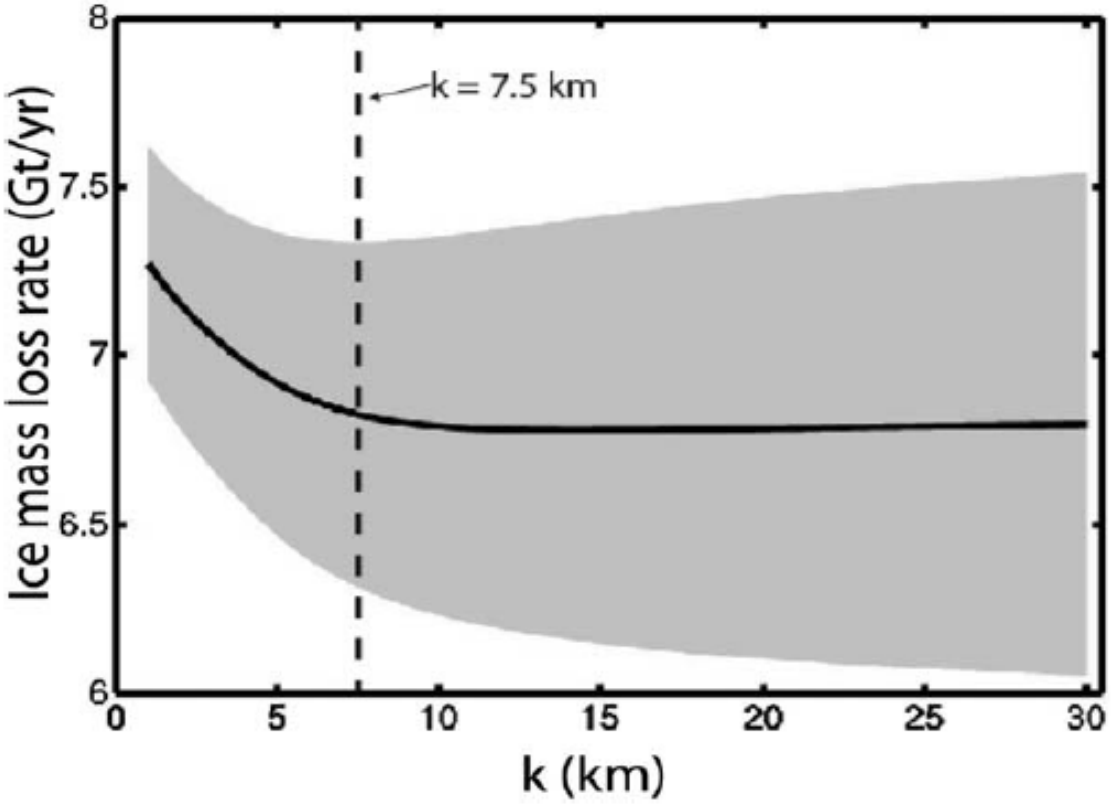

Figure 2.7. *Ice mass loss rate as a function of the decay distance k. The gray-shaded area marks the uncertainties range which is calculated based on equation (8). Dashed line marks the preferred model at k = 7.5 km.*

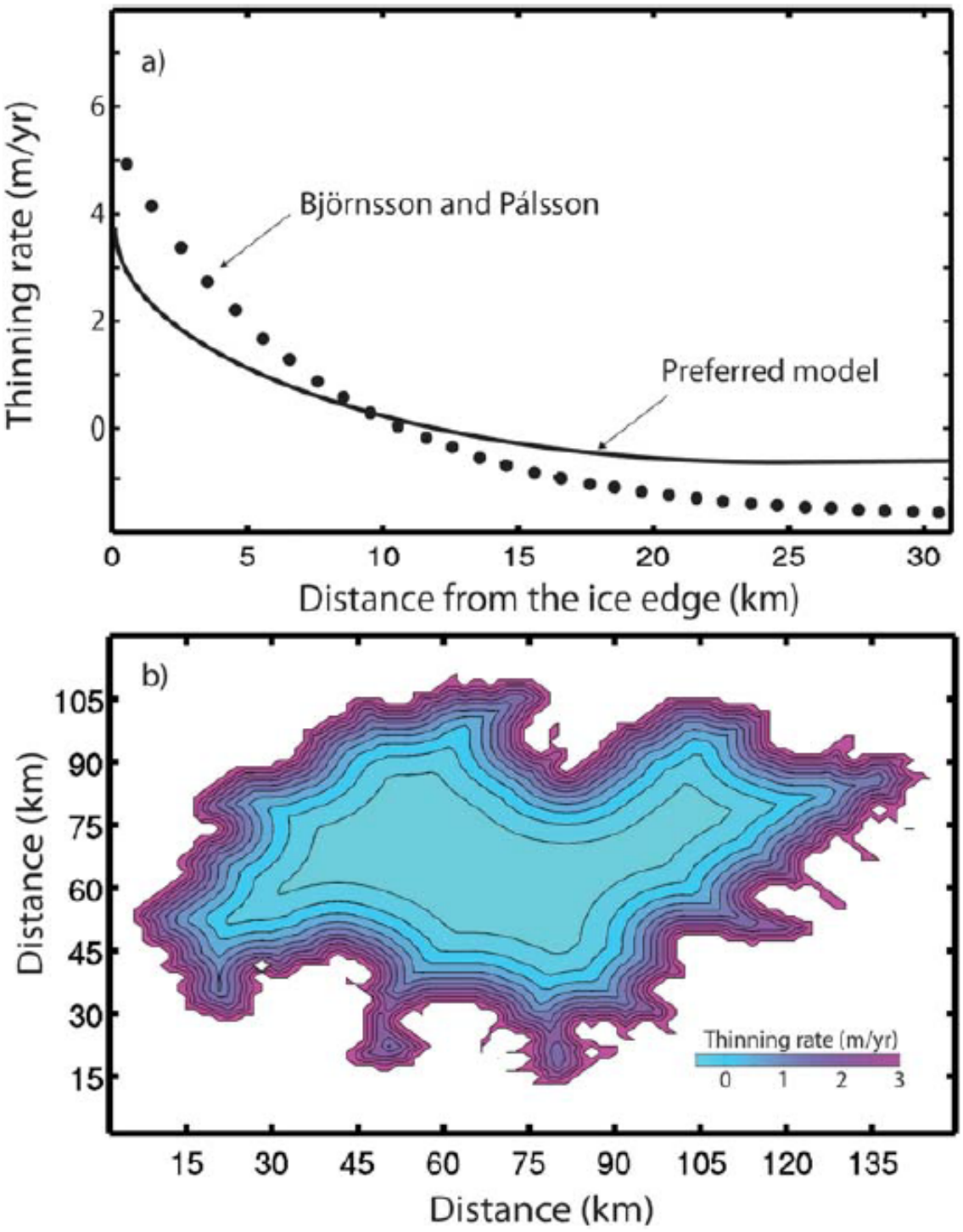

Figure 2.8. *Thinning rate model of Vatnajökull. (a) Solid line: 1-D estimated model for k57.5 km (a = 3.75 m/yr, c = 20.75 m/yr) and dotted line : exponential approximation to the model form Björnsson and Palsson [2008] (k = 7.5 km, a =*

5.5 m/yr, and c = 21.6 m/yr). (b) two-dimensional thinning rate model obtained using the estimated 1-D model.

Including the observation error, the estimated range of mass loss rate is $6.8^{+0.8}_{-0.7}$ Gt/yr. Adding the uncertainties associated with bounds in Young's modulus (40 ± 15 GPa) [*Grapenthin et al.*, 2006], the estimated mass loss rate is $6.8^{+3.3}_{-3.2}$ Gt/yr.

Figure 5 shows the comparison between the model with k = 7.5 km and the observations. In the area southwest of Vatnajökull, the model predictions closely resemble the observations (Figures 5c and 5f). Some areas with high residuals are addressed below (section 6.1).

For the Hofsjökull (surface area 925 km^2) and Myrdalsjökull (600 km^2) ice caps we also use exponential thinning rate models, invert for the mass loss rate and obtain rates of 0.9 and 1.7 Gt/yr, respectively. The estimate for Hofsjökull is close to that of *Grapenthin et al.* [2006] (their average thinning rate of 1 m/yr for 1996–2001 corresponds to a mass loss rate of 0.85 Gt/yr), but not the estimate for Myrdalsjökull. *Grapenthin et al.* [2006] report an average thinning rate of 0.5 m/yr which corresponds to a mass loss rate of 0.3 Gt/yr. The estimates of the smaller ice caps are not well constrained because of the depth variation of Young's modulus (see section 6.3.). For Langjökull (950 km2), we use the average thinning rate of 1.3 m/yr of *Grapenthin et al.* [2006], which corresponds to a mass loss rate of 0.9 Gt/yr, 1996 – 2004.

2.6. Discussion

2.6.1. Model fit

Here we investigate discrepancies between our model predictions and observations. First, there is a lack of observed uplift at the northwestern edge of Vatnajökull. This is an area of highest topographic elevation where melting is slow because of low air temperature [*Björnsson and Palsson*, 2008]. This is not represented by our simple thinning rate model. This area was also subjected to subsidence following the 1996 eruption of Gjalp subglacial volcano [*Pagli et al.*, 2007b]. Discrepancies near the Hofsjökull and Myrdalsjökull ice caps are also likely due to simplification of the assumed thinning rate model. For these small ice caps, the exponential model may not fit very well because of the large contribution of outlet glaciers. Third, there is an excess uplift (Figure 4) west of Vatnajökull, also noted by *Arnadottir et al.* [2009]. This area is located above and west of the spreading center. A possible explanation for excess uplift here is viscoelastic deformation related to a locally low effective elastic layer thickness. The data from these areas are not included in the modeling and do not affect the estimated ice mass loss rate.

2.6.2. Effect of viscoelastic behavior

Our approach to mass loss estimation is based on the assumption that the observed relative uplift can be explained by rebound of a homogeneous elastic half-space. However, GIA has both elastic and viscous components due to viscous flow in the upper mantle and possibly in the lower crust. Modeling of

GPS observations suggest that Icelandic lithosphere has a high viscosity lower crust and a low viscosity upper mantle, with average viscosities of $>10^{21}$ Pa•s and 1019 Pa•s, respectively, and a crustal thickness of 40 km [e.g., *Arnadottir et al.*, 2009]. *Auriac et al.* [2013] show that this rheological structure holds for the larger Vatnajökull area. However, spatial variations in rheology are likely. Iceland is located on a mid-ocean ridge and a hot spot. The lower crust and upper mantle can be thermally weakened depending on location [e.g., *Barnhoorn et al.*, 2011]. For the ridge area in southwestern Iceland, *Jonsson* [2008] finds lower crustal and upper mantle viscosities of 10^{19} Pa•s and 3–4 $\times 10^{18}$ Pa•s, respectively. *LaFemina et al.* [2005] find near Vatnajökull a stronger lower lithosphere (10^{19} to 10^{20} Pa•s), which may reflect an increased crustal thickness. For most of Iceland, the seismic crustal thickness is 30–40 km; it is thickest under Vatnajökull and thins to 20 km in the southwest [*Foulger and Natland*, 2003].

To assess the potential impact of these effects, we compute the effect of viscoelastic relaxation on the deglaciation-induced uplift using the 3D version of the finite element code GTecton [*Govers and Wortel*, 2005]. We try the effects of two different models—one with a 40 km elastic plate and half-space viscosity of 10^{18} Pa•s (model A) and a second one with a thinner elastic layer over a viscoelastic half space with a higher viscosity (5 km elastic plate and half-space viscosity of 10^{19} Pa•s, model B). Model A is similar to the model of *Auriac et al.* [2013] but has a lower viscosity, simulating the effect of elevated temperature due to the mid-ocean ridge. Model B has a low lower crustal (5–40 km) viscosity, which could be the result of high water content or nonlinear rheology. We use a

time-variable, constant disk load to simulate a realistic deglaciation history (see caption of Figure 8 for details of the load).

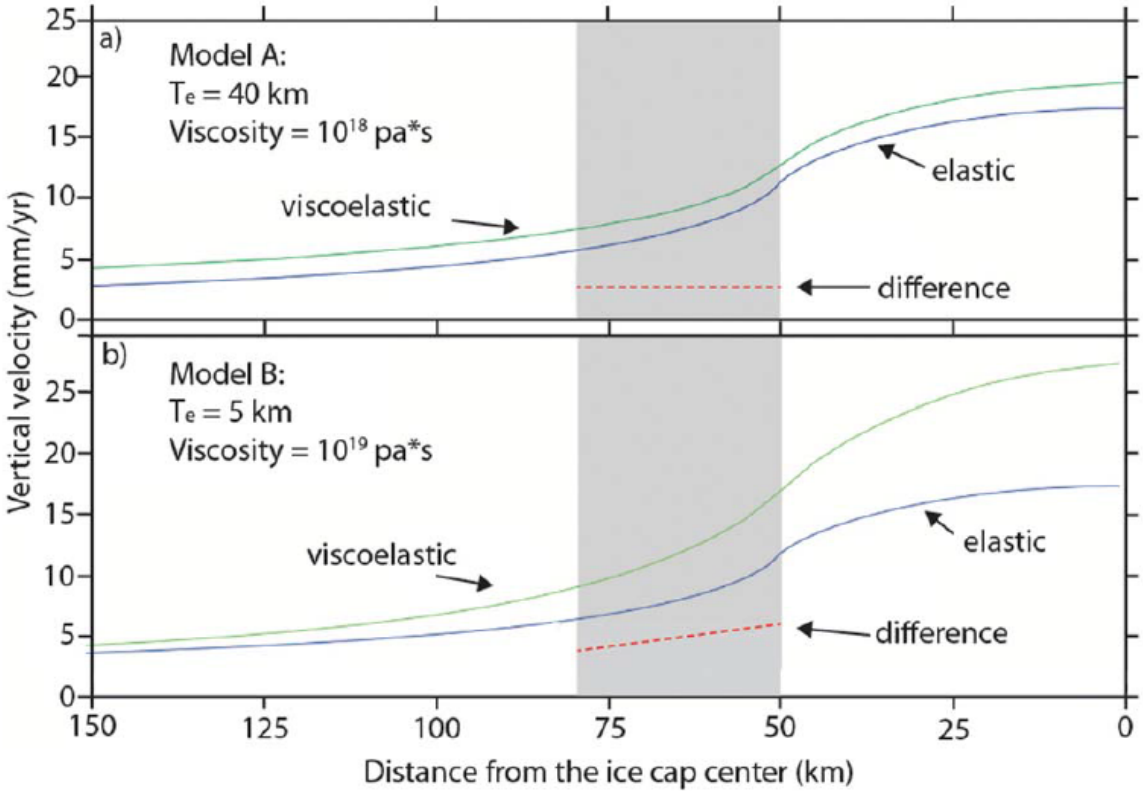

Figure 2.9. *Simulated 1995–2009 vertical velocities for disk (50 km radius) unloading of the lithosphere along a radial profile from the disk center to 150 km distance for two different Earth models. (a) Model A: 40 km elastic layer and 1018 Pa•s half-space viscosity. (b) Model B: 5 km elastic layer and 1019 Pa•s half-space viscosity; Deglaciation starts in 1890 with thinning rates of 25, 40, and 84 cm/yr for 1890–1964, 1965–1994, and 1995–2009, respectively. Blue line: elastic response. Green line: viscoelastic response. Red dashed line: difference between blue and green lines. Gray region: area of InSAR observations at 50–80 km distance from the disk center.*

For model A, the elastic and viscoelastic responses are similar. The viscous component produces a constant offset of 2 mm/yr (red dashed line in Figure 8a) without affecting the uplift gradient. For model B, the viscous component decreases from 10 mm/yr at the load center to 1 mm/yr at 150 km distance (Figure 8b). It contributes ~2.5 mm/yr to the uplift gradient at 50–80 km distance. Our approach of eliminating long wavelength deformation further lessens the impact of possible viscous deformation because it is largely removed from the observations. Weighting based on data resolution further reduces the magnitude of these viscous effects because areas with higher viscous than elastic deformation (far from the ice edge) receive less weight.

We conclude that for modeling relative uplift near the ice edge the viscous component can safely be neglected, except in the case of a very weak lithosphere and a thin elastic layer. In this case, the elastic half-space assumption (i.e., neglecting viscous deformation) would lead to an overestimation of the mass loss rate, with the actual rates being smaller than the estimates. In other words, except for this very special situation, relative InSAR observations at the ice edge are mainly sensitive to the elastic component but not to the viscous component of surface deformation associated with melting ice. Of course, InSAR can only resolve mass loss at the edge of glaciers and ice sheets.

The low viscosities of Model B are unlikely to occur under Iceland for two reasons. First, the upper mantle is relatively dry [*Barnhoorn et al.*, 2011] and there is no water that could act to reduce the viscosity. Second, for typical grain

sizes of mid-ocean ridge mantle rock and for relatively low deglaciation-induced strain rates, linear diffusion creep is likely the dominant deformation mechanism [*Barnhoorn et al.*, 2011].

2.6.3. Young's modulus

Our model assumes a Young's modulus of 40 GPa. It is important to justify this assumption because surface displacement is proportional to the load and inversely proportional to Young's modulus (equations (1) and (2)). An inversion with twice the value of the Young's modulus would yield twice the mass loss rate.

This modulus was estimated from GPS observations of the vertical deformation associated with seasonal loading in Iceland (winter snowfall and summer melting) [*Grapenthin et al.*, 2006]. It can be considered an effective Young's modulus for the elastic crust sampled by the load. For smaller loads, the effective Young's modulus could be smaller because the shallow crust is likely to be more fractured, hence weaker. For example, *Pinel et al.* [2007] found an effective Young's modulus of 29 GPa for the smaller Myrdalsjökull ice cap, suggesting that also the load change due to melting is of smaller spatial extent than for Vatnajökull. For larger seasonal loads significantly larger effective Young's moduli are found [*Bevis et al.*, 2005; *Steckler et al.*, 2010].

For the Icelandic crust, the mean P-wave velocities of 6.0 and 6.6 km/s at depths of 5 and 10 km [from Yang and Yang, 2005] correspond to dynamic modulii of 87 and 105 GPa, respectively (using a density of 2900 kg/m3 and

Poisson's ratio of 0.25). Our choice of Young's modulus is significantly lower than these values and is more likely representative of conditions associated with relatively slow load changes induced by glacial melting compared to higher values estimated from the passage of seismic waves.

Our values is consistent with the effective Young's modulus of 44 GPa of *Nof et al.* [2012] from modeling uplift induced by rapid decline of the Dead Sea water level. The Dead Sea load change (~15 km across) is similar in size to the Vatnajökull load change (k = 7.5 km).

2.6.4. Mass loss rate

For the 1995–2009 period, the mass loss rate of the Vatnajökull ice cap estimated from the InSAR data is (depending on k) $6.8^{-0.8}_{-0.7}$ Gt/yr. Mass loss rates from this and previous studies are summarized in Table 1. Our estimate agrees with the 1994–2005 rate of 6.4 Gt/yr from *Björnsson and Palsson* [2008]. A limitation of our study is that we only use observations from the southeast edge of the ice cap. That our mass loss rate estimate agrees with the in situ observations suggests that this section is melting at the average rate of the ice cap. The estimated mass loss is about twice the average mass loss rate of 3.5 Gt/yr from 1890 to 2003 [*Pagli et al.*, 2007a]. The rather constant uplift velocity during 1995–2009 (Figures 2c and 2d) suggests ice loss at a constant rate, in contrast to Greenland where ice loss is accelerating [*Jiang et al.*, 2010; *Rignot et al.*, 2011a].

We estimate mass loss rates for the Hofsjökull and Myrdalsjökull ice caps of 0.9 and 1.7 Gt/yr. Together with Langjökull's mass loss rate of 0.9 Gt/yr, the total loss rate for the four major Icelandic ice caps (Vatnajökull, Hofsjökull, Myrdalsjökull, and Langjökull) is 10.3 ± 1 Gt/yr. This is equivalent to the 11 ± 2 Gt/yr estimated from 2003 to 2010 GRACE data [*Jacob et al.*, 2012].

2.7. Conclusions

We have presented an approach to estimate ice loss from uplift measurements of the Earth's crust near glaciers and ice sheets that is optimized for the high spatial resolution of InSAR. The linear relationship between surface load change and ground uplift for elastic rheology allows us to estimate the ice mass loss rate from the measured uplift as long as prior information on Young's modulus and the spatial thinning pattern of ice is available. An exponential decrease in thinning rate with distance from the ice edge is applicable for many glaciers and ice sheets. Our InSAR-based approach resolves small wavelength, relative changes in uplift across a SAR frame, and is especially sensitive to contemporaneous load changes along the ice edge. It is presumably also applicable to systems dominated by ice loss near the terminus, e.g., systems undergoing the initial stages of rapid retreat (later stages may be dominated by dynamic effects and mass loss farther from the terminus). Spatial variations in ice loss due to variations in air temperature or precipitation and variable outlet glacier geometry can in principle be resolved by separately analyzing different sections of ice.

For Vatnajökull, we find for the 1995–2009 period an average ice mass loss rate of $6.8^{+0.8}_{-0.7}$ Gt/yr consistent with ground-based estimates and broadly consistent with GRACE estimates for the entire island. We used only observations from the southwestern ice edge, suggesting that mass loss in this area is representative of the entire ice cap.

Chapter 3

Another method for estimating ice mass loss from InSAR observations: Application to the Barnes ice cap, Canada

Summary

We present a method for ice mass loss estimation for ice caps using synthetic aperture radar interferometry (InSAR) time-series data. The method is based on the linear elastic theory describing relation between load and associated deformation. To overcome the underdeterminacy of the linear system, we use three extra constraints which resample the model space reducing the model complexity, control the smoothness of the model using a penalty function, and control the absolute range of each model parameters using constrained least-square. We apply this method to the surface bed-rock displacement near the Barnes ice cap, which reveals up to 5 cm relative line-of-sight (LOS) displacement between May 2012 and April 2015. We find an ice mass loss of 32.9±4.3 Gt during the study period, comparing to another

estimate based on the method considering the exponential relation between ice thinning and distance from the ice edge introduced in *Zhao et al.* [2014], which obtains an ice mass loss of 27.9±3.2 Gt.

3.1. Overview

InSAR time-series has been able to detect millimeter level small ground motion since late 2000s [*Gourmelen et al.*, 2010; *Vasco et al.*, 2010; *Ferretti et al.*, 2011; *Zhao et al.*, 2014] using multi-temporal interferograms. This technical advancement brings great opportunities to extend InSAR to the studies of ice mass loss estimation in the cryosphere. However, there was not geomechanical model, a simple model based on elastic theory tends to be significant under-determined without stable solution. *Lin et al.* [2012] suggested to use a penalty function constraining the spatial smoothness of ice loss pattern, and the method was applied to Jackobshavn Isbrea, Greenland between 2004 and 2008, validated by aerial triangulation measurement (ATM, laser altimetry). *Zhao et al.* [2014] provided a solution considering the approximated exponential relation between ice thinning rate and distance from the ice edge, and this method was applied to Vatnajokull, Iceland. In this study, we further discuss several potential methods can be used for the InSAR based ice mass loss study on a mathematical perspective. First, we add a constraint on the spatial smoothness based on Tokhonov regularization [*Lin et al.*, 2012]. Second, we add quad-tree resampling into the model to reduce the model complexity and increase data sensitivity at the same time. Third, we use a real range of ice thinning rate, e.g. in

Iceland it is reasonable to assume the thinning rate is between -3 and 3 m/yr, to constrain the inversion. We combine all these 3 methods, and the final model is constrained better than each single method.

Barnes ice cap has been in a rapid retreat period since 2006 [*Gardner et al.*, 2012]. Techniques used in previous studies include DEM differencing [*Gardner et al.*, 2012], elevation postings from airborne and satellite laser altimetry [*Krabill*, 2011; *Gardner et al.*, 2011; *Gardner et al.*, 2012; Gardner et al., 2013; *Nilsson et al.*, 2015], surface mass balance model (SMB) [*Gardner et al.*, 2011; *Gardner et al.*, 2012] and satellite gravimetry [*Gardner et al.*, 2011; *Gardner et al.*, 2012; *Jacob et al.*, 2012; *Gardner et al.*, 2013; *Lenaerts et al.*, 2013]. Although all techniques conclude to generally consistent results, uncertainties such as post-glacial rebound, extent of ice cap changes through time, extrapolation of elevation posting data, mean glacier density, firn density, uncertainty of atmospheric correction on GRACE data, are sometimes not negligible [*Gardner et al.*, 2012].

Gardner et al. [2012] concluded the ice thinning rate between 2005 and 2011 at Barnes ice cap is ~1.2 m/yr, corresponding to the ice mass loss of 6.3 Gt/yr. Cryosat altimetry data suggests the annual winter-winter thinning rate between 2010 and 2014 is 2.7 m/yr [*Gray et al.*, 2015]. In this study, we present the method described above, and apply it to Barnes ice cap using Radarsat-2 data between 2012 and 2015. Our result confirms the previous conclusions that the rate of mass loss in this area is accelerating in recent years. Different from

altimetry methods, because the InSAR derived bed-rock displacement is directly related to mass change, our results are independent from firn density variation.

3.2. Background

Spanning ~150 km and ~60 km northwest to southeast and from southwest to northeast, Barnes ice cap (70N, 73W), located at the center of Baffin island, Canadian Arctic Archipelago, covers an area of about 5900 km^2 [*Sneed et al.*, 2008], exhibiting like a big ecliptic dome. It is the last remnant of Laurentia Ice Sheet from ~20000 BP, buried with the Canada's oldest ice [*Dyke et al.*, 1987]. The highest place on the dome is ~1000 m with ~400 m topographic relief to the foot (Figure 1). And the DEM of whole area is similar to a ramp with elevation increasing from south-west to north-east. The annual averaged melting days at Barnes increases from 66 days (1979-1987) to 87 days (2002-2010), and the present-day melting season starts at the end of May and ends at the end of September [*Florent et al.*, 2012]. A net accumulation of iced firn and superposed ice was found on the higher parts of the ice cap in 1980s [*Hooke et al.*, 1987], but in present days, this accumulation area is believed to be very limited [*Gardner et al.*, 2012; *Nilsson et al.*, 2015]. The ice thickness was ~550 m in 1960s with peak elevation of 1116 m at that time. Between 1970 and 1984, Barnes ice cap lost average of 1.7 m ice, corresponding to the thinning rate of 0.12 m /yr according to ground survey [*Sneed et al.*, 2008]. Between 1984 and 2006, the retreat speed increases, and the total ice thinning estimated from differencing the record at 1984 and satellite image at 2006 is ~16.8 m, corresponding to the thinning rate of

~0.76 m/yr, and the rate between 2004 and 2006 reaches ~1 m/yr [*Sneed et al.*, 2008]. Ice loss accelerated in 2005; the ice cap thinned by ~7.2 m until 2011, corresponding to ~1.2 m/yr annual thinning rate or 6.25 Gt/yr mass loss rate [*Gardner et al.*, 2012]. This acceleration is clearly recorded in the mass loss time-series inverted from GRACE data [*Gardner et al.*, 2012].

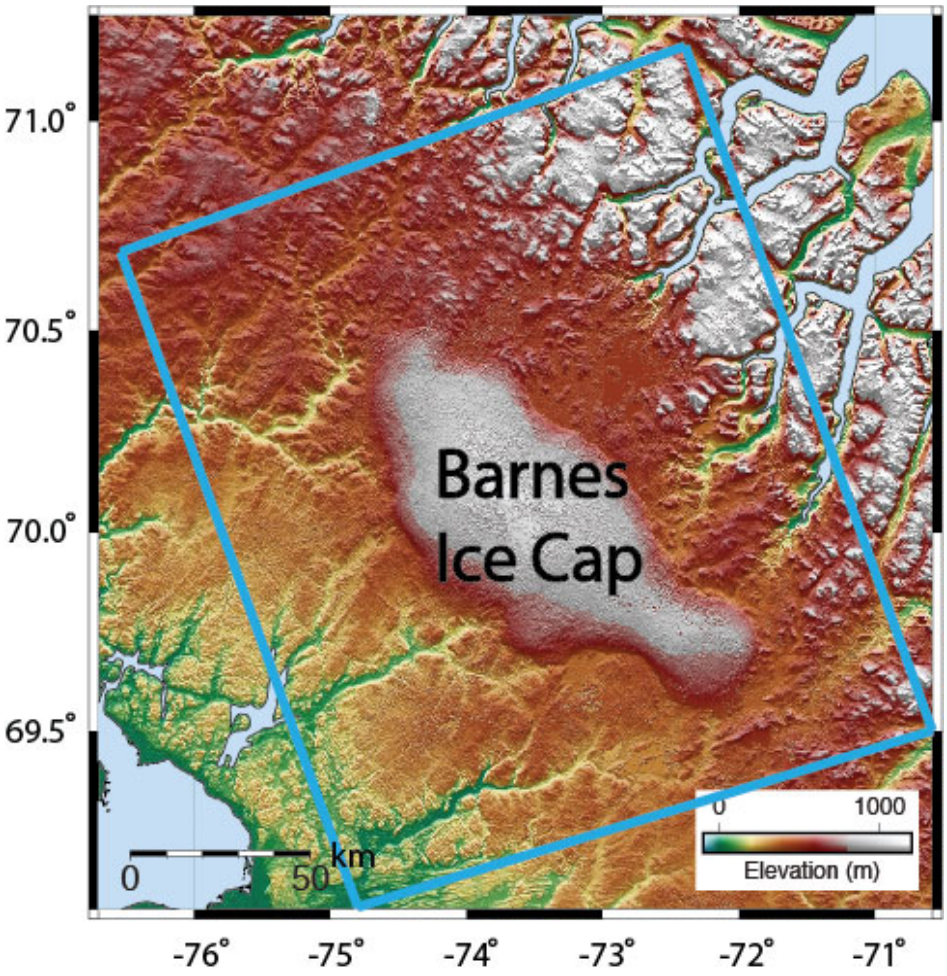

Figure 3.1. *DEM of Barnes ice cap. The blue frame draws the coverage of InSAR data.*

The last airborne laser altimetry campaign in this area (IceBridge ATM mission) was in 2011 [*Krabill*, 2011], and the GRACE data is limited by resolution

so that mass loss at Barnes cannot be distinguished from other glaciers on Baffin Bay. In this study, we apply our ice mass loss estimation method based on Radarsat-2 InSAR data between May 2012 and April 2015 at Barnes. And the results are compared with estimation from Cryosat data between 2010 and 2014.

3.3. InSAR analysis

We use 22 Radarsat-2 wide fine beam ascending imagery between May 2012 and April 2015 for this study. The original interferograms are processed by the Canada Centre for Remote Sensing with 7 and 14 looks in range and azimuth directions respectively, corresponding to ~33 m and ~73 m resolutions in the radar coordinates (a typical interferogram is shown in figure 2). Because of snow coverage in the winter, the maximum temporal baseline we choose is less than 2 repeat cycle (48 days), and for summer day we choose temporal baselines up to 2 years. With the threshold of 350 m for spatial baseline, we obtain 59 interferograms (figure 3).

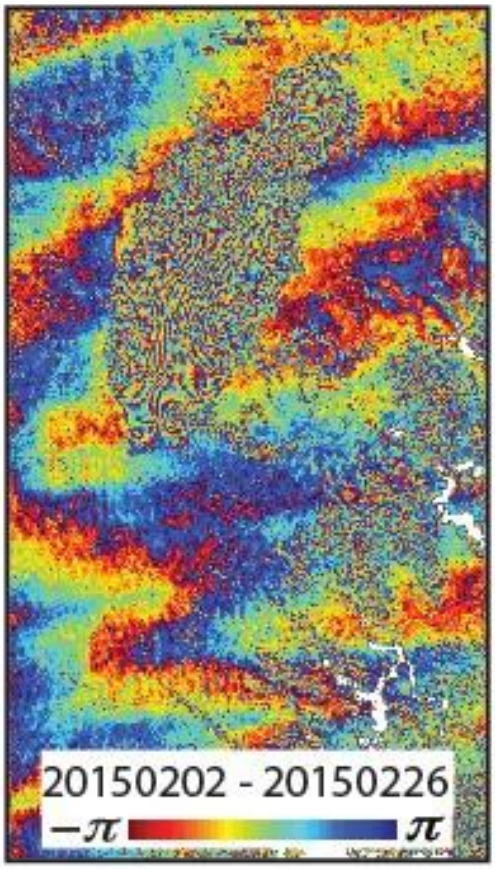

Figure 3.2. A typical interferogram (original) between 20150202 and 20150226.

Ice flow in spring is clearly retrieved.

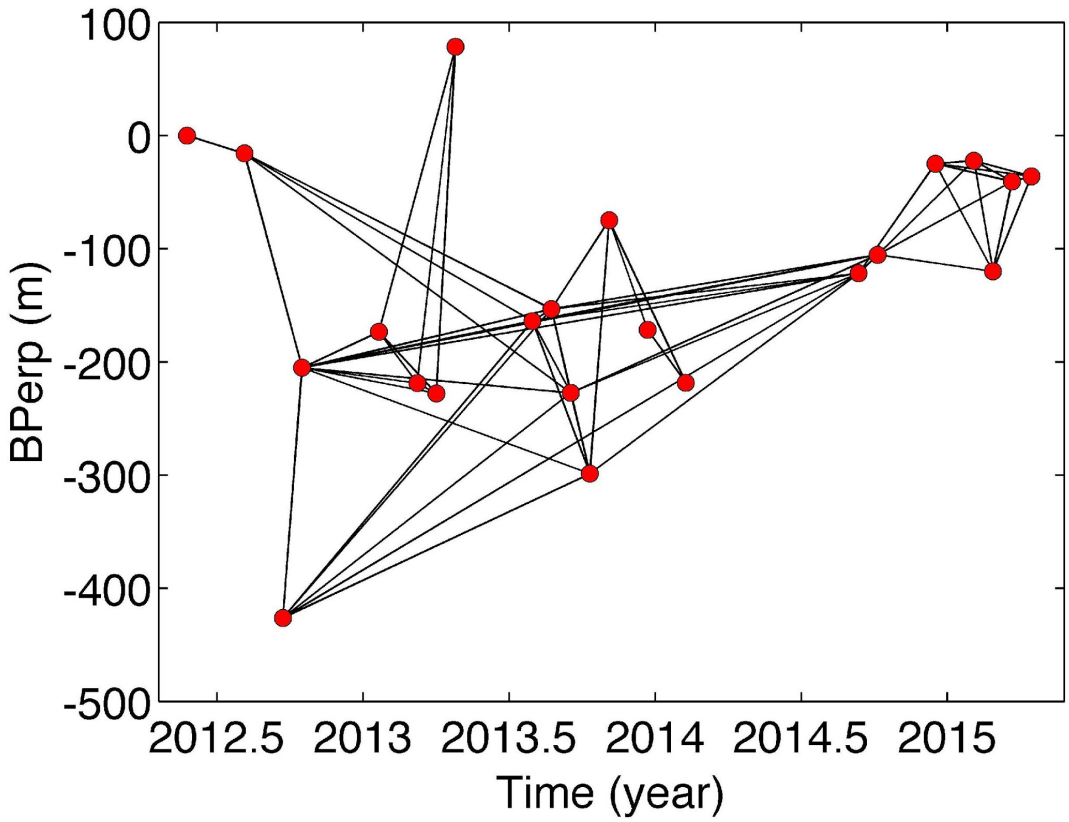

Figure 3.3. *Baseline plot of InSAR data (perpendicular baseline as a function of time). Information of all dates see Appendix A Table S1.*

We remove a second-order in range, first-order in azimuth ramp due to orbital uncertainty [*Samsonov et al.*, 2014]. Next, we also remove the DEM errors from both wrapped [*Ducret et al.*, 2014; *Zhao et al.*, 2015] and unwrapped phases [*Berardino et al.*, 2002; *Fattahi and Amelung*, 2013]. We multi-look the interferograms by a factor of 2 and apply an adaptive filter after the DEM error correction on wrapped phases in order to increase the signal-to-noise ratio, helping the unwrapping process. Phase unwrapping is based on the approach of *Chen and Zebker* [2000]. We retain only pixels with a spatial

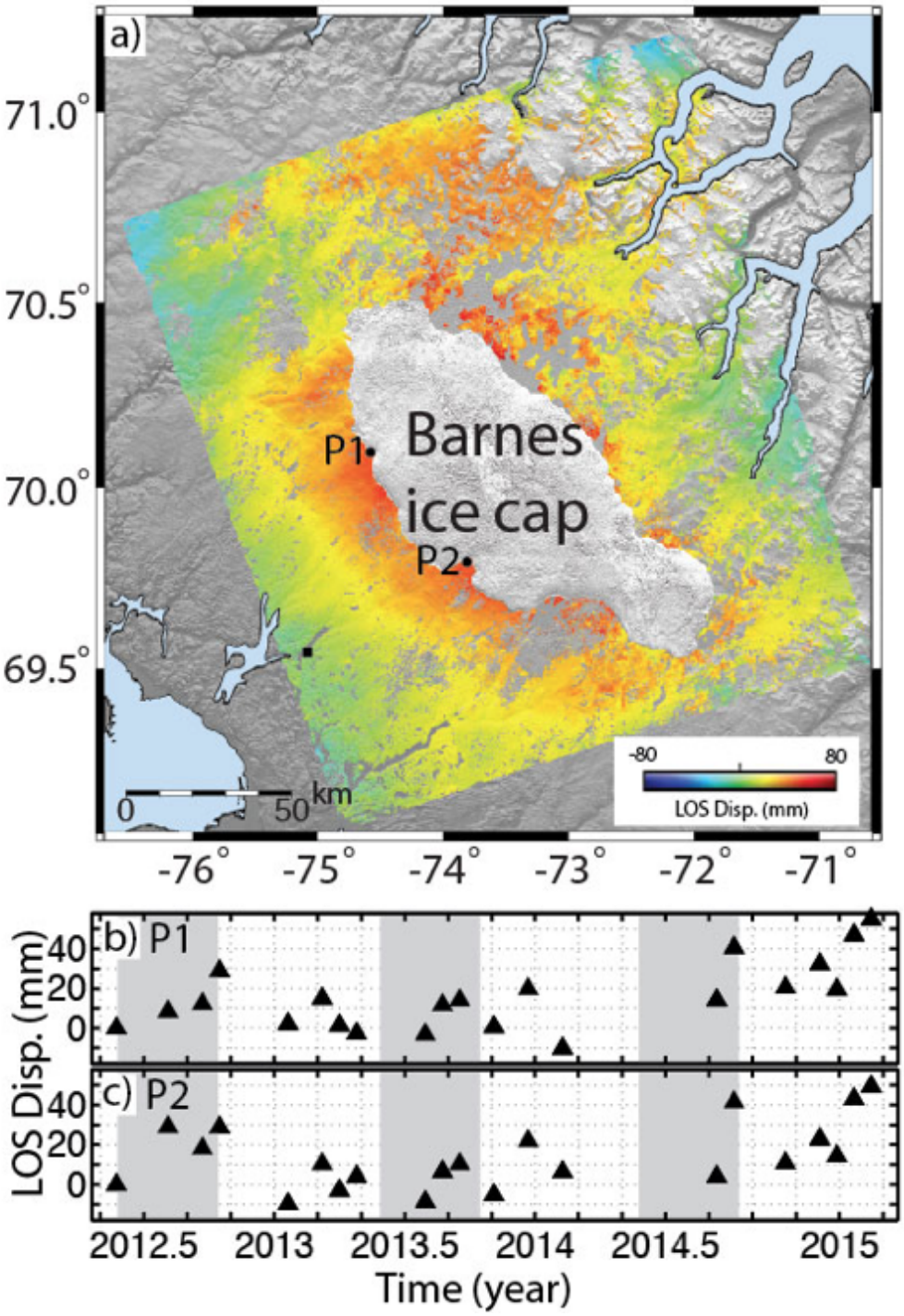

Figure 3.4. *InSAR LOS displacement map (May 24, 2012 – April 15, 2015). Solid square: reference point. b) and c) 2 time-series at the western flank of ice cap. Each tick on y-axis represents 2 months. Gray areas roughly illustrate the melting seasons.*

coherence larger than 0.1 in 40 percent of the interferograms [*Baker et al.*, 2012]. We reduce phase unwrapping errors of isolated areas using the nearest-neighbor interpolation method of *Agram et al.* [2009].The final time-series inversion is based on the small baseline (SB) InSAR approach [*Berardino et al.*, 2002].

3.4. Results

We show the total line-of-sight (LOS) displacement between the first (24 May 2012) and the last (15 April 2015) SAR acquisitions of our time-series. A red-to-yellow fringe embraces the ice cap, inferring the uplift (rebound) due to ice loss in three years. Up to 5 cm uplift is detected at the ice-rock margin (figure 3.4a). A reference point is chosen at bedrock along a water channel and far from the ice cap, in order to eliminate the effect of permafrost thawing and refreezing [*Lin et al.*, 2012; *Short et al.*, 2014]. Consequently, the green color represents stable ground (no deformation), and the blue color represents subsidence. On the eastern flank, the topographic relief is significant, and part of the area is covered by snow and proglacial lakes, indicating the potential of more residual phases due to decorrelation and tropospheric delays.

Displacement time-series of 2 points at the margin area show similar secular uplift trend as well seasonal fluctuations, uplift during summer (late May to late September) and subsidence for the rest of a year (Figure 4b, c). This seasonal variation also match the obervation from Cryosat altimetry (Figure 3.5., from [Gray et al., 2015]). Time-series at the western flank are noisier. So that only total displacement is used in modeling.

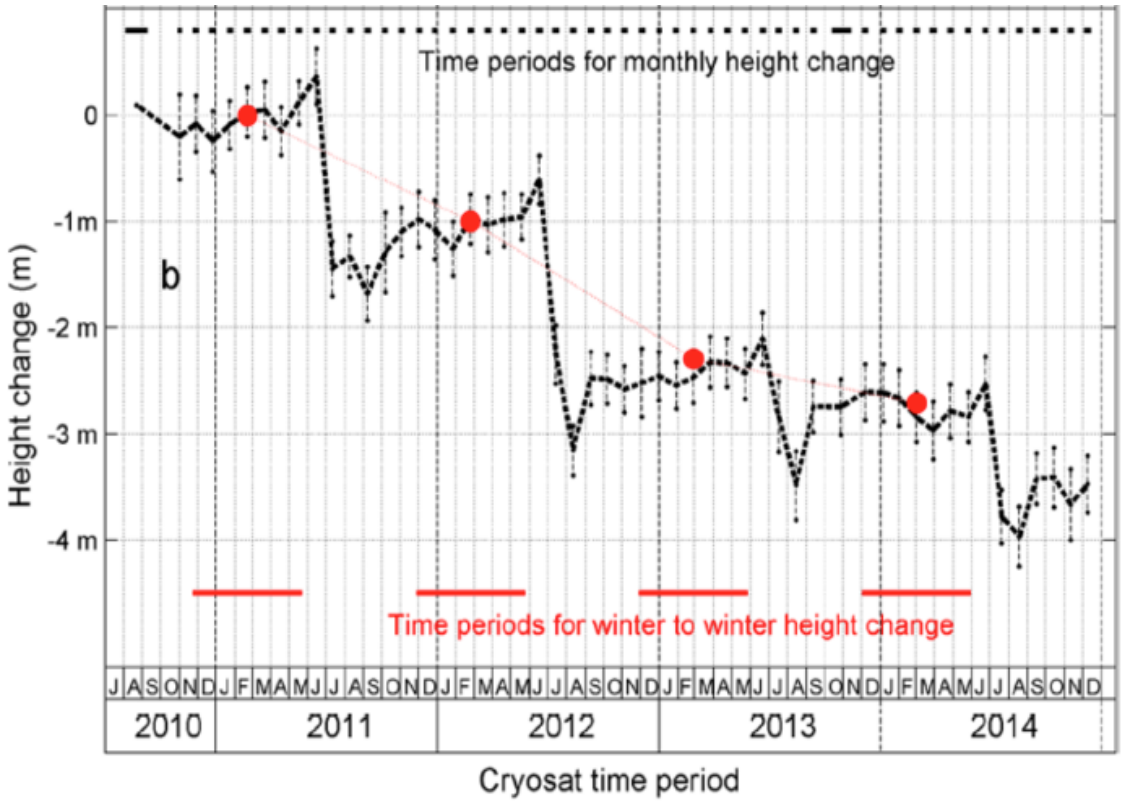

Figure 3.5. *(Figure 13. in Gray et al. [2015]) Elevation change at Barnes ice cap between 2010 and 2014, derived from Cryosat-2 altimetry. Each dot with error bar represents an observation of Cryosat-2. Red dots indicate the winter-to-winter height change calculated from the periods represented by the 4 red lines.*

3.5. Modeling

The elastic Green's function indicates that knowing the deformation (strain) and elastic parameters, one can infer the amount of force (stress) causing the deformation. However, in 2D problems, the sensitivity of deformation observation not directly on the ice is considerably low and the inversion becomes significantly under-determined, and the result is unstable. To overcome this problem, we present 3 solutions each of which provide some extra constraint

onto the inversion, and combine them together to obtain a final estimate of ice mass loss.

3.5.1. Methodology

3.5.1.1. Quad-tree resampling

Geophysical deformation usually exhibits an exponential characteristic, which means the amplitude of signal decreases exponentially from source to far field. According to this, displacements close to the source and displacement in the far field are of different sensitivity to the source change (here refers to ice mass change). We thus resample the InSAR observation using quad-tree method (Figure 3.6a,c), obtaining more samples close to ice cap and less in far field. The implementation is based on a threshold of local standard deviation. However, if we choose to resample the observation directly, the obtained tree usually contains many small blocks in the far field in case of noise. Because of this, we choose to use a pre-defined model (based on the exponential law in *Zhao et al.* [2014] and forward half-space model) to implement the resampling (threshold equals to 1 mm) and the observation is resampled accordingly. At the same time, we also resample the model space (Figure 3.6b,d, threshold equals to 0.25 m), so that the interior of the ice cap contains less blocks to be modeled, in order to reduce the error caused by under-determination.

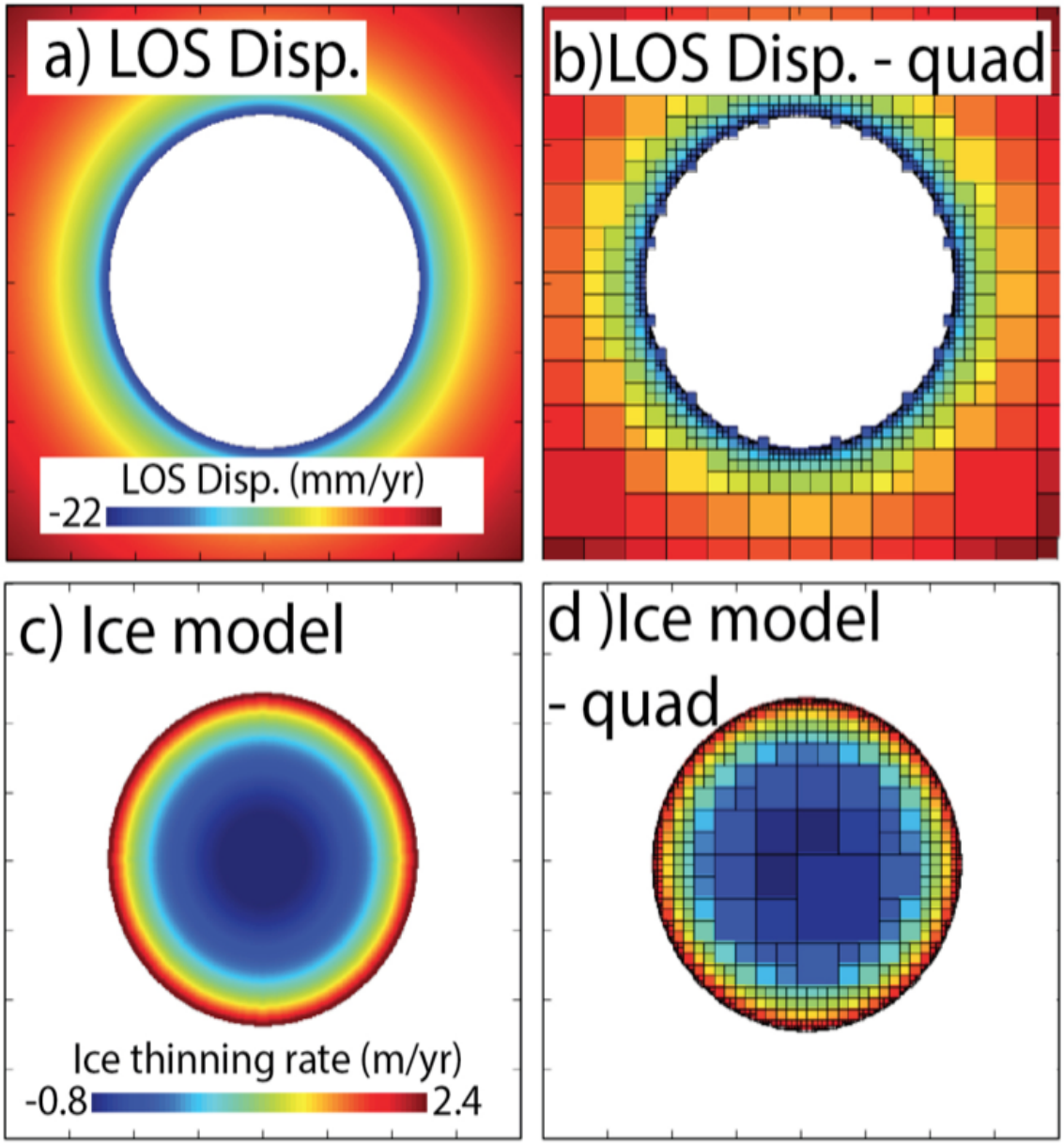

Figure 3.6. *a) A pre-defined displacement model (ice model uses (b)). b) A simulated circled ice thinning rate model whose value is exponentially correlated to the distance from the ice edge. c) Quad-tree resampling of a). d) Quad-tree resampling of b).*

3.5.1.2. Penalty function

Based on the quad-tree resampling, we further add the constraint that a thinning rate block should be “similar” comparing to its neighbors – the sum of squared difference between one block and its neighbors is as small as possible [*Lin et al.*, 2012]. Different from *Lin*’s formula, because of the quad-tree resampling, the number of neighbors is different for each block.

3.5.1.3. Constrained least-square

Constrained least-square is a term related to least-square and non-linear programming, which minimize the objective function and subjects results onto equality or inequality constraints. The common solution of this problem is using Lagrange multipliers (for equality) or Karush-Kuhn-Tucker conditions (for inequality) to convert the problem to be a system of linear equations, and then solve the problem by least-squares. [*Boyd and Vandenberghe*, 2004]

3.5.2. Results

We use homogeneous elastic Green’s function [*Farell*, 1972; *Graphenthin et al.*, 2006; *Zhao et al.*, 2014] to build the model with the three constraints introduced in last section. Young’s modulus and Poisson’s ratio are chosen at 60 GPa and 0.25 respectively. We also compare the result with a model based on the empirically exponential relation be ice thinning rate and distance from the ice edge [*Zhao et al.*, 2014]. These 2 models are shown Figure 3.7., with a) the empirically exponential method, b) the constrained least-square method. The

total ice loss estimated from the empirically exponential method and the constrained least-square method are 27.9±3.2 Gt and 32.9±4.3 Gt respectively, corresponding to 9.3 Gt/yr and 11.0 Gt/yr ice loss rates in the 2.9 years between May 24, 2012 and April 15, 2015. Considering there is usually significant precipitation in May [*Gray et al.*, 2015], the annual rate is likely with slight overestimate (less than 5%).

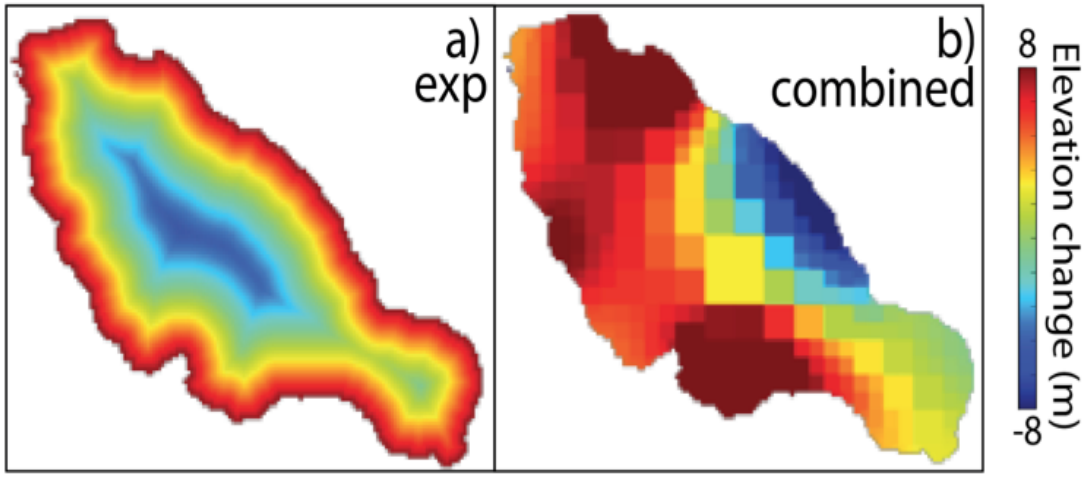

Figure 3.7. *a) Inverse model based on empirical relation between ice elevation change (equivalent to density at 917 kg/m^3, positive means ice thinning) and distance from the ice edge; b) Inverse model based on combination of the three constraints (in 3.5.).*

The pattern of ice elevation change is irregular, different from commonly lower thinning at center and higher at margin, with more ice thinning at the northern and western parts of the ice cap, and accumulation at the eastern margin. This is likely affected by the noises from observation. From the LOS displacement map (Figure 3.4a) and the model (Figure 3.7b), it is clear that the

areas with less uplift signals also have less ice thinning or even accumulation. The insight supports the general feasibility of the proposed method. However, the final result is biased by the low signal-to-noise ratio.

On the other hand, the model based on exponential assumption (Figure 3.7a) is regular. It is because of the very strong model assumption on the thinning rate pattern. From previous studies based on altimetry, DEM differencing, and gravimetry on the Canadian Arctic Archipelago [Gardner et al., 2011; Gardner et al., 2012; Lenaerts et al., 2013], we suggest this assumption is generally acceptable with minor exceptions. For example, at Barnes, the thinning rates are higher at the western flank, and lower in east. Also for big ice-sheet, this assumption is limited because of higher spatial heterogeneity of climate conditions and thinning rates.

3.6. Discussion

The result indicates that the ice loss rate between 2012 and 2015 is about 1.5 times of the amount between 2005 and 2011, suggesting the acceleration at Barnes since 2006 is still undergoing. *Gray et al.* [2015] suggest even higher winter-winter thinning rate at about 2.7 m/yr based on Cryosat-2 data. Part of the reason is perhaps snow-fall is absent from CryoSat-2 data [*McMillan et al.*, 2014]. Our results are consistent with observations of ice cap extent using optical images [*Li et al.*, 2014] that Barnes is in a rapid retreating period.

By comparing the displacement map with the ice thinning rate model between 1960 and 2010 [*Gardner et al.*, 2012], we find similar pattern – high

uplift at the areas with high ice mass loss. The ice loss in the west of the ice cap is generally larger than the eastern part. This is likely due to the elevation difference, the area lower than 700 m in the west is much larger than in the east, causing the temperature difference. Decorrelation is the main error source in this study. Because of snow with wet surface, decorrelation is significant sometimes even on 1 repeat cycle interferogram (24 days). Summer-summer pairs are better but part of which are affected by thawing permafrost.

Gardner et al. [2012] and *Nilsson et al.* [2015] all suggest to use a simplified ice density model, which assuming a constant ice density of 900 kg/m^3, ignoring firn density and firn compaction. This assumption is valid based on the conclusion that summer melting dominates the ice mass balance in this area [*Gray et al.*, 2015]. However, there is still certain amount snow accumulation between the melting seasons [*Gray et al.*, 2015], and the effective density (the apparent density when the elevation change is a combination of snow and ice) is important for non-summer-summer (start or end time is not in summer) observations. Our method directly model the mass change, and thus doesn't have this concern on effective density.

3.7. Conclusion

We use SB-InSAR time-series analysis for Radarsat-2 data from May 2012 to April 2015 to detect the crustal deformation due to ice mass loss in the vicinity of the Barnes ice cap. The results show up to 5 cm LOS uplift at the margin of the ice cap between the first and last SAR acquisitions. The uplift is

explained by a new model based on three additional constraints in the linear inversion. The model result in the estimate of ice mass loss at Barnes ice cap during the 2.9-year study period which is 32.9±3.2 Gt, corresponding to 11.3 Gt/yr ice loss rate. We compare the model with a model based on an empirical model describing the exponential relation between ice loss and the distance from ice edge, and reach similar results. This ice loss rate is ~1.5 times of the previous estimate between 2005 and 2011. It indicates that the acceleration at Barnes since 2006 has not stopped. The estimate depends on the choice of half-space modulus and seasonality of ice mass balance. Moreover, the performance of modeling highly depends on the observation signal to noise ratio.

Chapter 4

Inhomogeneous firn density distribution inferred from InSAR at Petermann glacier, Greenland

Summary

Altimetry derived ice volume change requires accurate density measurement for the conversion to mass change. While because of different snow ice distribution and interaction over ice sheets, this density is not constant and is usually significantly different from pure ice density at the margin of ice sheets, and even sometimes larger than ice or smaller than snow densities. In this study, we use InSAR to sense spatial variations of the effective density at the margin of an ice sheet. We use 2003-2010 Envisat imagery to generate glacial rebound map (LOS displacement rate) through InSAR time-series analysis. Up to 3 mm/yr LOS displacement is detected in the bedrock area next to Petermann Glacier. We use

Icesat derived ice volume change to model this displacement signal. The observed bedrock displacements can not be explained using homogeneous firn density, but are consistent with a manually modified density model. The prefered density model has effective density larger than one close to the upper stream of Petermann because of snow accumulation and ice flow. We found better fit using the later one as well as a more reasonable half-space Young's modulus of 70 GPa for Greenland ice sheet. This suggest that space-geodetic observations of bedrock displacement at the ice sheet margin combined with elevation change observations can sense spatial variations of the effective ice density at the ice sheet margin.

4.1. Overview

Radar/laser altimetry derived ice-sheet surface elevation changes require the associated density in order to obtain ice mass change. However, the elevation change is a combination of different processes including ice dynamics, firn densification, and change in accumulation rate. Ice dynamics affect the vertical thickness of ice which is mainly measured based on the velocity from synthetic aperture radar interferometry, and the density is ~900 kg/m^3. Firn densification is a process that snow, sometimes partially melted snow, controlled by gravity, interacts with lower layer snow or snow ice compound to increase density and get compacted in elevation. Change in accumulation refers to the new snow. Because the densities in these 3 processes are different, the final

density applied on the ice-sheet volume change is a combination of all of them, hereafter called “effective density” [*Slobbe et al.*, 2009].

The effective density sometimes varies between the densities of snow and ice. It also can be smaller than the snow density (e.g. thinning due to ice dynamics is between 1 and 2 times of snow accumulation, assuming ice density of 900 kg/m^3 and snow density of 300 kg/m^3) and larger than ice density (e.g. thinning due to ice dynamics is between 0 and ⅔ of snow accumulation), and the range of variation is possibly very wide [*Li et al.*, 2011, *Kuipers Munneke et al.*, 2015]. Figure 4.1. shows 2 example effectives densities. In a), the snow accumulation rate is 1 m/yr, and the ice thinning rate (due to dynamics or melt) is 2.5 m/yr. The altimetry derived elevation change is -1.5 m/yr, and the effective density is 1300 kg/m^3. In b), the snow accumulation is 2.5 m/yr, and the ice thinning rate is 1 m/yr. The altimetry derived elevation change is 1.5 m/yr, and the effective density is -100 kg/m^3. It is reasonable to assume the effective density is dependent on season, e.g. in the summer there is less snow and the effective density is close to ice; in the winter, there are more snow, so that there are more density variations.

Early studies usually used a constant between snow and ice densities (300 and 900 kg/m^{-3}) to convert ice volume change to mass change. For example, *Davis et al.* [2005] used 350 kg/m-3 as the average density; *Thomas et al.* [2006] used 300 kg/m-3 for the interior of the ice sheet and 900 kg/m-3 for the ice margin. *Wingham et al.* [2006] used 350 kg/m^3 and 917 kg/m^3, respectively. However, two values for the interior and margin of ice sheets are too coarse for

accurate mass balance study. Figure 4.1. explains the assumption that the effective density is between snow and ice densities easily breaks, and the difference from assumed value and true value can be significantly large (sometimes in opposite signs, Figure 4.1.b).

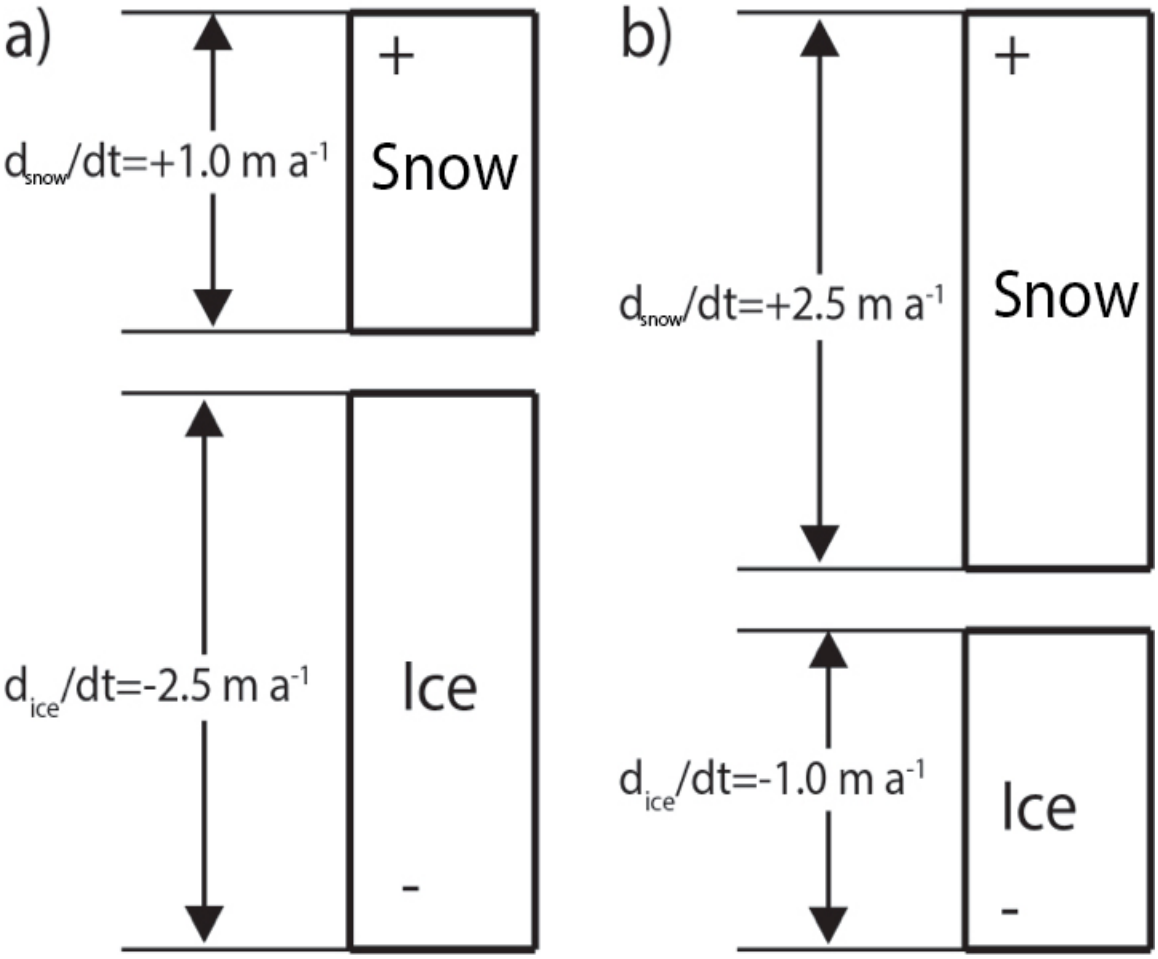

Figure 4.1. *(Modified from Fig. 1 in Li and Zwally, 2011). Illustration of effective ice density (ρ_{eff}), assuming ice density (ρ_{ice}) of 900 kg/m^3 and snow density (ρ_{snow}) of 300 kg/m^3. a) ρ_{eff}= 1300 kg/m^3 > ρ_{ice}; b) ρ_{eff}= -100 kg/m^3 < ρ_{snow}.*

Physical models on firn compaction [*Zwally et al.*, 2011; *Li and Zwally*, 2011; *Sorensen et al.*, 2011; *Khan et al.*, 2014] were used for volume-mass

conversion studies, which are based on regional climate models including BOX [*Box 2013*; *Box et al.*, 2013], MAR [*Fettweis et al.*, 2011], RACMO2 [*Ettema et al.*, 2009], HIRHAM [*Christensen et al.*, 2006] and another model introduced by *Hanna et al.* [2011]. However, there is no feasible tool to validate these models [*Sorensen et al.*, 2011].

We present here a study using InSAR derived surface displacements and altimetry derived ice volume change to validate the firn density model constrained from Regional Climate Models (RCM). With advantage of high spatial resolution, InSAR derived deformation is specially sensitive to the mass change at the ice sheet margin, and is thus useful for the validation of different firn density models at Petermann glacier, Greenland, with known ice volume change from altimetry products. We use Envisat ASAR imagery between 2003 and 2010. After time-series analysis, velocity maps obtained from both ascending and descending tracks are sensitive to the mass change at the ice sheet margin. We use Icesat-1 and the IceBridge mission for ice volume change estimation, which have proved to be high quality.

4.2. Background

Petermann glacier located in northwest Greenland (Figure 4.2). It is the biggest glacier in north Greenland, with the longest (70 km long and 20 km wide [*Rignot and Steffen*, 2008]) outlet tongue in the northern hemisphere, draining about 6% of the Greenland ice sheet area [*Falkner et al.*, 2011]. The ice stream thickness is ~600 m [*Rignot and Steffen*, 2008] at the grounding line (about 30

km from beginning of outlet) [*Rignot and Steffen*, 2008], with a 60 m ice shelf [*Allen et al.*, 2010]. Petermann's ice front was first mapped by the British Arctic Expedition in 1876 [*Falkner et al.*, 2011], and it retreated after that with several major calving events: 1959-1961 (~153 km^2), 1991 (~168 km^2), 2001 (~71 km^2), 2008 (~31 km^2), and 2010 (~270 km^2) [*Johannessen et al.*, 2011]. Calving and basal melting are thought to be the main reason causing ice mass loss at Petermann [*Rignot and Steffen*, 2008; *Johnsson et al.*, 2011; *Johannessen et al.*, 2011]

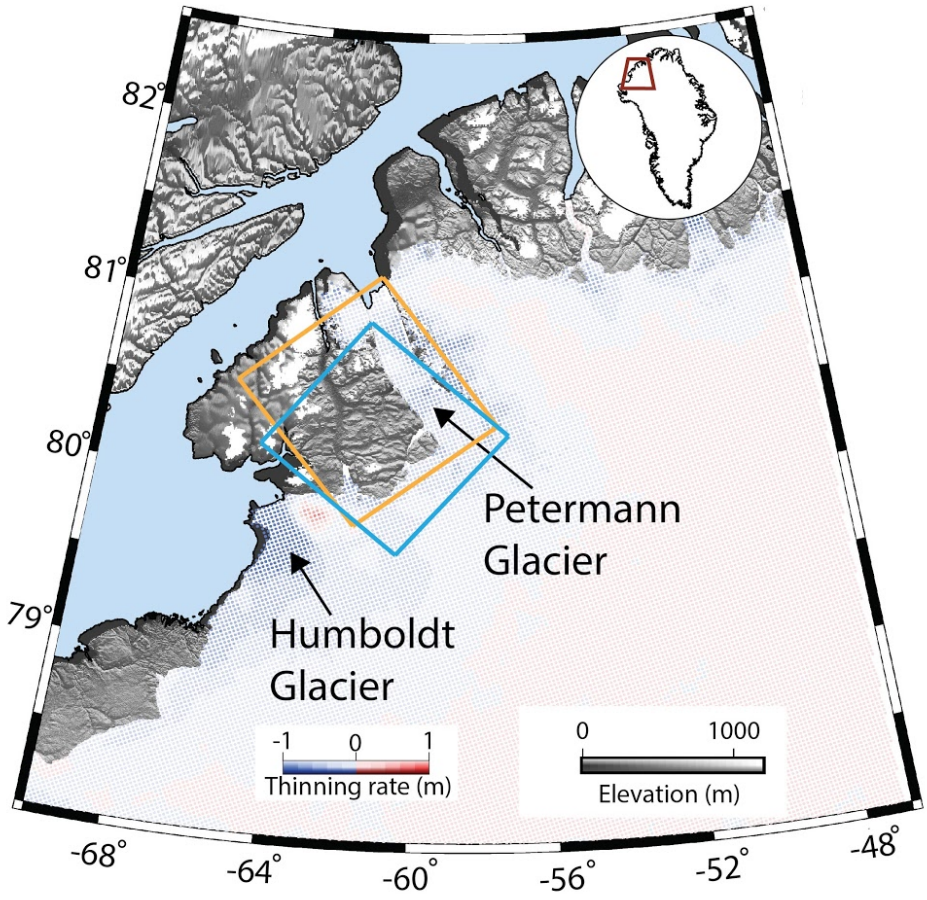

Figure 4.2. *Study area – Petermann glacier. Shaded relief background is topography at Petermann. The topography on Greenland is from a 30 m DEM combining ASTER, SPOT-5 DEMs and AVHRR photoclinometry [Howat et al.,*

2014]. The topography on the Ellesmere island, Canada (north-west corner of the map) is from ASTER global DEM v2 (30 m) [Fujisada et al., 2012]. Colored map represents the interpolated Icesat-1 thinning rates. Blue and orange frames represent the coverage of descending and ascending InSAR data, respectively.

The ice thinning rates at Icesat footprints are shown in Appendix B. Noise is higher at the ice margin area than the interior ice sheet. After combining with ATM (laser altimetry, 2003, 2005-2010) and LVIS (laser altimetry, 2009-2010), and interpolation, the ice thinning rates are more continuous in spatial without big variations in short distance (Figure 4.2). Large amount of thinning occurs at several small outlet glaciers along the north-east margin of the ice stream of Petermann glacier. Another larger thinning is found at the western edge of Humboldt glacier, caused by the speeding up of ice flow. Instead, the eastern edge of this glacier, where ice used to move faster, slowed down in the study period causing a positive dynamic ice mass balance (see the dark red area in Figure 4.2, and Appendix B). Dynamic ice mass loss is not significant at Petermann glacier [*Joughin et al.*, 2010]. And because of the dry weather in this area, precipitation is negligible except the area close to ice stream, and runoff is the dominated factor of SMB [*Ettema et al.*, 2009]. The highest speed of Petermann's ice stream is about 1000 m/yr, which has been stable since 1996 [*Rignot and Kanagaratnam*, 2006; *Rignot and Steffen*, 2008; *Joughin et al.*, 2010], under the background that Greenland's outlet glaciers are speed-up generally. As a result the mass loss as Petermann is dominated by surface mass balance (SMB). In a sub decadal scale, in the whole basin including Petermann

glacier, the dynamic mass loss is negative for periods 2003-2006 and 2009-2012, and positive for period 2006-2009 [*Khan et al.*, 2014]. SMB is relatively unchanged in these periods, leading to a significant mass balance difference before and after 2006 [*Khan et al.*, 2014].

4.3. InSAR data and analysis

4.3.1. Data processing

We use 53 and 32 Envisat ASAR imagery from descending and ascending tracks between April 2003 and September 2010 for this study. We remove interferograms whose perpendicular baselines are larger than 300 m or whose temporal baselines are larger than 3 years, and obtain 162 and 93 interferograms for descending and ascending tracks.

We use ROI_PAC software [*Rosen et al.*, 2000] for interferometric processing and small baseline InSAR [*Berardino et al.*, 2002] technique for the time-series analysis. The reference topography is generated from a 30 m DEM combining ASTER, SPOT-5 DEMs and AVHRR photoclinometry [*Howat et al.*, 2014], and is removed after raw interferogram generation. Next we remove localized DEM errors from the wrapped interferograms following *Ducret et al.* [2014]. In this step, we include some interferograms with perpendicular baseline longer than 300 m, which are more sensitive to the DEM errors. Next, we take additional looks to obtain ~80×80 m^2 pixels, apply an adaptive filter, and unwrap the phases based on the statistical-cost network-flow approach [*Chen and Zebker*, 2000]. To avoid influences from decorrelated pixels, we select pixels with

a spatial coherence larger than 0.2 in 60 percent of the interferograms [e.g. *Baker and Amelung*, 2012; *Zhao et al.*, 2015]. We further use a nearest-neighbor interpolation method introduced by *Agram et al.* [2009] to resolve the problem of isolated area after pixels selection. After phase unwrapping, we implement time-series analysis [*Berardino et al.*, 2002] and DEM error correction [*Fattahi and Amelung*, 2013] to obtain the final results.

4.3.2. Results

InSAR LOS velocity maps are presented in Figure 4.3a,b, both of which show an uplift gradient from glacier (upper ice stream) to far field, with 5 mm/yr relative LOS uplift at the margin area (the azimuth angle, ~45 degree, at polar region is larger which transfers about doubled horizontal motion into LOS. However, the major motion in the study area is in vertical direction, this difference is ignorant). Similar patterns from Descending and ascending track suggest that the deformation is mainly vertical, inferring that it is likely due to surface mass change. The results from ascending track are generally noisier than descending track because of less SAR acquisitions (32 images). Figure 4c show 2 InSAR time-series (descending and ascending) at Site SCBY, a continuous GPS station installed in 2007. Both time-series show about 2-3 cm LOS displacement in 6-7 years, representing LOS velocities of 3-5 mm/yr (with ~2 cm seasonal variability). The absolute vertical velocity at SCBY measured by GPS is 11 mm/yr, and the 6-8 mm/yr difference between InSAR relative and GPS absolute displacement is likely due to the background deformation, which can be long wavelength

response to the mass change for interior ice sheet, and the glacial isostatic adjustment (GIA) signal. The long wavelength present-day elastic uplift rate at the study area is about 2-3 mm/yr, and the GIA signal is about 3-4 mm/yr [*Spada et al.*, 2012]. This value matches our estimate from InSAR-GPS differentiation, suggesting InSAR is able to retrieve much more details about red-rock deformation at local scale.

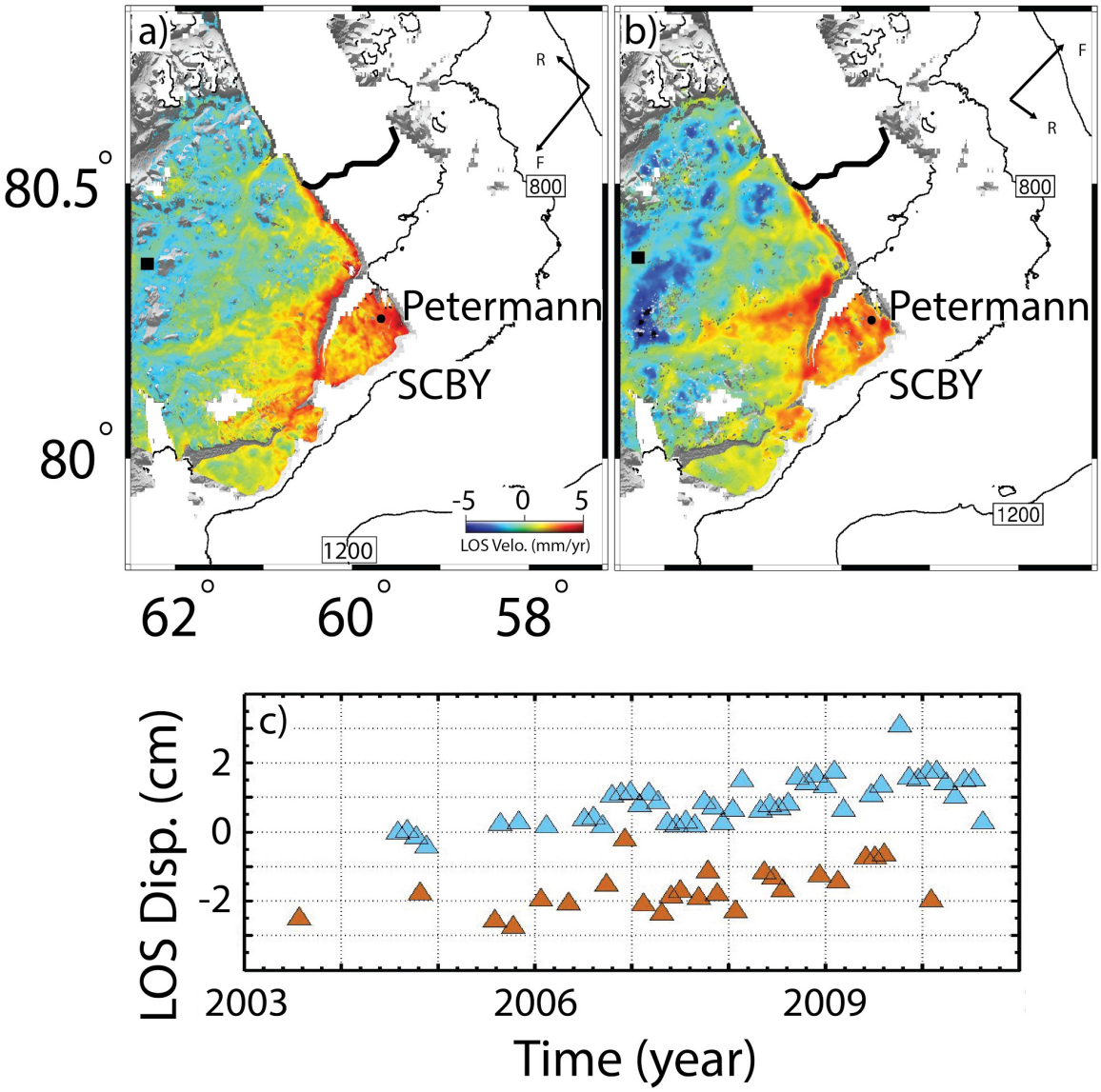

Figure 4.3. *a), b) Descending and ascending tracks velocity between 2003 and 2010 (descending track starts from 2004). Black square represents the reference point, SCBY stands for the location of the continuous GPS station. Arrows with characters F (flight) and R (range) represent the directions of flights and SAR LOS. c) InSAR LOS time-series at SCBY. Blue and orange triangles represent descending and ascending tracks respectively. Contour lines of elevation are shown on the ice sheet.*

4.4. Modeling and results

We use homogeneous half-space model [*Farrell*, 1972; *Graphenthin et al.*, 2006], which has been proved to be similar to layered model when load is at the scale of several tens of kilometers [*Graphenthin et al.*, 2006; *Nof et al.*, 2012; *Zhao et al.*, 2014], to simulate the observed displacements. Ice volume change is based on interpolated Icesat data (Figure 4.4a) on UTM coordinates, and density is assumed to be 917 kg/m^3. We assume Poisson's ratio is insensitive to dominantly vertical displacements [*Nof et al.*, 2012; *Zhao et al.*, 2015]. We thus assume Poisson's ratio of 0.25, and invert for the half-space Young's modulus.

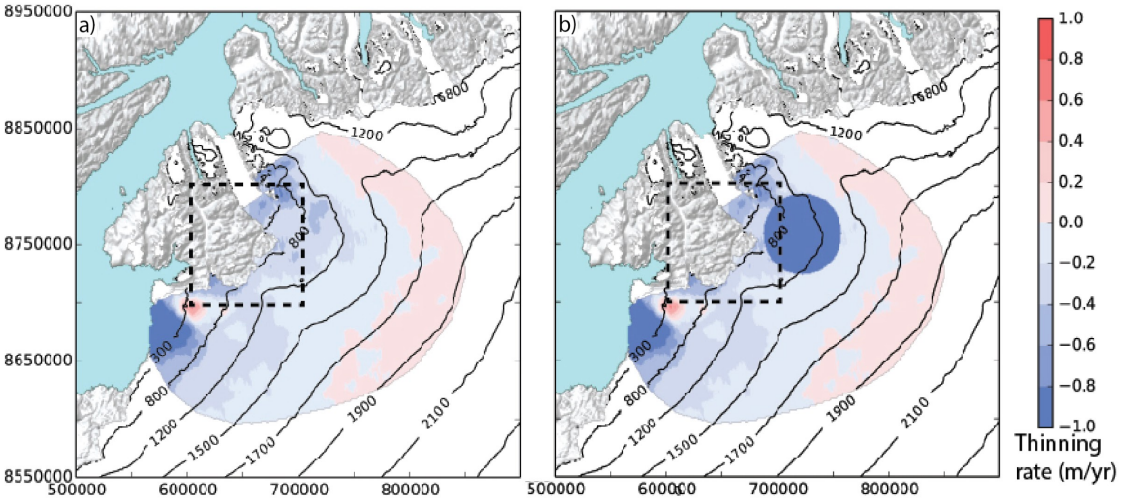

Figure 4.4. *Ice thinning rate model used in this study (2003-2010), a) interpolated from Icesat elevation change data, b) with an extra disk (represent an area with effective firn density tripled to ~2700 kg/m^3) at the west flank of Petermann, close to upstream. Dashed rectangle: the coverage of Figure 4.5. Positive values represent accumulation and negative values represent thinning.*

The preferred model is presented in Figure 4.5, with a), b) data, c), e) models and g), i) residuals for the descending and ascending tracks respectively. We obtain a Young's modulus of 50±8 GPa, and the standard error is calculated from linear error propagation. The root mean square error (RMSE) for descending track is 1.2 mm/yr. While the RMSE for ascending track is 1.5 mm/yr.

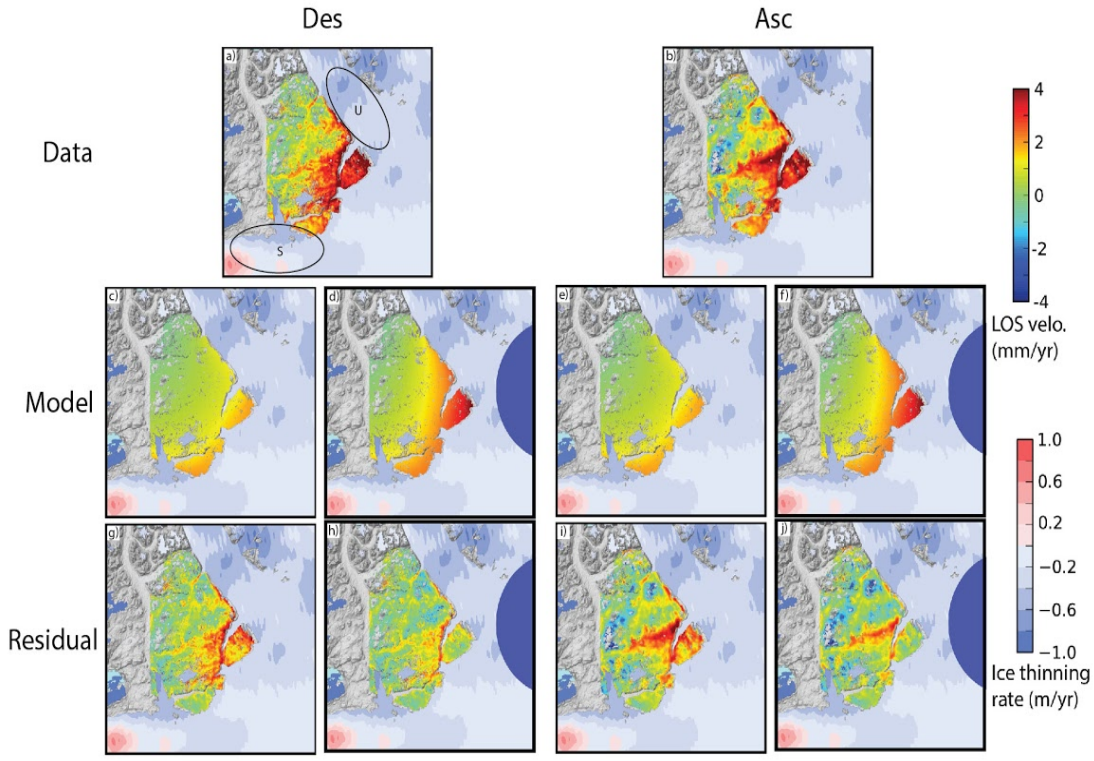

Figure 4.5. *a), b): Descending and ascending InSAR LOS velocities between 2003 and 2010. c), e): Preferred elastic half-space models for both tracks, with Poisson's ratio of 0.25 and best fit Young's modulus of 50 GPa. d), f) preferred models for ice thinning model with an extra disk with best fit Young's modulus of 70 GPa. g), i): Residuals between data and models c, e. g), i): Residuals between data and models d, f. The blue-red background colors on the ice sheet represent the ice thinning rates, with positive representing accumulation. Areas "U", "S" represent upper stream and southern areas used in later sections.*

The homogenous models (Fig. 4.5c,e) overpredict the displacements at the southern part of study area (area S in Fig. 4.5a), because from InSAR, ice mass loss more concentrates at the area close to the ice stream. One possible

explanation is that the effective density for the ice loss close to upstream is higher than pure ice density (because of the opposite elevation changes for firn accumulation and ice loss) (Figure 4.1a); or the effective density for the ice loss to the south of Petermann glacier is lower than ice density (Figure 4.1b); or the effects on both cases.

We define 2 special areas. One area is ice stream area which includes the upstream of Petermann (area U in 4.5a) and surrounding glacier area within 10 km. Another is “southern zone” which includes the southern margin of Petermann glacier and northern part of Humboldt glacier (area S in 4.5a). Ice flow velocities indicate no annual dynamic mass change at upper stream area and small accumulation in southern zone [*Joughin et al.*, 2010]. SMB includes 2 main sources, which are runoff and precipitation. Both upper stream and southern areas have highest rates of runoff because they are close to the ice sheet margin with similar elevation. But from precipitation data, upper area has significantly higher accumulation rate than southern area.

By summarizing all information above, we conclude that in upper stream area, there exists positive volume change due to precipitation with density close to pure snow (300 kg/m^3) (less firn in this area because of glacier motion), and negative ice mass change due to runoff with density close to pure ice (900 kg/m^3). We use averaged SMB data between 1958 and 2007 to make a rough calculation, assuming precipitation is mainly snow (94% of the precipitation on the Greenland ice sheet is snow [*Ettema et al.*, 2009]) with density of 300 kg/m^3 and runoff is mainly water with density of 1000 kg/m^3. With ~0.3 m/yr

precipitation (snow, 300 kg/m^3) and ~0.7 m/yr (ice, 900 kg/m^3) runoff in ice stream area, we obtain the effective density at ~1500 kg/m^3. Considering the rapid ice loss acceleration after 1990s [*Ettema et al.*, 2009; *Jiang et al.*, 2010; *Bevis et al.*, 2012], the effective density in ice stream area can easily double the pure ice density (917 kg/m^3). For southern area, because the accumulation rate is negligible, and dynamic ice loss has similar density with runoff, the effective density is close to the pure ice density.

The findings in the previous paragraph infers that the effective density of ice volume loss close to the up stream of Petermann glacier is likely significantly underestimated. We thus add a 35 km radius disk with extra ice thinning rate of 1 m/yr next to the upstream (Figure 4.4b). It is equivalent to triple the effective density considering the real thinning rate in this area is close to 1 m/yr.

The preferred model is presented in Figure 4.5, with d), f) models and h), j) residuals for the descending and ascending tracks respectively. With fixed ice thinning rate, density (pure ice), and a simple half-space model, we obtain a Young's modulus of 70±5 GPa, and the standard error is calculated from linear error propagation. The root mean square error (RMSE) for descending track is 0.7 mm/yr. While the RMSE for ascending track is 1.1 mm/yr. According to the previous studies on constraining Young's modulus from surface loading [*Grapenthin et al.*, 2006; *Nof et al.*, 2012; *Zhao et al.*, 2014], the effective half-space Young's modulus is between 40 GPa and 80 GPa for the load radius between 40 km and 70 km. Considering the load size of Petermann glacier, the 70 GPa half-space modulus is more realistic than 50 GPa. Moreover, we obtain

better fit after adding the extra disk, which supports our hypothesis that the effective density in ice stream area is higher than the southern zone.

4.5. Discussion

4.5.1. InSAR derived velocities

InSAR velocities detect up to 5 mm/yr LOS surface displacement at the ice-rock margin of Petermann glacier between 2003 and 2010. The ascending track is noisier than the descending track because of less SAR acquisitions being used for the time-series analysis. Although part of the seasonality can be seen from time-series, the currently accuracy is not enough to fully solve the response due to seasonal mass changes. The remaining errors include atmospheric delay, and decorrelation. In large scale (50-100 km) InSAR is able to retrieve the glacial rebound signal clearly with tremendous spatial details that cannot be found from coarse resolution whole Greenland elastic deformation maps [*Spada et al.*, 2012; *Nielsen et al.*, 2014]. Moreover, our preferred model suggests up to 10 mm/yr displacement at the ice margin. Because the present-day vertical uplift in this area is close to a constant within 5-6 mm/yr based on ICE5G-VM2 (ignoring difference between vertical and LOS), we conclude that our observation is dominantly elastic response inferred from the difference between absolute displacement from preferred model and relative displacement from InSAR. By averaging InSAR velocity, the amount (3-4 mm/yr) is also close to other predictions in this area.

4.5.2. Effective density

The theory of effective density that the ice thinning is a combination of snow/firn accumulation, dynamic ice motion, and ablation (runoff and evaporation/sublimation) has been demonstrated in *Li and Zwally* [2011]. However, at local scale (up to 200 km), the spatial variation of effective densities is hard to detect. This study introduces a potential tool to validate if the effective density varies in a certain area.

According to altimetry data, the ice thinning rates at ice stream area and southern zone of Petermann glacier are similar. But according to ice flow [*Joughin et al.*, 2010] and SMB [*Ettema et al.*, 2009] (including runoff and precipitation) data, these similar thinning are caused by different sources. In ice stream area (area U in Fig. 4.5a), the thinning is a combination of snow accumulation and runoff. While at southern zone (area S in Fig. 4.5a), the thinning is a combination of dynamic thickening and runoff. Because the density of accumulating snow and dynamically thickening ice are quite different, the effective densities in these 2 areas are thus different. We conclude that the effective density near Petermann glacier is close to triple of ice density (~2700 kg/m^3, inferred from historic data without accurate estimate from current observations), and the effective density at southern zone is likely close to ice density.

4.6. Conclusions

1) We use Envisat ASAR 2003-2010 InSAR data to obtain the surface velocities at the bed-rock area close to Petermann glacier. Up to 5 mm/yr relative LOS uplift is detected at the ice margin. This velocity result matches previous study in Greenland indicating 3-4 mm/yr averaged velocity in this area. Absolute displacement from model suggests there is a 5-6 mm/yr background uplift which matches the prediction of present-day post-glacial rebound.

2) A homogeneous ice density model doesn't fit the observation very well in the south (area S in Fig. 4.5a) of our observed area We propose a density model with increased density (representing by increasing thinning rate) close the upstream of the glacier. The new model fits the observation better obtaining a reasonable half-space Young's modulus at 70±5 GPa. The new model with density heterogeneity can be evidenced by dynamic ice motion and SMB data qualitatively. However, the accurate geometry of the density distribution is hard to be constrained, we don't present a quantitative solution in this study.

Chapter 5

InSAR observations of lake loading at Yangzhuoyong Lake, Tibet: constraints on crustal elasticity

Summary

We use Envisat 2003-2010 InSAR imagery over Yangzhuoyong Lake in southeastern Tibet to study the elastic response of the Earth's crust to variations in lake level. The net lake level drop during our study period is ~3 m with seasonal variations of more than 1 m. The time-series close to the lake center shows a high correlation with the lake level history. Near the lake center the unit response with respect to lake level change is 2.5 mm/m in radar line-of-sight direction, or ~2.7 mm/yr in vertical direction, corresponding to a vertical response of ~4.3 mm/Gt load change. We show that the observations are most sensitive to the elastic properties of the crust in the 5-15 km depth range and explain them with a layered elastic half-space model with a Young's modulus of 50±9 GPa Young's modulus in the top 15 km of the crust and using moduli inferred from seismology at greater depth. The inferred Young's modulus is ~25% smaller than the seismic modulus, which we attribute to damaged rock and the presence of fluids.

5.1. Overview

The Young's modulus is the elastic material property determining the elastic response of the Earth to surface, including seasonal, episodic and long-term glacial loading [*Graphenthin et al.,* 2006, *Auriac et al.,* 2014, *Zhao et al.*, 2014], lake loading [*Cavalie et al.,* 2007; *Nof et al.,* 2012; *Wahr et al.*, 2013, *Doin et al.,* 2015], river loading [*Bevis et al.,* 2005], ocean tide loading [*Ito and Simons*, 2011] and loading by seasonal variations of terrestrial water storage [*Steckler et al.*, 2010; *Fu and Freymueller*, 2012; *Fu et al.*, 2012; *Chanard et al.*, 2014].

At the confining pressures in the lower crust and mantle, Young's modulus can be inferred from seismic wave speed measurements [*Dziewonski and Anderson*, 1981]. At the lower confining pressures in the uppermost crust, the moduli at seismic frequencies could be several times higher than for seasonal or long-term loading, because of the presence of cracks if fluid pressure within cracks is not equilibrated [*Ravalec and Gueguen*, 1996; *Fjaer et al., 2008, chapter 5; Wauthier et al.*, 2012]. Poroelastic effects contrast between drained and undrained response. Plastic deformation in unconsolidated terrains could also affect the effective elastic moduli.

Knowledge about upper crustal elasticity parameters is important for many applications, including the estimating the magnitude of imparted stress by an earthquake on nearby faults [*King et al.,* 1994], inferring earthquake slip distributions and stress drop from surface displacement observations [e.g. *Simons et al.,* 2002; *Sun et al.*, 2011], inferring the overpressure in volcanic magma reservoirs [e.g. *Fukushima and Cayol*, 2005; *Grosfils et al.*, 2013], and

inferring pressure changes related to fluid extraction and injection [e.g. *Vasco et al.*, 2010, *Yang et al.*, 2015]. Furthermore, it allows to isolate the displacement component in response to surface loading and to interpret the remainder in terms of secular and transient tectonic [*Chamoli et al.,* 2013; *Amos et al.,* 2014] and/or volcanic processes [*Grapenthin et al.*, 2010; *Heap et al.*, 2014; *Odbert et al.*, 2015]. Lateral variations in elastic moduli have been invoked to explain asymmetric strain patterns due to earthquake loading *[Peltzer et al.,* 1999].

Previous geodynamic studies in Tibet used upper crustal elastic parameters inferred from seismic wave speeds in the range of (or equivalent to) 80 to 130 GPa for Young's modulus [*Peltzer et al.*, 1999; *Ryder et al.*, 2007; *Tao et al.*, 2008; *Wang et al.*, 2013], neglecting that the static moduli in the uppermost crust may be lower than the dynamic, seismic moduli. In this study we probe the Young's modulus of the Tibetan crust using InSAR observations of crustal response to lake loading. The lakes on the Tibetan plateau are changing in volume because of the changing climate [*Jiao et al.*, 2013; *Shen et al.*, 2014]. Most lakes are growing because of increased glacier melting in response to atmospheric warming and increased precipitation, but some lakes are receding. The fastest retreating lake is Yangzhuoyong Lake [*Zhang et al.*, 2011, 2013].

5.2. Background

Yangzhuoyong Lake, also referred to as Yamzho Yumco, is one of the holy lakes of Tibet, located ~100 km south of Lhasa. It is an endorheic lake [*Zhang et al.*, 2011] with a surface area of ~643 km^2 (east-west 130 km, north-south 70 km) and an average water depth of 30-40 m (maximum depth of 59 m). The lake is draining a ~6100 km^2 basin [*Chu et al.*, 2012a] at an average elevation of 4440 m. North of the lake the topography varies from 3500 m in the valleys to 5000 m in the mountain peaks. South of the lake the topography reaches up to 7000 m (Figure 1a). The major tectonic structures in the area are the Yadong-Gulu rift and the Yalu Zangbu fault zone [*Sun et al.*, 2011] northwest and north of the lake, respectively. The crustal thickness is about 70 km close to the Yalu Zangbu river, and gradually decreases to 40 km to the south [*Institute of Geology and Geophysics*, 1981]. A 2008 Mw 6.3 normal faulting earthquake indicates extension across the Yadong-Gulu rift [*Sun et al.*, 2011].

Optical remote sensing shows that Yangzhuoyong Lake retreated by ~80 km^2 between 1970 and 2010 [*Li et al.*, 2014]. A lake level gauge [*Chu et al.*, 2012a] at Baidi (Figure 1a) recorded a water level decline of about 5 m since 1970 [See Figure S1 in the supporting information], of which 3 m occurred during the 2003-2010 observation period of this study (gray line in Fig. 2a). The low stands of the lake occur between May and July and the high stands between September and November of each year [*Chu et al.*, 2012b]. Satellite laser altimetry data also show a drop in lake level [*Zhang et al.*, 2011]. The lake level decline appears to correlate with increases in air temperature and potential

evaporation, suggesting that these are the drivers for lake retreat [*Liao et al.*, 2012].

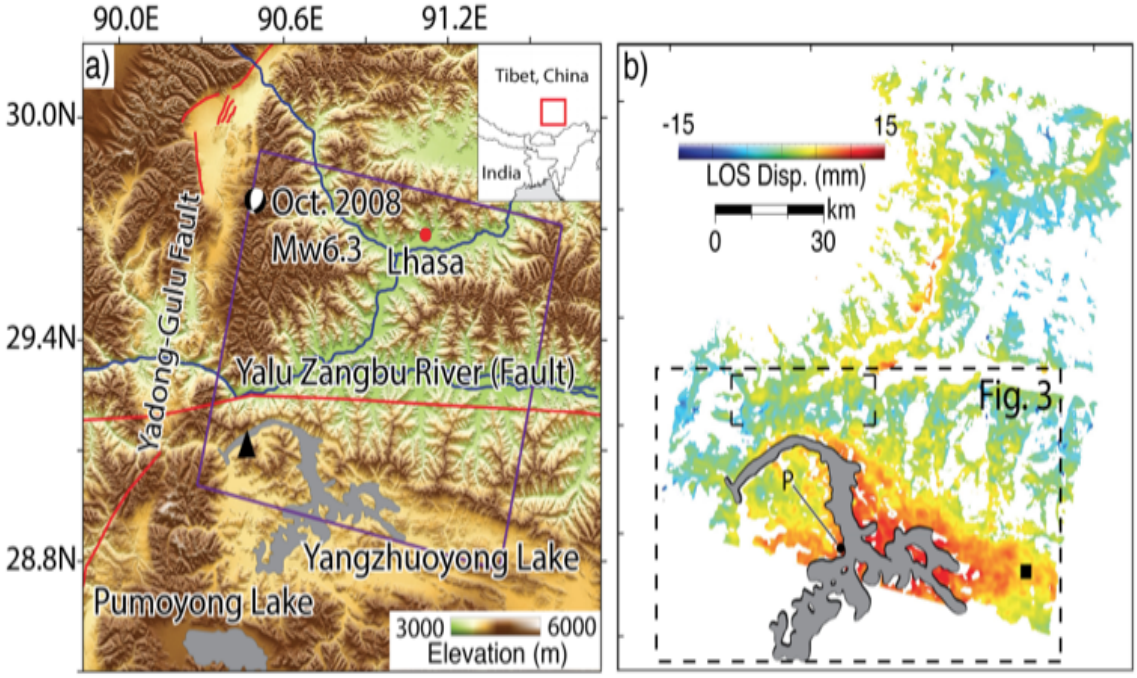

Figure 5.1. *a) Topographic relief of the study area around Yangzhuoyong Lake. Black triangle: Baidi water level gauge; purple rectangle: SAR coverage (track 405, frame 3015); grey shadings: lakes. b) 2003-2010 InSAR LOS displacement map. Solid square: reference point; dashed rectangle: area of figure 3; small rectangle north of lake: area for the estimation of uncertainty of the time-series.*

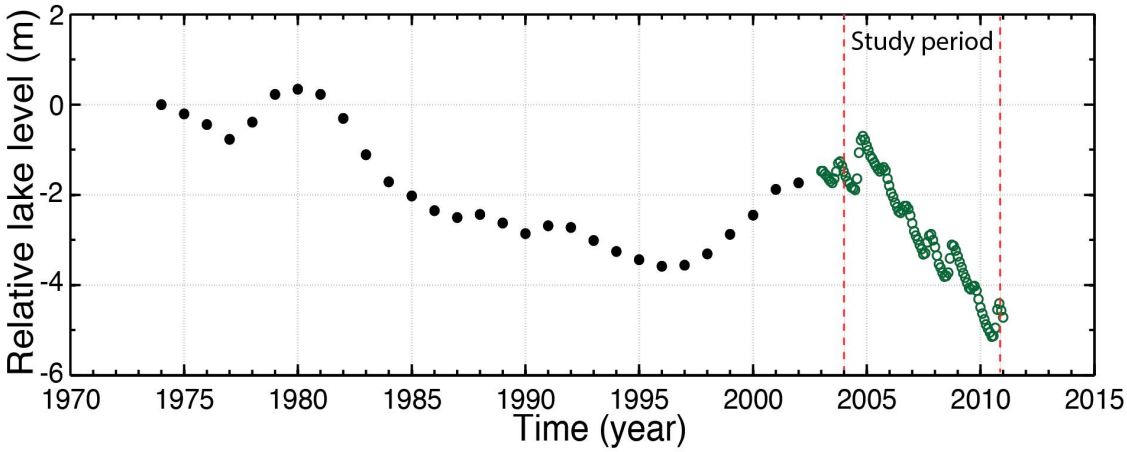

Figure 5.2. *Lake level variation at Yangzhuoyong Lake (1974-2010) [Chu et al., 2012b]. Black circles: annual average. Green circles: monthly average. Red dashed lines indicate the study period.*

5.3. InSAR analysis

Our analysis is based on 27 Envisat ASAR images acquired between December 2003 and September 2010. We discard one SAR acquisition (Nov. 02, 2004) because of strong atmospheric delays. Using spatial and temporal baseline thresholds of 450 m and 4 years, respectively, we are left with a network of 92 interferograms connecting 20 acquisitions (see Figure S2 in the supporting information). We don't include the frame to the south in the analysis because four summer acquisitions are missing.

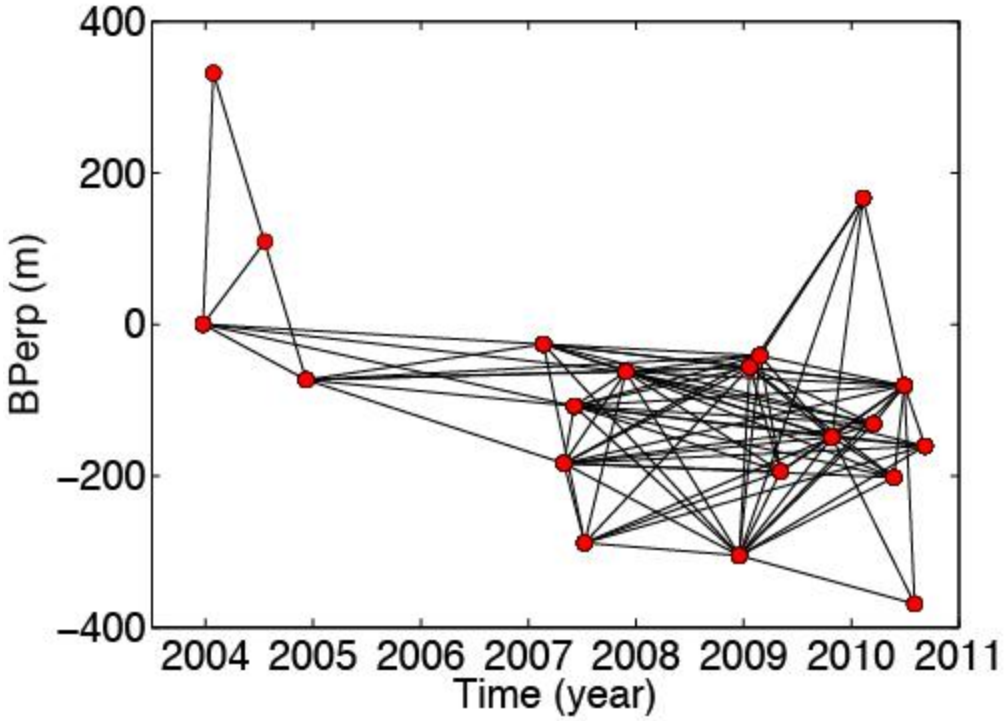

Figure 5.3. *Baseline-time plot of the network of SAR acquisitions (red dots) and interferograms (black lines) used for the time-series inversion.*

For data processing we use an approach based on the ROI_PAC software adapted for regions with strong topographic relief [*Doin et al., 2011*, *Grandin et al.*, 2012]. The imagery is coregistered using orbital information and offset fields. The topographic phase is removed using a 3 arc-second SRTM digital elevation model, interpolated to 1 arc-second spacing and then take 2 looks in range and 10 looks in azimuth direction to obtain ~40×40 m^2 ground pixel. Next we remove contributions from topography-correlated tropospheric delays and localized DEM errors from the wrapped interferograms to aid phase-unwrapping. The first are estimated using a second-order polynomial with respect to elevation [*Cavalie et al.*, 2007; *Nof et al.*, 2012, see Figure S3a,b in the supporting information for an

example]; the second are estimated from a set of interferograms using the method of *Ducret et al.* [2014] (see Figure S3c,d in the supporting information]. For this processing step we use all available SAR acquisitions, including interferograms with baselines larger than 450 m. Next, we take additional looks to obtain ~80×80 m^2 pixels, apply an adaptive filter, and unwrap the phase using the approach of *Chen and Zebker* [2000]. We retain only pixels with a spatial coherence larger than 0.2 in 60 percent of the interferograms [e.g. *Baker and Amelung*, 2012]. We reduce phase unwrapping errors of isolated areas using the nearest-neighbor interpolation method of *Agram et al.* [2009]. We then add the tropospheric phase contributions back to the unwrapped phase. This approach of temporarily removing topography-correlated phase contributions, combined with the localized DEM correction, improves the phase unwrapping because it reduces the spatial standard deviation of the wrapped phase, ensuring that multi-looking and filtering increases the SNR without blurring the signal.

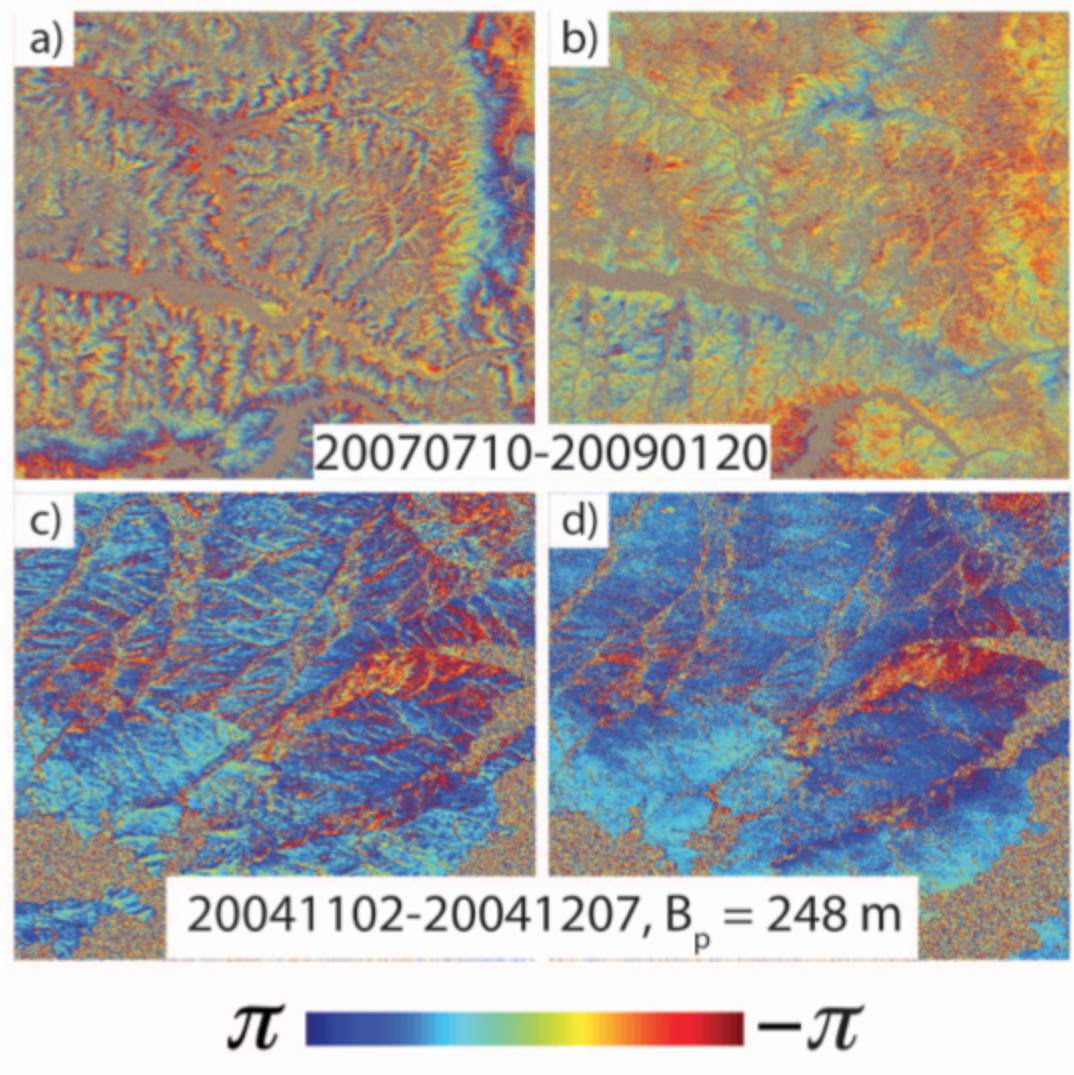

Figure 5.4. *APS and DEM corrections on wrapped phase. a) and b) Interferograms before and after APS correction. c) and d) interferograms before and after DEM correction.*

We then use the small baselines (SB) InSAR time-series approach to obtain pixelwise displacement histories [*Berardino et al.*, 2002]. Finally, in the time domain we remove the topography-correlated phase due to tropospheric

layering from the unwrapped phase using a second-order polynomial, and correct for topographic residuals using the approach of *Fattahi and Amelung* [2013].

5.4. Results

The ground displacement field in radar line-of-sight (LOS) direction shows a bulge of up to 10 mm LOS displacement near the lake (red colors, Figure 1b), corresponding to ~11 mm of uplift assuming that displacement is vertical (with a radar incidence angle on the ground of ~23^o Envisat's I2 beam is most sensitive to vertical deformation). To the north of the lake where the topographic relief is up to 2500 m, LOS variations likely represents residual tropospheric delays.

A displacement time series for a point near the lake center (Figure 2a) shows the correlation between ground displacement and lake level (grey line) (Figure 2a). Seasonal drops in lake level (negative lake level changes) coincide with LOS decreases (uplift) and seasonal rises in lake level (positive lake level changes) coincide with LOS increases (subsidence). The correlation between the sign-reversed lake level and displacement is 0.9.

The LOS displacement u^j_i, at pixel j and epoch i, relates to the lake level, l_i, by $u^j_i = d^j * l_i$ with d^j the LOS displacement with respect to unit lake level change or unit response of the system at pixel j [in mm/m or 10^{-3}]. Both u^j_i and l_i are relative to the first SAR acquisition. The least squares solution for d^j is given by

$$\begin{bmatrix} d^j & c^j \end{bmatrix} = \left(G^T G\right)^{-1} G^T \mathbf{u}^j \quad (1)$$

with $\mathbf{u}^j = (u^j_1, u^j_2, \ldots, u^j_N)^T$, c^j the constant for least square fitting, and G = [(l_1, l_2, …, l_N)^T, (1, 1, …, 1)^T]. An example for d^j at point P is given in Figure 2b.

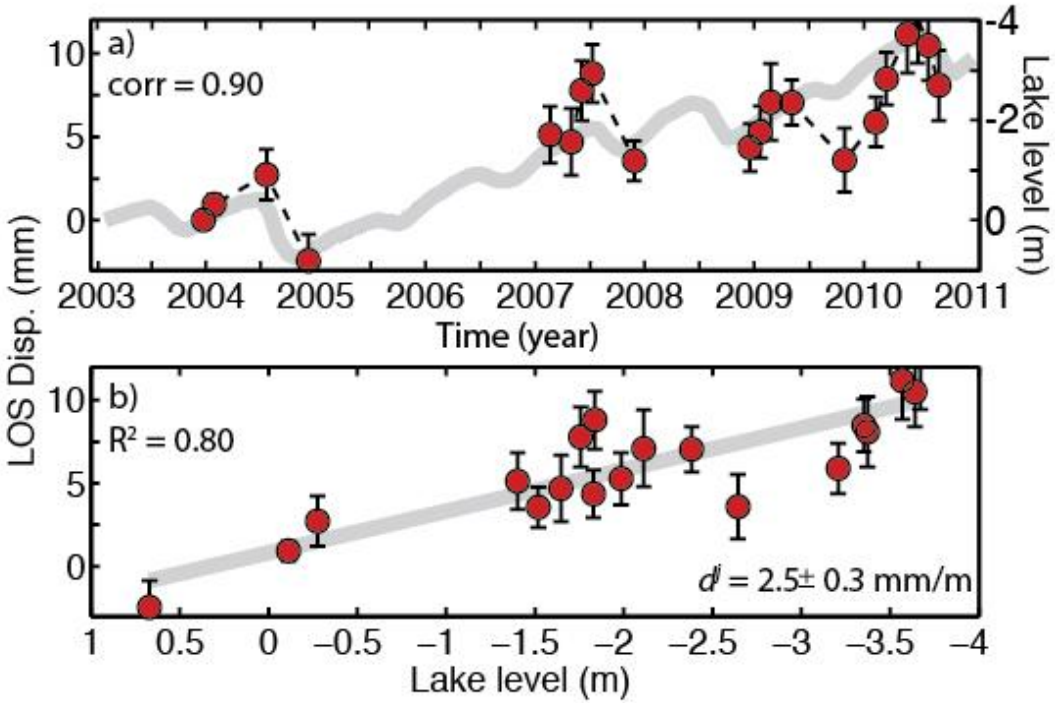

Figure 5.5. *a) LOS displacement time-series relative to the first acquisition for point P (red dots) together with the monthly lake level at the Baidi gauge relative to December 2003, the month of the first SAR acquisition (grey line, negative numbers correspond to lake level decrease). Error bars: standard deviation of LOS displacement at each epoch for the non-deforming area northwest of the lake (rectangle in Figure 1). b) LOS displacement as a function of lake level change (red dots). The slope (grey line) is the LOS displacement with respect to unit lake level change (d^j, unit mm/m).*

5.5. Modeling

We use homogeneous [*Farrell*, 1972; *Graphenthin et al*, 2006] and layered elastic half-space models [*Cavalie et al., 2007*] to simulate the observed rebound and estimate Young's modulus. In the layered model, seismic derived parameters do not fully explain our observation (parameters see Figure S5b,d and model see Table S1 in the supporting information) we estimate the modulus of the top layer and use at depth larger than 15 km moduli inferred from the seismic P-wave speed measurements of the area from *Yin et al.* [1990] and *Vp/Vs* ratio and density from an area further north from *Mechie et al.* [2004] [Figure 4]. Dominantly vertical displacements in response to surface loading can't resolve Poisson's ratio because of the trade-off with Young's modulus, as shown by the formulations of the Green's functions [e.g. *Grapenthin et al.*, 2006; *Zhao et al.*, 2014].

Depth (km)	*Vp* (km/s)	*Vs* (km/s)	Density (kg/m^3)	Young's modulus (GPa)	Poisson's ratio
5	5.2	3.1	2400	56*	0.22
15	5.7	3.36	2550	71*	0.23
35	6.1	3.6	2700	86	0.23
65	6.65	3.73	3000	106	0.27
half-space	7.8	4.4	3300	162	0.27

Table 5.1. *Earth model from seismic data. Vp is from [Yin et al., 1990] covering Yangzhuoyong Lake, Vs and density are from [Mechie et al., 2004] based on INDEPTH III [Zhao et al., 2001] covering Siling Lake (~300 km north of Yangzhuoyong Lake). Young's modulus and Poisson's ratio are calculated from*

*columns 2-4. * first 2 layers are combined in inversion, assuming Poisson's ratio of 0.25 and density of 2700 kg/m^3.* ADD EQUATIONS FOR PARAMETERS CONVERSION

The data is the LOS displacement with respect to unit lake level change (unit mm/m, see Fig. 2b), calculated for each pixel from the LOS displacement history (Figure 3a). We use a quadtree decomposition [*Jonsson et al.*, 2002] to downsample the data with quadrants selected according to the expected signal (using the layered model with Young's modulus of 40 GPa, quadrant size 1.44 km to 11.52 km, threshold for subdividing of 0.08 mm/m, 315 data blocks; half and doubled Young's modulus give nearly identical sampling). We found that this sampling provided reasonable sensitivity to model variations in both the near and far fields. To find the best-fitting models we minimize the root mean square error (RMSE), defined as:

$$RMSE = \sqrt{\left(\mathbf{d}-\mathbf{p}\right)^T \Sigma^{-1} \left(\mathbf{d}-\mathbf{p}\right) / M} \quad (3)$$

where **d** is the observed and **p** the modeled LOS displacement per unit lake level change. **d** and **p** are M*1 vectors with M is the number of data blocks after quad-tree decomposition, and Σ is the M*M variance-covariance matrix used as a weighting matrix, calculated from the sample semi-variogram and covariogram [*Sudhaus and Jonsson*, 2009] (see Figure S4 in the supporting information for the data weights).

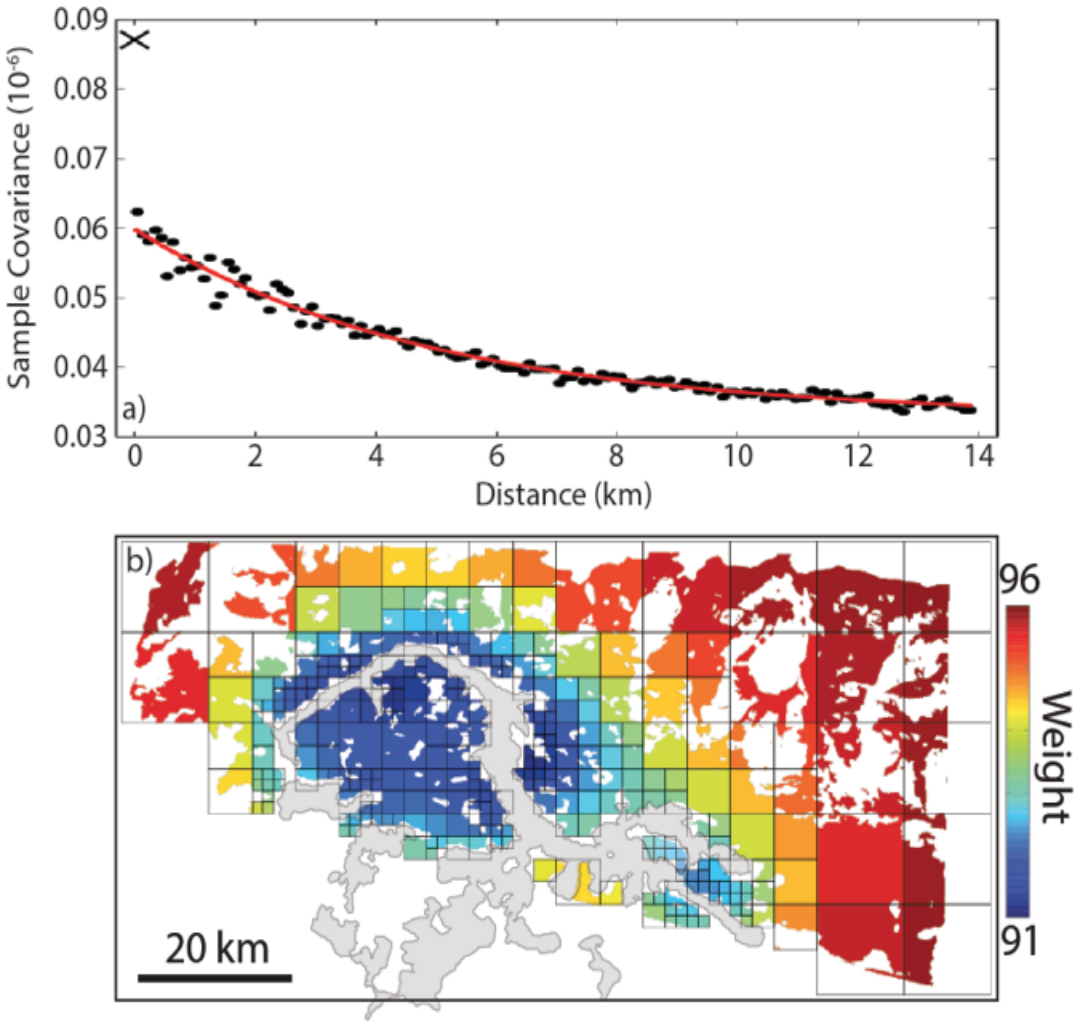

Figure 5.6. *a) Variance (cross at zero distance), sample covariance (dots), and fitted covariance function (red line). b) Variance-covariance weights [Sudhaus and Jonsson, 2009] calculated from a)*. The weight is dimensionless because the unit of our data is mm/m.

For the layered model we conduct a grid search varying Young's modulus of the top layer between 30 GPa to 150 GPa with a step size of 5 GPa. The best fit is found for a modulus of 50±9 GPa for the top layer (Figure 3). For the half-space model we find a Young's modulus of 81±12 GPa using linear inversion

(see Figure S5a in the supporting information). The RMSEs for both models are 0.77 mm/m and 0.79 mm/m, respectively. We obtained the standard error for the layered model from 1000 bootstrap samplings [*Hastie et al.*, 2009], and for the half-space model from linear error propagation of the uncertainty. The model predictions agree with the observations west and south of the lake but are lower than observed northeast of the lake. A west-east profile crossing the lake (AA' in Fig. 4) shows that the layered model is characterized by higher displacement gradients then the half-space model because of the lower Young's modulus in the top layer.

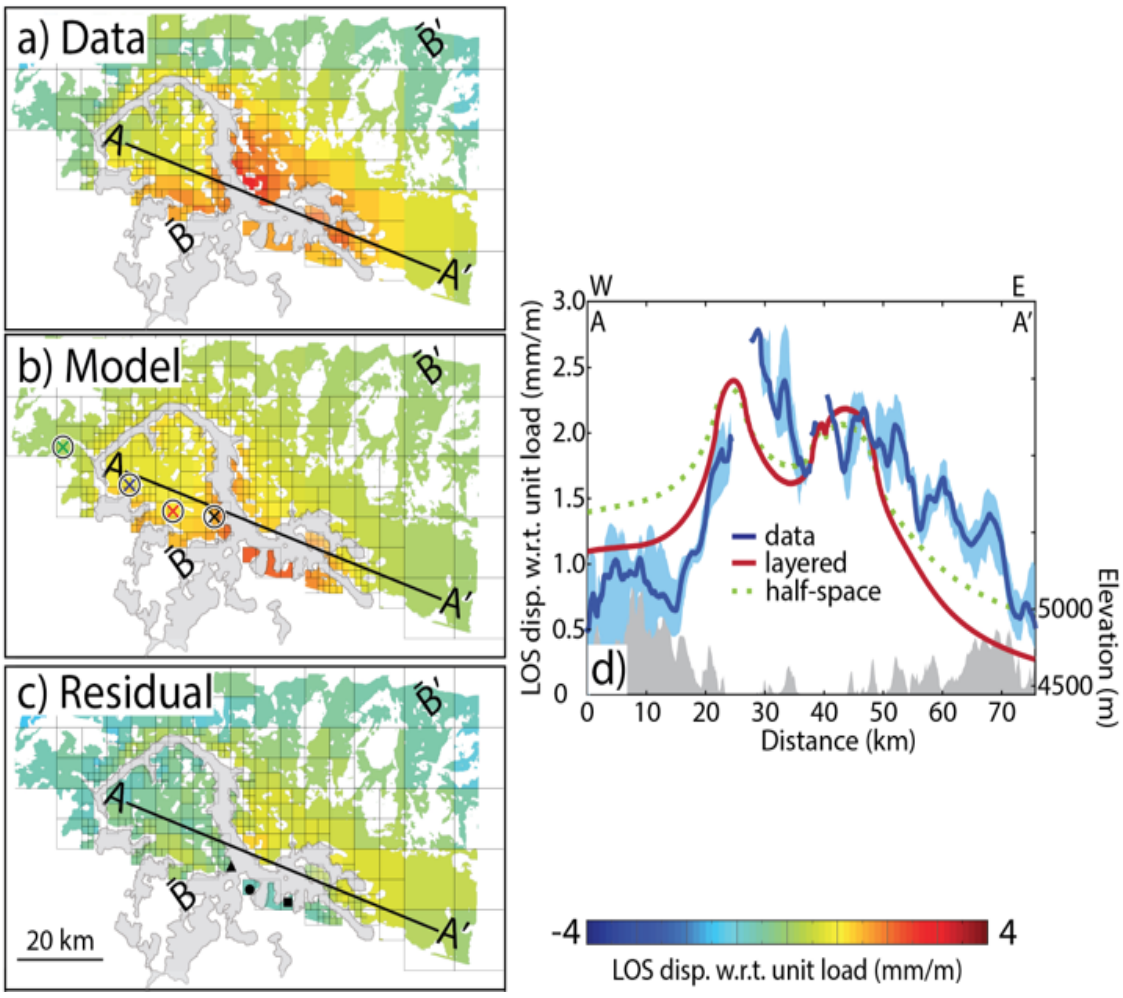

Figure 5.7. *a) Observed LOS displacement with respect to unit load, b) prediction from the best-fitting layered model (top layer Young's modulus of 50 GPa), c) differences between observations and model predictions, d) profile along AA' averaged over a width of 1.8 km (dark blue; light blue shows the upper and lower bounds) together with the predictions of the best-fitting layered and homogeneous model. Gray shading: topographic elevation along the profile. For profile BB' see Figure S6 in the supporting information. The colored crosses in b) show the points of Fig. 4. The triangle, circle and square in c) denote the geometric mass center of the load at current lake level and for 100 and 200 m higher lake level, respectively.*

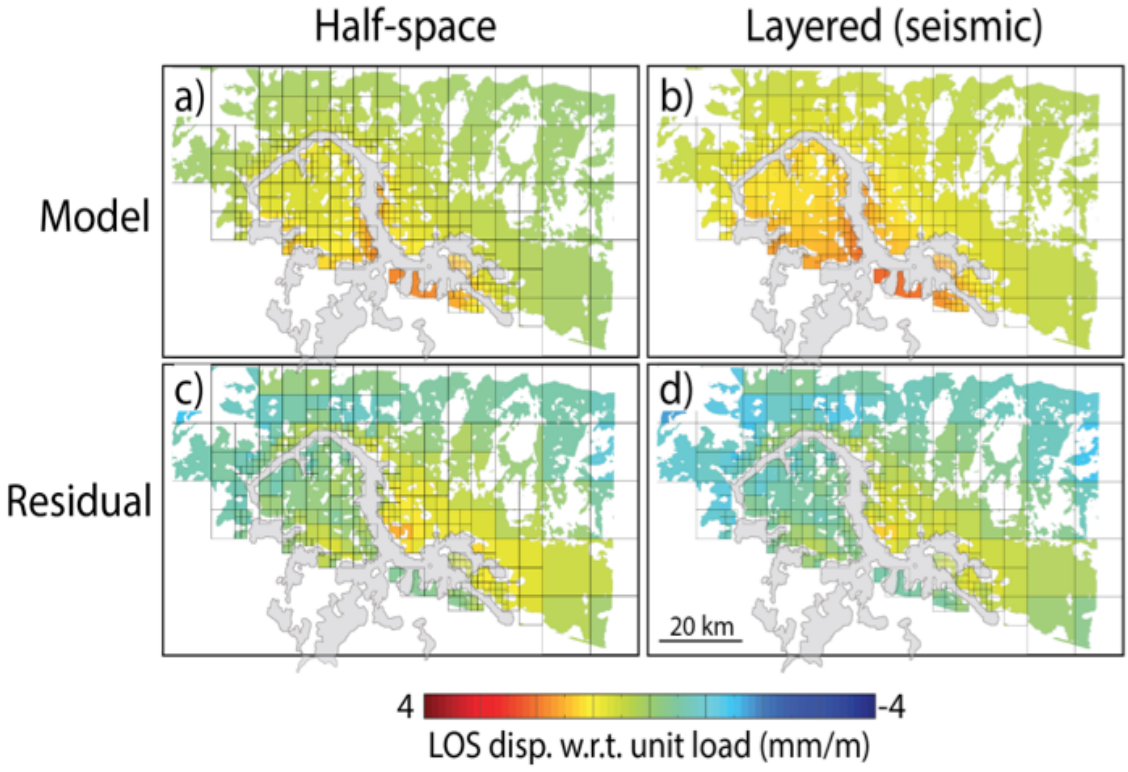

Figure 5.8. *a), b) Same as Figure 3b but for the best-fitting half-space model (Young's modulus of 81 GPa) and for the layered model using the seismic*

Young's moduli. c,d) Differences between data and model predictions. The RMSE of the half-space model is 0.79 mm/m and 1.03 mm/m for the seismic layered model.

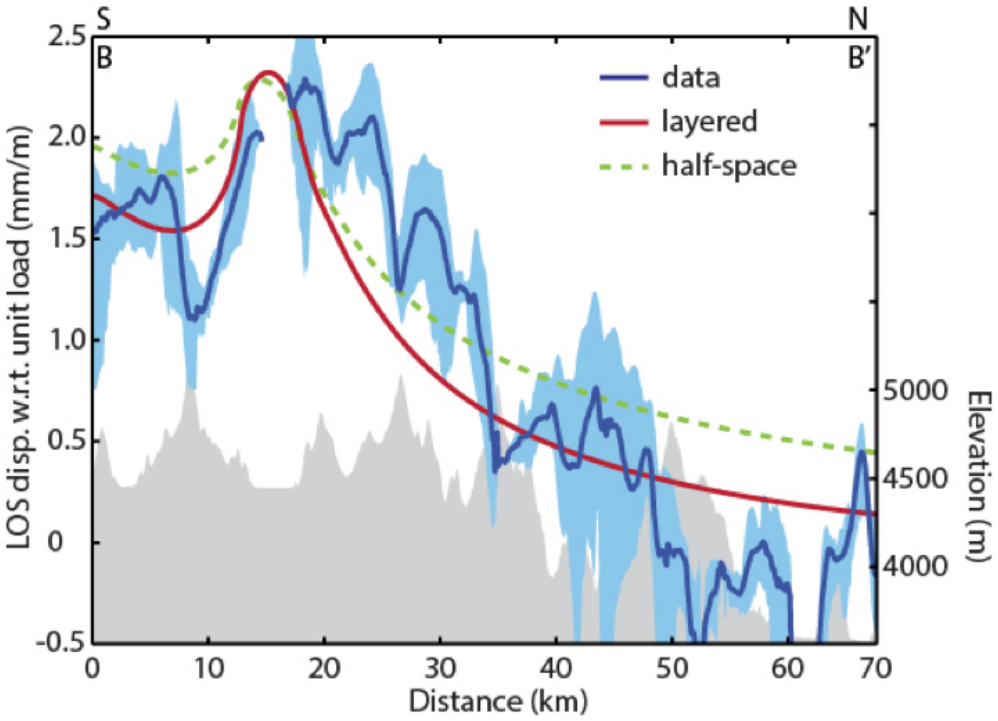

Figure 5.9. *Same as Figure 4 but for profile BB'.*

5.6. Discussion

InSAR recorded up to ~10 mm ground displacement towards the radar in the vicinity of Yangzhuoyong Lake during 2003-2010. The lake level dropped by more than 3 m during this time period, suggesting that we see rebound caused by the partial removal of the water load. The results were obtained using a data analysis approach that included the empirical estimation and removal of the topography-correlated phase assuming the phase was caused by atmospheric

delays. Using cloud free SAR acquisitions and the MEdium Resolution Imaging Spectrometer (MERIS) estimates for the atmospheric delays and using the ERA-Interim global atmospheric model for atmospheric corrections [*Jolivet et al.*, 2014], the obtained LOS displacement fields are more noisy but do show a signal in the vicinity of the lake (see Figure S7 in the supporting information), making us confident that this signal represents real deformation and is not a processing artifact. For comparison with other loading problems it is useful to express ground displacement in response to mass change [*Bevis et al.*, 2004]. Given the surface area of the lake (621 km^2), 1.61 m of lake level change corresponds to a mass change of 1 Gt. The response next to the lake center (point P, 2.5 mm/m) thus corresponds to 4.0 mm/Gt of load change.

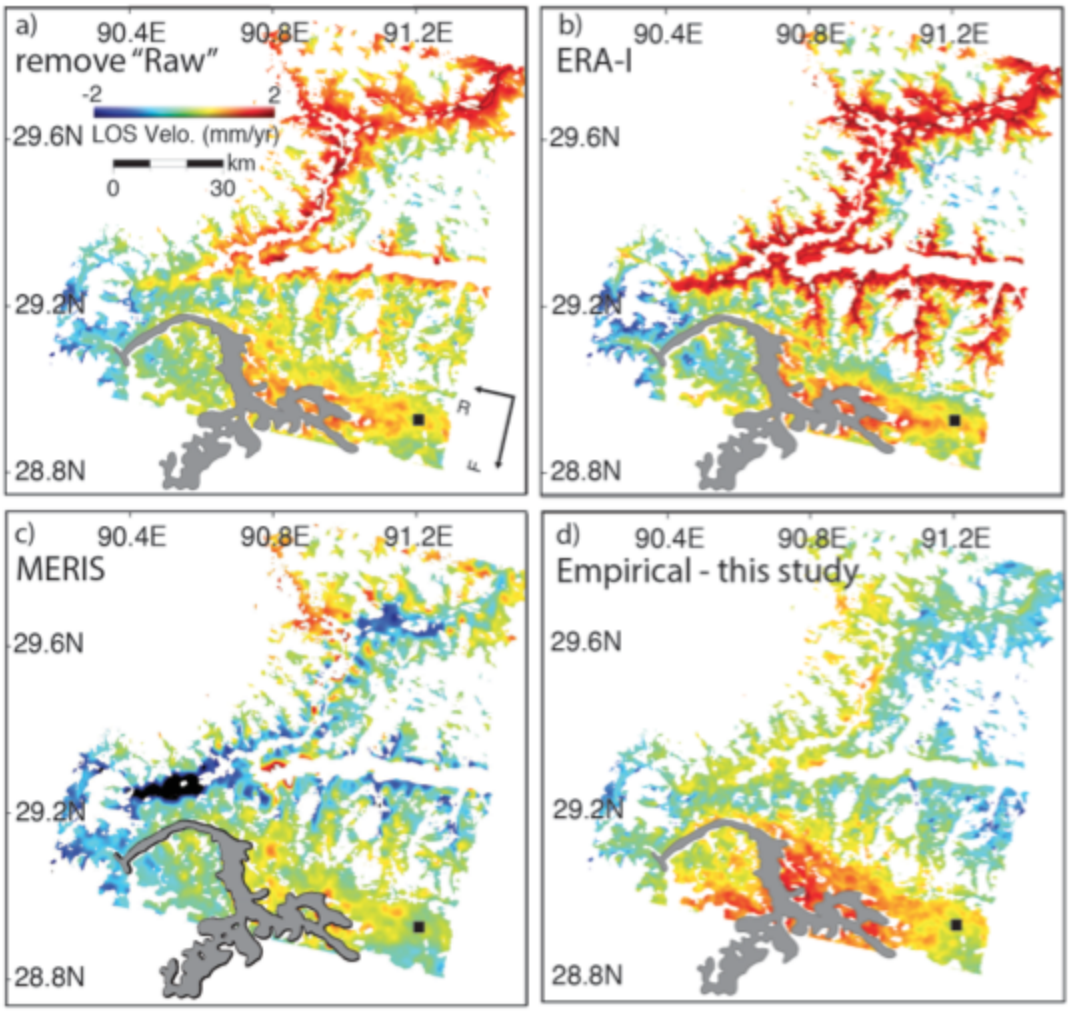

Figure 5.10. *Averaged InSAR LOS velocities obtained using different atmospheric delay correction approaches. a) Original velocity without atmospheric delay correction. b) Correction using the ERA-Interim global atmospheric model (using the same SAR acquisitions as in Figure 1b). c) Correction using cloud free scenes and MERIS. d) Empirical estimation and removal of the topography-correlated phase.*

The Young's modulus in the top layer of our preferred model is 50±9 GPa. This is significantly smaller than the value inferred from the regional seismic

model of 68-78 GPa (FIg. 4b). The seismic Young's modulus falls outside the 2-sigma (98%) confidence interval of the inferred modulus, reinforcing that the modulus controlling the response to surface loading is smaller than the modulus at seismic wave frequencies.

To determine the feasibility of the top layer thickness, we conduct a sensitivity test on different depth of crust. A remaining question is which depth range of the crust is sampled by changes of the Yangzhuoyong Lake load. To address this question we conduct a depth sensitivity test following Doin et al. [2015]. We divide the crust into a series of 5 km thick sub-layers. Starting from the preferred model we reduce the Young's modulus in each sub-layer by a factor of 2 and compare the vertical surface displacement with that from the preferred model as a function of distance from the load's gravity center. Figure 4c shows that the reduction in the elasticity parameters in the 5-10 km and 10-15 km sublayers causes the largest increases in surface displacement (0.1-0.3 mm/m at 6-24 km distance with the largest increase of more than 0.3 mm/m at 6 km distance). Changes in the elasticity parameters in the sublayers below 40 km depth have little effect (< 0.07 mm/m). This shows that in most parts of the study area the surface response is most sensitive to the 5-15 km depth range, confirming our approach of varying the elasticity parameter of the top 15 km layer.

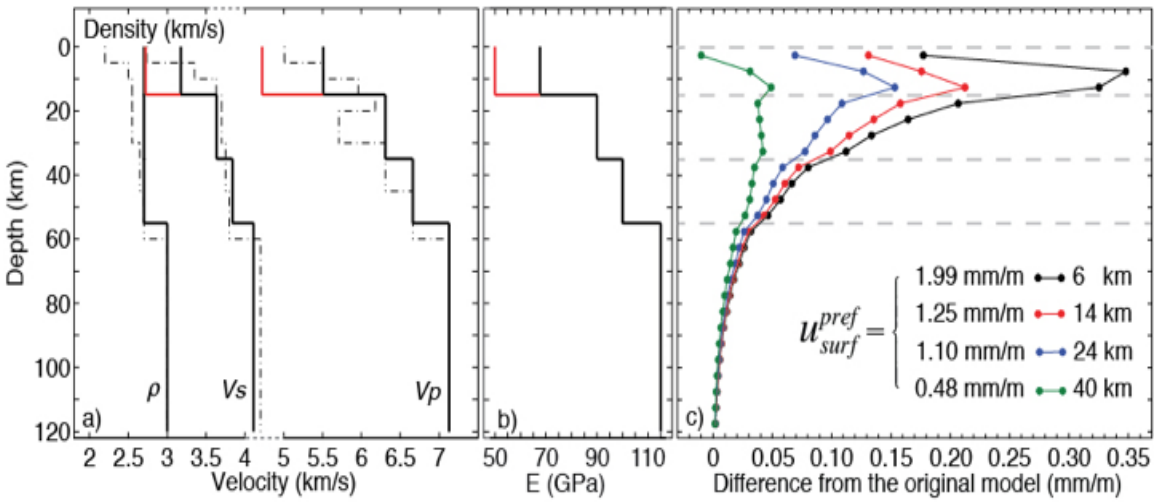

Figure 5.11. *a) Vp* [*Yin et al.*, 1990]*, Vs and density* [*Mechie et al.*, 2004] *as a function of depth (dashed lines) together with layer averages (solid lines) and b) corresponding Young's moduli. Red lines indicate parameters of best-fitting model. The parameters of the layered model are summarized in table S1 in the supplementary material. c) Depth sensitivity test showing the difference in surface response from the original model (according to Doin et al. [2015]). Each dot represents the center of a sub-layer. Four colored line represent four points (crosses on Figure 3b) from the lake center to far field, defined by the distance from the current lake mass center (black triangle in Figure 3c). u_surf means the LOS displacement at each point in the preferred model.*

The response to surface loading can also be explained using a uniform half-space model with an effective Young's modulus describing the averaged response of the sampled rock [*ref*]. Using this model we find a Young's modulus of 81+-12 GPa. This value is between the effective Young's modulus of ~40 GPa for the smaller-sized Dead Sea and Icelandic ice cap loads [*Grapenthin et al.*,

2007; *Nof et al.*, 2012; *Auriac et al.*, 2014] and the 130-140 GPa for the larger-sized Amazon river [*Bevis et al.*, 2005] and Bangladesh monsoon flooding loads [*Steckler et al.* [2010]. *Chanard et al*. [2014] use a layered, spherical model to find a Young's modulus between 90 and 170 GPa for the Himalaya region. These differences reflect that larger loads sample deeper regions of the Earth's mantle characterized by higher Young's moduli.

Our best-fitting models underpredict the displacement response in the area northeast of the lake by 0.5-1 mm/m. One explanation is that this area is also rebounding because of a possible visco-elastic response from past unloading. The lake level history over the past few hundred years is not known. Given the topographic relief, for a 100 and 200 m higher lake level the lake's past center of gravity would be located 12-20 km to the east of the current center of gravity (Figure 3c). Another possible explanation is that the upper crust in this area is weaker and a lower Young's modulus results in localized but more rebound than further west. Seismic reflection studies identified relatively low shallow wave speed velocities (5.2 km/s) [*Yin et al.*, 1990] and partial melt in the middle crust (at 25 km depth) [*Brown et al.*, 1996; *Gu et al.*, 2000] but can't resolve the three-dimensional structure .

5.7. Conclusions

We have documented a total of 10 mm of ground surface displacement towards the satellite in the vicinity of Yangzhuoyong Lake between 2003 and 2010. We attribute this signal to crustal rebound due to lake retreat. The lake

level dropped ~3 m during this time period. Most of the signal can be explained as the elastic response to load changes of a layered half space with a Young's modulus of 55+-9 GPa in the top layer (thickness of 15 km), except an area of 0.5-1 mm/m LOS displacement per unit lake level change northeast of the lake. We attribute this residual signal to lateral heterogeneities in Young's modulus, possibly related to partial melting, and/or a delayed response to past load changes but we can't distinguish between these two possibilities.

Chapter 6

Ground deformation due to carbon sequestration detected using TerraSAR-X: A case study in Texas, United States

Summary

Retrieving surface geomechanical responses due to CCS injection from InSAR is one of the most economical methods for reservoir simulations. In this study, we use TerraSAR-X high resolution spot light InSAR data to monitor an active CCS site at Hastings, Texas, between January 2012 and April 2014, at a temporal frequency of ~11 days. 54 SLC and 171 small baseline interferograms are used for the time-series analysis. A SBAS technique is developed with modified network building, point selection, absolute phase retrieving and time-series inversion functions. Based on this technique, we obtain the time-series at ~100 m spatial and sub-month temporal resolutions. We optimize the solution through ridge regression, which regularizes model variance to reduce overfitting. For those points with long-term velocities smaller than 1 mm/yr, InSAR can hardly

provide the temporal details. The velocities imply that there is no significant surface deformation at the center of the injection zone from InSAR, after January 2012 when production started. Large-scale background deformation likely exists according to the comparison between InSAR and GPS measurements. We find four anomalies with several millimeters LOS deformation at the surrounding areas. These areas are likely affected by the local salt water pumping. To verify these signals, more ground information is required.

6.1. Overview

Synthetic Aperture Radar Interferometry (InSAR) has been proved to be useful for monitoring surface deformation associated with geological carbon sequestration (CCS) [*Vasco et al.*, 2008]. A series of reservoir simulations based on the first success of InSAR in In Salah, Algeria were built [*Vasco et al., 2010*; *Rutqvist et al.*, 2010; *Rucci et al.*, 2010; *Tamburini et al.*, 2010*; Bissell et al.*, 2011; *Shi et al.*, 2012; *Rinaldi and Rutqvist*, 2013]. The CCS induced surface deformation is usually at a magnitude of several millimeters, requiring high stability of the interferometric phase. *Zhao et al.* [2011] concluded on the advantages of low frequency data in rural or vegetated areas because of its ability of keeping coherence. New techniques have also been developed for the stable point selection [*Hooper et al.*, 2007; *Ferretti et al.*, 2011]. *Rohmer and Raucoules* [2012] further discussed the detectability of long-term CCS injection by InSAR.

In this study, we use TerraSAR-X (TSX) high resolution spot light data. The temporal sampling density of TSX data increases to three times of the ERS/Envisat data, and four times of the Alos data, which is 11 days providing a “microscope” in time. An extra advantage of this data is its ultra high spatial resolution – ~0.9 m, which can potentially enhance the performance of the InSAR technique (more details discussed in section 4).

We develop a modified small baseline InSAR (SBAS) technique to monitor the surface deformation in response to geological carbon sequestration. A 2.5-year monitoring at the Hastings oil field, Texas is discussed. In the major injection area, InSAR does not find significant deformation, which is also inferred by GPS measurements. Small deformation possibly caused by local water pumping is detected close to the injection site.

6.2. Study area

The Hastings oil field is located in Brazoria and Galveston Counties, Texas, ~30 km south-east of Houston, discovered in 1935. It ranks as one of the largest oil fields in the Texas Gulf Coast. The development of the field was completed by 1941, with the areal extent of ~23 km^2, which is divided into two sections – Hastings West and Hastings East – by the major fault. The production is from the Frio formation at depths of ~1700 m, with salt water disposed at the same time to maintain the reservoir pressure [*McWilliams*, 1972]. The injection of CO_2 started in December 2010 in northern part of Hastings West, and until October 2011, ~28 billion cubic feet (BCF) CO_2 has been injected into the Frio

formation. Average reservoir pressure was increased during the injection from 2350 pounds per square inch (psi) to 2850 psi. After the significant production since mid-January 2012, the pressure dropped for ~100 - 150 psi, and then was maintained at a stable level.

6.3. Data

We use a 3 m Lidar DEM (Figure 1) from the national elevation dataset [*Heidemann*, 2012, *URL: http://ned.usgs.gov/faq.html*] to remove the topographic phase during the interferometry processing. The DEM is interpolated to 1 m using a cubic spline method in order to simulate full resolution DEM in SAR coordinates. The study area lacks topographic relief, with elevation ranging from 0 m to 22 m with 90% of the area between 7 m to 15 m. The coherence map is calculated at full resolution as well.

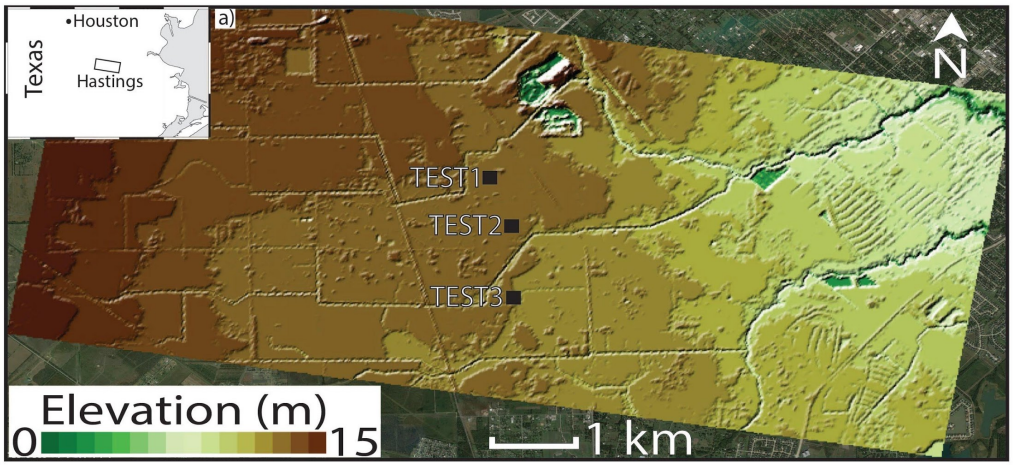

Figure 6.1. *Shaded relief digital elevation map of Hastings. The small box at the upper-left corner indicates the location of the study area and the SAR data coverage (black frame). The Hastings formation is ~20 km to the south of the*

Houston city, Texas. TEST1, 2, 3 indicate the location of three continuous GPS stations.

We acquired TSX high resolution spot light data starting from January 27, 2012 until April 20, 2014, nearly every 11 days. Two data gaps (55 days for each) occur in the summers of 2012 and 2013, which influence the continuity of the InSAR time-series, because coherence decreases faster in the summer due to denser vegetation, so that the phases of long temporal baseline interferograms are unstable in these periods. The ground coverage is about 12 km and 6 km in SAR range and azimuth directions. We combine a total 54 single look complex images (SLC) to 171 interferograms (Figure 2). We generate interferograms using hierarchical temporal and perpendicular baseline thresholds: 1) B_{temp} < 22 days and B_{perp} < 150 m; 2) B_{temp} < 33 days and B_{perp} < 120 days 3) B_{temp} < 44 days and B_{perp} < 80 m; 4) B_{temp} < 55 days and B_{perp} < 40 m; 5) B_{temp} < 66 days and B_{perp} < 20m. Because the deformation due to injection is usually very small, we assume there is no deformation during the two data gaps, with two simulated zero deformation interferograms connecting the network (dashed lines in Figure 2).

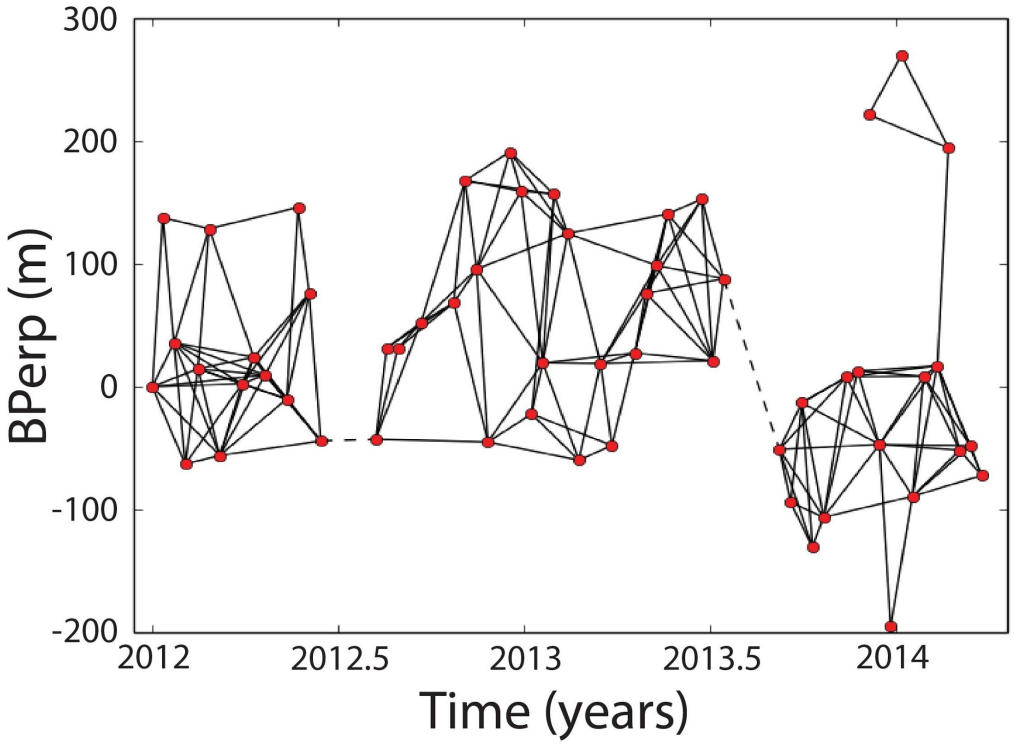

Figure 6.2. *Baseline plot as a function of time. Each solid line represents an interferogram generated by two SLCs (red points). Dashed line represents the simulated zero deformation interferogram during the two data gaps. The hierarchical thresholds are described above. One exception is the interferogram between February 24, 2014 and March 18, 2014 with a long spatial baseline. Total number of SLC is 54 with 174 interferograms generated.*

6.4. Point selection

In rural areas, the interferometric phase center is usually not stable through time, and there are much less persistent scatterers (PS) than in urban and rocky areas. After including more distributed scatterers as pseudo PS candidates (e.g. [*Hooper et al.*, 2007]), the spatial masking of the PS technique is usually similar to SBAS. We thus use the SBAS technique [*Berardino et al.*,

2002; *Zhao et al.*, 2014] using multi-looked, filtered interferograms for the time-series analysis.

To select stable points, we use a temporal analysis method based on the full resolution coherence map. For each pixel we calculate a coherence stability, *S,* defined as:

$$S = \sum_{i=1}^{N} C \Big/ N \tag{1}$$

With *C* the number of interferograms with coherence for this pixel above a given threshold ρ_{th}. N is the total number of interferograms. We use $\rho_{th} = 0.15$ and $S = 0.5$ for this study.

6.5. Interferogram denoising and absolute phase retrieving

Since the geomechanical responses associated with fluid injection and production vary smoothly in space, we reduce the noise level by applying 16 looks in both range and azimuth directions. The resulting spatial resolution is ~15 m in both directions.

The unwrapping process of InSAR usually fails and produces unexpected phase jumps at noisy phases. To avoid these uncertainties, techniques have been developed by *Zhang et al.* [2011] and *Tiampo et al.* [2013] to prevent path searches or network flow calculations. We follow the algorithm introduced by *Tiampo et al.* [2013] to retrieve absolute phases in this study. Considering the

noise in each interferogram as a 2-D random field following a Gaussian distribution [*Agram and Simons*, submitted], the zero-phase is at the mean. Assuming the phase due to deformation in each interferogram is between $-\pi$ and π (inferred from the small deformation rate and small temporal baselines selected), there are no phase jumps between neighboring pixels, except where the absolute phase difference is larger than π, comparing to the zero-phase. So pixels with phase jumps are corrected by adding or subtracting 2π respectively.

Several factors may affect the assumption above such as SAR satellite orbital uncertainty, the time delay when the radar signal travels trough the atmosphere and the spatial correlated deformation signal. Because of the high orbit accuracy of TSX data, we do not consider the orbital error correction. For interferograms with ramps visually (~2 % of the total interferograms), we de-ramp them with a bi-linear model estimated on the wrapped phase by the 2-D spatial derivatives. The ramps are mainly in range direction, indicating that the orbital error is dominated. The estimated ramps are added back after phase retrieving, based on the conclusion in *Fatahi and Amelung* [2014] that the limited orbital error in TSX data does not play a crucial role in InSAR time-series. We do not find ramps in azimuth direction, indicating that the few ramps we have are due to orbital errors and the stratified atmospheric delay is small (also implied from the small topographic relief). And the small deformation rate does not affect the choice of zero-phase significantly. The remaining uncertainty of this phase retrieving process is only the atmospheric delay caused by the local turbulence.

However, considering the relatively small area, this effect is also not crucial. For the pixel where atmospheric turbulence breaks the assumption of small phases, the temporal inconsistency will help us to eliminate that pixel based on the residual of time-series inversion.

A low pass filter is commonly applied before phase unwrapping. Because of the non-linearity of the wrapped phase, an adaptive filer is usually taken at this step to help unwrapping. Because we do not apply any phase unwrapping, and the phases become linear after the absolute phase retrieving, we simply apply a 10×10 Gaussian filter (~150 m on the ground) to further increase the signal to noise ratio.

6.6. Time-series inversion

A pixel-wise ordinary least-square (OLS) inversion is applied to generate the time-series first. The deformation evolutions at the monthly or weekly scales are not clear, because noises increase the degree of over fitting. We thus apply a ridge regression (RR) [*Hoerl*, 1962] to regularize the model, sacrificing part of model variance.

Regularizations have been applied to InSAR by *Lin et al.* [2010, principal component analysis] for the model complexity selection, by *Ozawa and Ueda* [2011, ridge like smoothing operator] for a low-pass constraint of the time-series analysis, and by *Samsonov and d' Oreye* [2012, RR] and *Zhao et al.* [2014, RR] to obtain multi-dimensional time-series. From a Bayesian point of view, RR is described as minimizing the cost function below [Chapter 1, *Bishop*, 2009]:

$$\sum_{n=1}^{N}(d-Gm)^2+\lambda m^T m \quad (2)$$

$$\lambda=\frac{\alpha}{\beta} \quad (3)$$

where *d* is the observation (interferometric phase), *m* is the model (deformation velocity), *G* is the design matrix, λ is the hyperparameter, α is the maximum likelihood model variance (from OLS), β is the variance of a prior model.

The solution of RR is given by:

$$m_{RR}=\left(G^T G+\lambda I\right)^{-1} G^T d \quad (4)$$

where m_{RR} is the model based on RR, *I* is an identical diagonal matrix.

One of the key processes of RR is to choose a proper hyperparameter λ to constrain the maximum likelihood estimation from a biased data sampling. RR is a biased estimator and there is a trade-off between model variance and bias (Figure 3) depending on the selection of the λ. When λ is small, regularization is weak, model variance is high and bias is low. In case of high noise, over fitting is high. When λ is large, regularization is strong, model variance is low and bias increases. Thus the model under fitting will be dominant. Typical methods for optimizing the hyperparameter include Mallows and cross validation [*Frank*, 1989], the Akaike information criterion [*Yamaoka et al.*, 1978], the Bayesian information criterion [*Weakliem*, 1999] and the HKB index [*Hoerl et al.*, 1975]. We select HKB index for this study. Figure 3 shows the variance-bias trade-off, and

the preferred hyperparameter based on HKB is 300 (definitions of model variance, bias and HKB index are given in equation 5-7). Figure 4 shows the model resolutions [Chapter 4, *Menke*, 1989] for OLS and RR. For OLS, because the inversion is over-determined, the model resolution is an identical diagonal matrix. For RR, because of the shrinkage, the resolution decreases. But the spread of the resolution [Chapter 4, *Menke*, 1989] still concentrates within 3 neighboring coefficients (3 adjacent time epochs), suggesting that we still obtain a temporal resolution within 3 SAR cycles (33 days for TSX data) for most of the dates.

$$Var\left(m_\lambda^{RR}\right)=\sigma^2 B_\lambda \left(G^T G\right)^{-1} B_\lambda^T$$
$$B_\lambda=\left[I+\lambda\left(G^T G\right)^{-1}\right]^{-1} \quad (5)$$

$$\left\|m_\lambda\right\|=\left(m_\lambda^T m_\lambda\right)^{1/2} \quad (6)$$

$$\lambda_{HKB}=\frac{p\sigma^2}{m^T m} \quad (7)$$

$Var\left(m_\lambda^{RR}\right)$ is the estimated model variance of RR, σ^2 is the data variance, $\left\|m_\lambda\right\|$ is the measure of the estimated model, and its ratio to the OLS model indicates the relative shrinkage (bias) of the model, λ_{HKB} is the HKB index, *p* is the number of unknown regression coefficients (here the number of velocities to be estimated in SBAS).

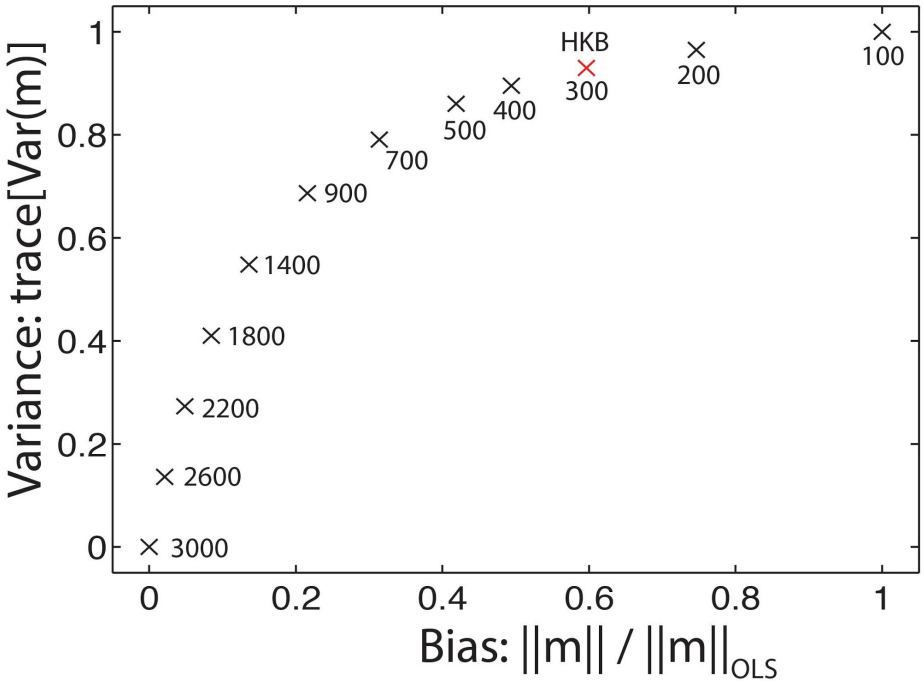

Figure 6.3. *Variance-Bias trade off of RR. Horizontal axis: the ratio between the measure of RR model and the OLS model, indicating the relative shrinkage (bias). Smaller values represent being away from the OLS model, which are more biased. Vertical axis: Variance of the RR model represented by the trace of variance-covariance matrix. Both X and Y axes are normalized to [0, 1]. The crosses represent the selected hyperparamters. The preferred hyperparameter based on HKB criterion is 300 (red cross).*

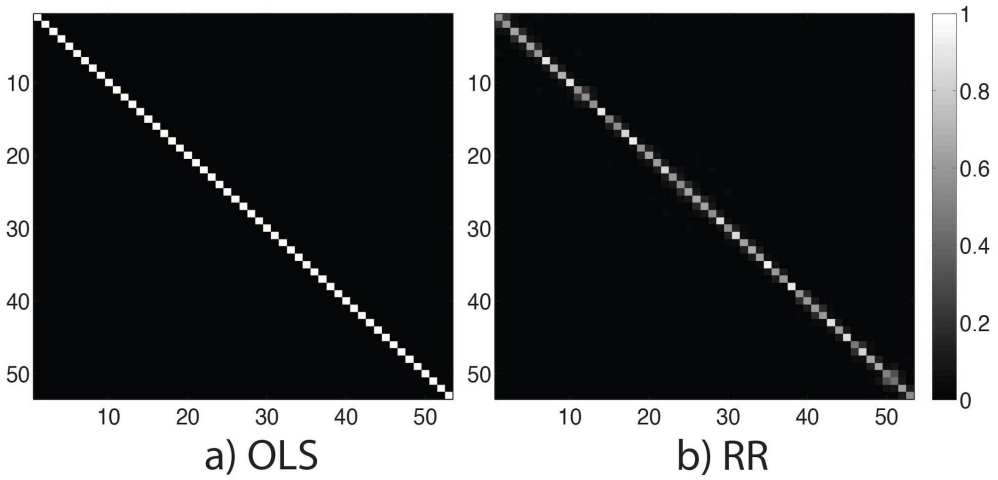

Figure 6.4. *Model resolutions. a) OLS. b) RR.*

6.7. **Results and discussion**

The final InSAR LOS deformation after RR is shown in Figure 5. We compare the LOS time-series at point A derived from OLS and RR (Figure 6). The variations between adjacent dates in OLS are higher than RR, indicating a larger model variance. Optimized by HKB index, RR performs the best estimates under the given noise level.

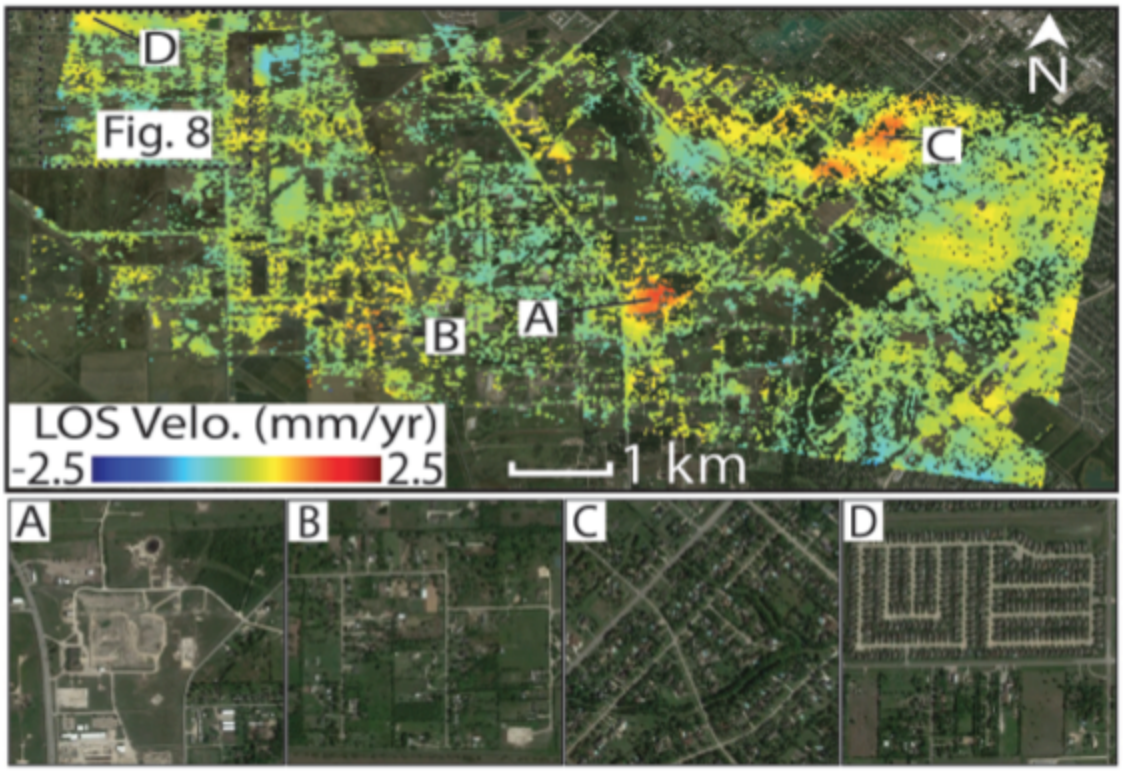

Figure 6.5. *InSAR LOS velocity map from January 2012 to April 2014. Four big deforming areas are marked on the map (A-D). A is located at the center of the Hastings formation, and is the largest operation site. B is at the western boarder of the Hastings formation. C and D are two residential areas. The maximum LOS velocities at these areas are ~2 mm/yr, ~2 mm/yr, ~2 mm/yr, ~0.5 mm/yr respectively. The dashed frame draws the location of Figure 7.*

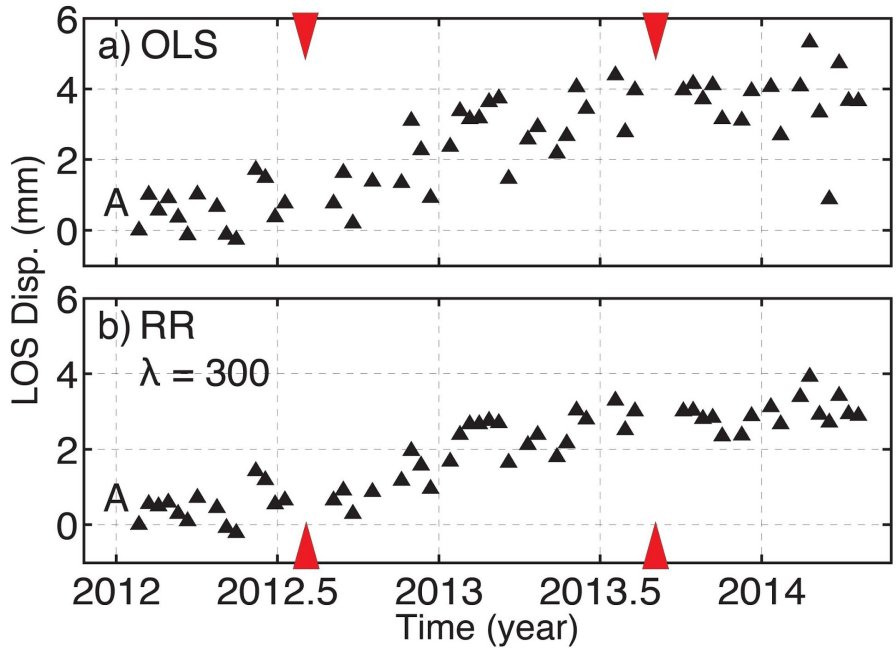

Figure 6.6. *Comparison between OLS and RR at point A (Figure 4). a) OLS. b) RR at λ = 300 based on HKB index. OLS provides a general solution of the deforming history and a clear uplift signal in the velocity map. However, because of the noise in the interferograms, the regression coefficients are likely to be over fitted. The time-series does not show clear deformation evolution at monthly or weekly scales. RR overcomes this issue, and the time-series is smoother which is real for geomechanical processes. By choosing a bigger hyperparamter, we can obtain an even smoother time-series. However, that increases the risk of under fitting. Thus we choose the hyperparamter based on the HKB index, and get the optimized value at 300. Red triangles represent the 2 data gaps.*

The observed velocity field includes four big anomalies (A-D in Figure5). We suggest that these signals are related to the local salt water pumping. However, more ground information is required for the verification. The biggest

uplift signal (point A in Figure 5) is at an obsolete operation zone in Hastings East. Several salt water disposal systems are close to this area [*McWilliams*, 1972], which are likely the source of the deformation. The circle shaped deformation area is about 800 m in diameter. The total uplift since 2012 is ~3 mm with an annual rate of ~2 mm/yr. This signal can be divided to three phases (Figure 7): 1) Spring 2012 – summer 2012, the area starts uplifting with a small rate (~2 mm/yr); 2) Summer 2012 – Summer 2013, the uplift rate accelerates to ~4 mm/yr; 3) After summer 2013, the area becomes relatively stable with very small uplift. Similar deformation is detected at point B (Figure 5). This area is about 500 m (the area is larger in the OLS result but noisy) in diameter with a linear uplift of ~4 mm since 2012, and an annual rate of ~2 mm/yr.

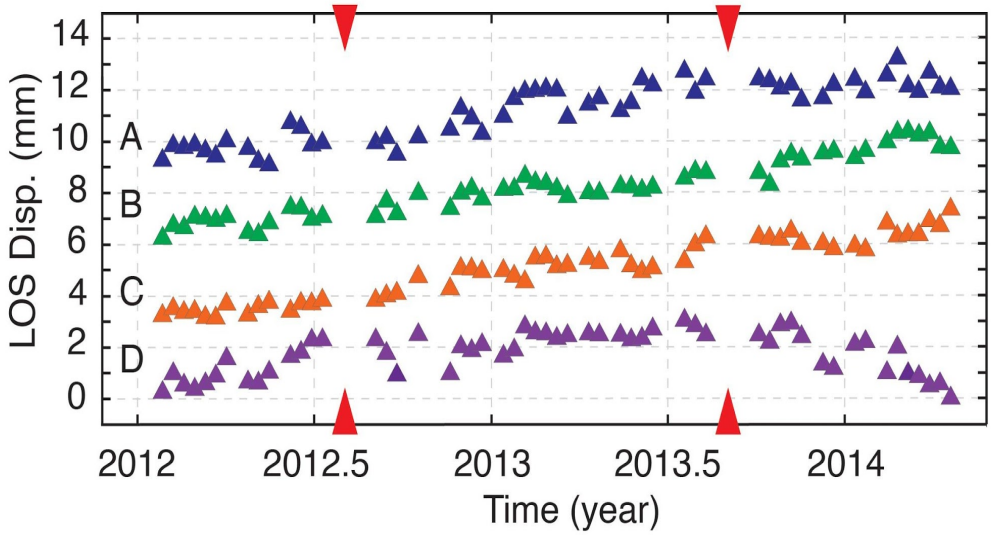

Figure 6.7. *Final time-series after RR at the four selected points (A-D). A, B, and C are shifted by 9 mm, 6 mm, and 3 mm respectively. The deformation at A has roughly three phases: spring 2012 – summer 2012 with slow uplift, summer 2012 – summer 2013 with faster uplift, summer 2013 – April 2014 with a more stable behavior. The total LOS displacement is ~3 mm. The time-series B and C are*

nearly linear with 3 and 4 mm LOS displacement respectively. The deformation at D includes an uplift of ~2 mm before summer 2013, and a subsidence of ~2 mm after. Red triangles represent the 2 data gaps.

Two residential areas are detected to be deforming. These two areas are ~4 km to the north-west (C in Figure 5) and ~7 km to the east (D in Figure 5) of point A in Figure 4 (center of the Hastings oil field). Point C is uplifting by a rate of ~2 mm/yr. Velocity at point D is almost flat. But the deformation at this point has two phases (Figure 8). Before summer 2013, this area slowly uplifts with a maximum amount of ~2 mm, and after that it quickly subsides with a maximum amount of ~2 mm in half year.

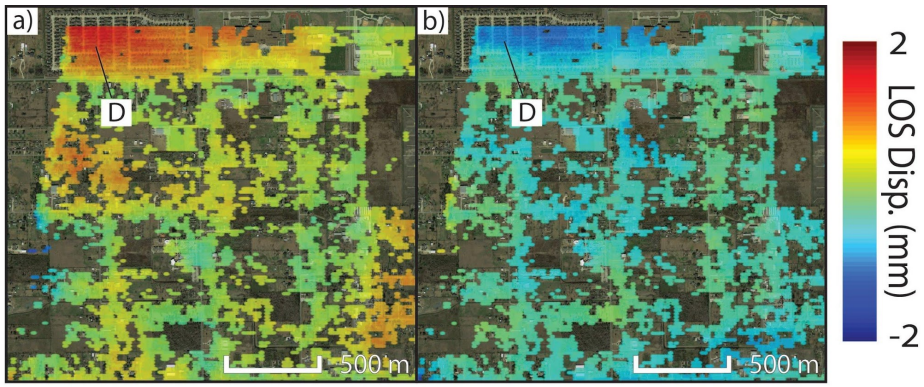

Figure 6.8. *Two deforming phases around point D. a) Uplift phase, spring 2012 – summer 2013 with ~2 mm LOS displacement. b) Subsidence phase, summer 2013 – April 2014 with ~2 mm LOS displacement.*

Three continuous GPS stations have been installed in the study area (TEST1, 2, 3 in Fig. 1) since October 2012. Both InSAR and GPS do not find significant surface deformation due to injection after summer 2012 (Figure 9).

However, the amplitude of InSAR derived deformation is smaller than GPS. One possible explanation is the existence of background deformation signal, which InSAR measurement is insensitive to. The vegetation in the injection zone also affects the accuracy of InSAR results. We also compare the InSAR derived deformation at TEST1 with a bore hole pressure measurement close to this site (Figure 10). The InSAR time-series likely retrieves the rapid pressure decrease in Spring 2012. However, due to the noise level, it is hard to conclude on the use of this sub-millimeter deformation.

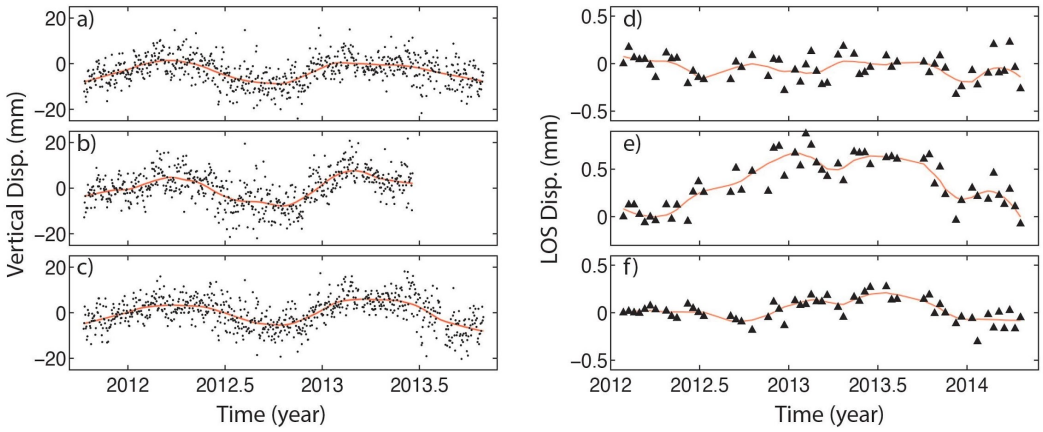

Figure 6.9. *GPS vertical and InSAR LOS time-series. a), b), and c): GPS TEST1, TEST2 and TEST3. d), e) and f): InSAR points at TEST1, TEST2 and TEST3. Red line: smoothed time-series based on a 3-month kernel.*

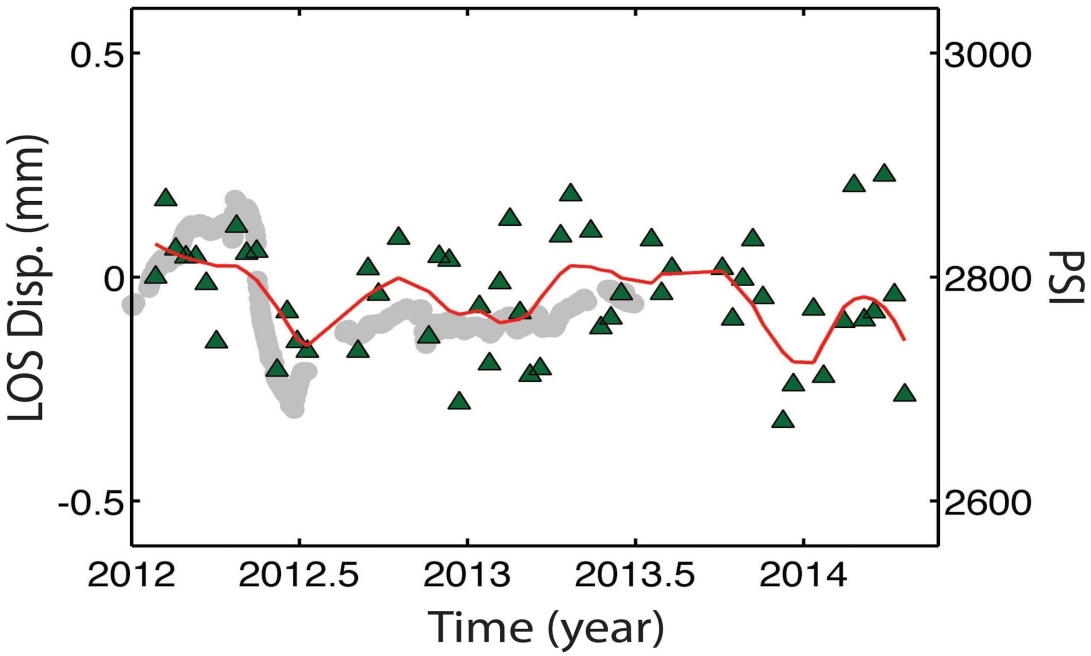

Figure 6.10. *InSAR-pressure comparison. Gray dots: bore hole pressure records measured at a well close to TEST1. Green triangles: InSAR time-series at TEST1. Red line: smoothed InSAR time-series.*

Chapter 7

Conclusions

7.1. Summary of contributions

As more and more satellite loaded with SAR sensor being launched, we are now able to have very long-time InSAR time-series. Based on new techniques developed in time-series analysis, the effects of processing and external errors are minimized. Millimeter level surface deformation derived from InSAR starts to be commonly used by geophysical researchers. By taking this advantage and InSAR's high spatial resolution, new applications and new models are potentially able to be designed. We discussed several attempts in this dissertation. Although the existing of uncertainties on the proposed works, we conclude that we have made contributions at least from several aspects below:

1. We used modified SBAS method to implement InSAR time-series and obtain centimeter to millimeter level surface deformation at 5 different sites, proving the generality and quality of InSAR time-series analysis

2. We developed a complete geophysical model for ice mass loss estimation with constraint on the geometric shape of thinning rates, and successfully applied it to Vatnajokull ice cap, Iceland.
3. We suggested another potential strategy for ice mass loss estimation on a more mathematical aspect with techniques such as model space resampling, local smoothness constraint, and inequality constraints on model. And we applied this method to Barnes ice cap, Canada, updating its ice mass loss between 2012 and 2015.
4. We obtained an extremely small deformation signal at Yangzhuoyong Lake (~1.5 mm/yr and 10 mm in 7 years) using Envisat ASAR data. We also provided constraint on the shallow crustal Young's modulus based on InSAR observation, and compared this result with seismic derived parameters, demonstrating the difference between static and dynamic moduli.
5. We used high resolution TSX data to monitor the crust response due to CCS injection and water pumping, and generated a very high temporal resolution InSAR time-series.

7.2. Future work

Corresponding to the 5 contributions we made, future plans potentially improve these works are listed below:

1. Investigations on different error sources such as DEM error, atmospheric delay and unwrapping errors can further increase the reliability of InSAR products.
2. The assumption that the ice thinning rate is exponentially correlated with distance from the ice edge is generally valid for most small ice cap. But for big ice sheets like Greenland, this assumption is too arbitrary. So that more sophisticated model is expected in the future.
3. Although the 3 constraints added in chapter 3 are plausible, in practice, the quality of products are affected by the quality of observations significantly.
4. High temporal sampling of SAR acquisition is expected at Yangzhuoyong Lake in order to retrieve this small deformation signal in time with higher significance. TSX data is like suitable for this study.
5. In rural areas at CCS injection sites, distributed InSAR may have stronger ability to retrieve reliable information.

BIBLIOGRAPHY

Auriac A., K. H. Spaans, F. Sigmundsson, A. Hooper, P. Schmidt, and B. Lund (2013), Iceland rising: solid Earth response to ice retreat inferred from satellite interferometry and viscoelastic modeling, Journal of Geophysical Research, 118, 1331-1344, doi: 10.1002/jgrb.50082.

Auriac, A., F. Sigmundsson, A. Hooper, K. H. Spaans, H. Bjornsson, F. Palsson, V. Pinel and K. L. Feigl (2014), InSAR observations and models of crustal deformation due to a glacial surge in Iceland, Geophysical Journal International, 198(3): 1329-1341, doi: 10.1093/gji/ggu205.

Alsdorf D., L. Brown, K. D. Nelson, Y. Makovsky, S. Klemperer and W. Zhao (1998), Crustal deformation of the Lhasa terrane, Tibet plateau from project INDEPTH deep seismic reflection profiles, Tectonics, 17 (4), 501-519.

Amos, C. B., P. Audet, W. C. Hammond, R. Burgmann, I. A. Johanson and G. Blewitt (2014), Uplift and seismicity driven by groundwater depletion in central California, Nature, 509, 483-486, doi: 10.1038/nature13275.

Árnadóttir, T., B. Lund, W. Jiang, H. Geirsson, H. Björnsson, P Einarsson, and T. Sigurdsson (2009), Glacial rebound and plate spreading: results from the first countrywide GPS observations in Iceland, Geophysical Journal International, 177, 691-716, doi: 10.1111/j.1365-246X.2008.04059.x.

Baker, S. and F. Amelung (2012), Top-down inflation and deflation at the summit of Kīlauea Volcano, Hawaii observed with InSAR, Journal of Geophysical Research, doi: 10.1029/2011JB009123.

Barnhoorn A., W. van der Wal, M. R. Drury (2011), Upper mantle viscosity and lithospheric thickness under Iceland, Journal of Geodynamics, 52, 260-270, doi: 10.1016/j.jog.2011.01.002.

Bernardino, P., G. Fornaro, R. Lanari, and E. Sansosti (2002), A new algorithm for surface deformation monitoring based on small baseline differential SAR interferograms, IEEE Trans. On Geoscience and Remote Sensensing, 40, 2375-2383, doi: 10.1109/TGRS.2002.803792.

Bevis M., D. Alsdorf, E. Kendrick, L. P. Fortes, B. Forsberg, R. Smalley Jr. and J. Becker (2005), Seasonal fluctuations in the mass of the Amazon River system and Earth's elastic response, Geophysical Research Letters, 32, L16308, doi: 10.1029/2005GL023491.

Bevis M. et al. (2012), Bedrock displacements in Greenland manifest ice mass variations, climate cycles and climate change, Proceedings of the National Academy of Sciences of the United States of America, doi: 10.1073/pnas.1204664109.

Biggs J., T. Wright, Z. Lu and B. Parsons (2007), Multi-interferogram method for measuring interseismic deformation: Denali fault, Alaska, Geophysical Journal International, 170, 1165-1179, doi: 10.1111/j.1365-246X.2007.03415.x.

Bissell, R. C., Vasco, D. W., Atbi, M., Hamdani, M., Okwelegbe, M., and Goldwater, M. H., 2011. A full filed simulation of the In Salah gas production and CO2 storage project using a coupled geo-mechanical and thermal fluid flow simulator. Energy Procedia, 4, 3290-3297, doi: 10.1016/j.egypro.2011.02.249.

Björnsson H., F. Pálsson (2008), Icelandic glaciers. Jökull, 58, 365-386.

Björnsson H., F. Pálsson, S. Gudmundsson, E. Magnússon, G. Adalgeirsdóttir, T. Jóhannesson, E. Berthier, O. Sigurdsson, and T. Thorsteinsson (2013), Contribution of Icelandic ice caps to sea level rise: Trends and variability since the Little Ice Age, Geophysical Research Letters, 40, 1-5, doi: 10.1002/grl.50278.

Borsa, A. A., D. C. Agnew and D. R. Cayan, Ongoing drought-induced uplift in the western United States, Science, 345, No. 6204, 1587-1590, doi: 10.1126/science.1260279.

Brown, L. D., W. Zhao, K. D. Nelson, M. Hauck, D. Alsdorf, A. Ross, M. Cogan, M. Clark, X. Liu and J. Che (1996), Bright spots, structure, and magmatism in southern Tibet from INDEPTH seismic reflection profiling, Science, 274, 5293, 1688-1690, doi: 10.1126/science.274.5293.1688.

Bufler, H. (1971), Theory of elasticity of a multilayered medium, Journal of Elasticity, 1 (2), 125-143.

Cavalie O., M.-P. Doin, C. Lasserre, and P. Briole (2007), Ground motion measurement in the Lake Mead area, Nevada, by differential synthetic aperture radar interferometry time series analysis: Probing the lithosphere rheological structure, Journal of Geophysical Research, 112, B03403, doi: 10.1029/2006JB004344.

Chamoli, A., A. R. Lowry and T. N. Jeppson (2014), Implications of transient deformation in the northern Basin and Range, western United States, Journal of Geophysical Research, 119 (5), 4393-4413, doi: 10.1002/2013JB010605.

Chanard K., J. P. Avouac, G. Ramillien and J. Genrich (2014), Modeling deformation induced by seasonal variations of continental water in the Himalaya region: Sensitivity to Earth elastic structure, Journal of Geophysical Research, doi: 10.1002/2013JB010451.

Chen, C. W. and H. A. Zebker (2001), Two-dimensional phase unwrapping with use of statistical models for cost functions in nonlinear optimization, Journal of the Optical Society of America A, 18 (2), 338-351, doi: 10.1364/JOSAA.18.000338.

Chen J. L. et al. (2006), Satellite gravity measurements confirm accelerated melting of Greenland ice sheet, Science, 313, 1958-1960, doi: 10.1126/science.1129007.

Chen J. L., C. R. Wilson, D. Blankenship and B. D. Tapley (2009), Accelerated Antarctic ice loss from satellite gravity measurements, Nature Geoscience, 2, 859-862, doi: 10.1038/NGEO694.

Chu D., D. Wang, Q. Pu, J. De, B. La, B. Pu, X. Zhang and R. Sun (2012a), A model for the remote sensing monitoring of Yangzhuoyong lake and recent variation, Chinese Journal of Glaciology and Geocryology (in Chinese), 34 (3), doi: 1000-0240(2012)03-0530-08.

Chu D., P. Qiong, D. Wang, C. Mima, Z. Laba, X. Zhang, and R. Sun (2012b), Water level variations of Yamzho Yumco Lake in Tibet and the main driving forces, Journal of Mountain Science (in Chinese), 30(2), doi: 1008-2786-(2012)2-239-09.

Doin M. P., F. Lodge, S. Guillaso, R. Jolivet, C. Lasserre, G. Ducret, R. Grandin, E. Pathier and V. Pinel (2011), Presentation of the small baseline NSBAS processing chain on a case example: the Etna deformation monitoring from 2003 to 2010 using Envisat data, Proc. ESA Fringe 2011.

Ducret G., M. P. Doin, R. Grandin, C. Lasserre and S. Guillaso (2014), DEM corrections before unwrapping in a small baseline strategy for InSAR time series analysis, IEEE Geoscience and Remote Sensing Letters, 11 (3), doi: 10.1109/LGRS.2013.2276040.

Dyke, A.S.; Prest, V.K. (1987), Late Wisconsinan and Holocene History of the Laurentide Ice Sheet, *Géographie physique et Quaternaire* **41** (2): 237–263.

Dziewonski, A. M., D. L. Anderson, (1981), Preliminary reference Earth model, Physics of the Earth and Planetary Interiors, 25 (4), 297–356, doi:10.1016/0031-9201(81)90046-7.

Ewert H., A. Groh and R. Dietrich (2011), Volume and mass changes of the Greenland ice sheet inferred from ICESat and GRACE, Journal of Geodynamics, doi: 10.1016/j.jog.2011.06.003.

Fattahi H., F. Amelung (2013), DEM error correction in InSAR time series, IEEE Transaction on Geoscience and Remote Sensing, 99, 1-11, doi:10.1109/TGRS.2012.2227761.

Fattahi, H. and F. Amelung, (2014), InSAR uncertainty due to orbital errors, Geophy J. Int, 199 (1), 549-560, doi: 10.1093/gji/ggu276

Ferretti A., C. Prati, and F. Rocca (2001), Permanent scatterers in SAR interferometry, IEEE Trans. On Geoscience and Remote Sensing, 39 (1), 8-20.

Fjaer E., R. M. Holt, P. Horsrud, A. M. Raaen and R. Risnes (2008), Petroleum related rock mechanics, 2nd edition, Elsevier.

Foulger, G.R. and J.H. Natland (2003), Is “hotspot” volcanism a consequence of plate tectonics?, Science, 300, 921-922.

Frank, I. E., 1989. Comparative Monte Carlo study of biased regression techniques. Technical report, Dept. of Statistics, Stanford University.

Fu Y., J. T. Freymueller (2012), Seasonal and long-term vertical deformation in Nepal Himalaya constrained by GPS and GRACE measurements, J. Geophys. Res., 117, B03407, doi:10.1029/2011JB008925.

Fu, Y., J. T. Freymueller, and T. Jensen (2012), Seasonal hydrological loading in southern Alaska observed by GPS and GRACE, Geophys. Res. Lett., 39, L15310, doi:10.1029/2012GL052453.

Fukushima, Y., V. Cayol and P. Durand (2005), Finding realistic dike models from interferometric synthetic aperture radar data: The February 2000 eruption at Piton de la Fournaise, Journal of Geophysical Research, 110 (B3), doi: 10.1029/2004JB003268.

Gardner A. S. et al. (2013), A reconciled estimate of glacier contributions to sea level rise: 2003 to 2009, Science, 340, 852-857, doi: 10.1126/science.1234532.

Geirsson, H., P. LaFemina, Th. Árnadóttir, E. Sturkell, F. Sigmundsson, M. Travis, P. Schmidt, B. Lund, S. Hreinsdóttir, and R. Bennett (2012), Volcano deformation at active plate boundaries: Deep magma accumulation at Hekla volcano and plate boundary deformation in south Iceland, Journal of Geophysical Research, 117, B11409, doi:10.1029/2012JB009400.

Gourmelen N., F. Amelung, F. Casu, M. R. Manzo, R. Lanari (2007), Minning-related ground deformation in Crescent Valley, Nevada: Implications for sparse

GPS networks, Geophysical Research Letters, 34, L09309, doi: 10.1029/2007GL029427.

Gourmelen N., F. Amelung, and R. Lanari (2010), Interferometric synthetic aperture radar-GPS integration: Interseismic strain accumulation across the Hunter Mountain fault in the eastern California shear zone, Journal of Geophysical Research, 115, B09408, doi: 10.1029/2009JB007064.

Govers, R. and M.J.R. Wortel (2005) Lithosphere tearing at STEP faults: Response to edges of subduction zones, Earth and Planetary Science Letters, 236, 505–523.

Grandin, R., M-P. Doin, L. Bollinger, B. Pinel-Puyssegur, G. Ducret, R. Jolivet and S. N. Sapkota (2012), Long-term growth of the Himalaya inferred from interseismic InSAR measurement, Geology, 40 (12), 1059-1062, doi: 10.1130/G33154.1.

Grapenthin, R., F. Sigmundsson, H. Geirsson, T. Árnadóttir, and V. Pinel (2006), Icelandic rhythmics: Annual modulation of land elevation and plate spreading by snow load, Geophysical Research Letters, 33, L24305, doi:10.1029/2006GL028081.

Grosfils, E. B., P. J. McGovern, P. M. Gregg, G. A. Galgana, D. M. Hurwitz, S. Long, and S. Chestler (2013), Elastic models of magma reservoir mechanics: A key tool for understanding planetary volcanism, in Volcanism and Tectonism Across the Solar System, edited by M. Massironi et al., Geol. Soc. London Spec. Publ., SP401.

Gu, Z., Y. Pan, Y. Zhou, C. Wu, L. Yu, C. Song and J. Tao (2000), The physical properties of crustal low velocity layer in Qinghai-Xizang plateau, Bulletin of Mineralogy, Petrology and Geochemistry (in Chinese), 19 (1), 30-33.

Hastie, T., R. Tibshirani, and J. Friedman (2009), The elements of statistical learning: data mining, inference and prediction. Springer.

Heap, M. J., Baud, P., Meredith, P. G., Vinciguerra, S., & Reuschlé, T. (2014). The permeability and elastic moduli of tuff from Campi Flegrei, Italy: implications for ground deformation modelling. Solid Earth, 5(1), 25-44.

Heidemann, H. K., 2012. Lidar base specification version 1.0. Chapter 4 of Section B, U.S. Geological Survey Standards.

Hoerl, A. E., 1962. Application of ridge analysis to regression problems. Chemical Engineering Progress, 58, 54-59.

Hoerl, A. E., Kannard, R. W., and Baldwin, K. F., 1975. Ridge regression: some simulations. Communications in Statistics, 4(2), doi: 10.1080/03610927508827232.

Howat I. M., B. E. Smith, I. Joughin and T. A. Scambos (2008), Rates of southeast Greenland ice volume loss from combined ICESat and ASTER observations, Geophysical Research Letters, 35, L17505, doi: 10.1029/2008GL034496.

Howat, I.M., A. Negrete, B.E. Smith, 2014, The Greenland Ice Mapping Project (GIMP) land classification and surface elevation datasets, The Cryosphere, 8, 1509-1518, doi:10.5194/tc-8-1509-2014.

Institute of Geology and Geophysics, Chinese Academy of Sciences (1981), Explosion seismic study for velocity distribution and structure of the crust and upper mantle from Damxung to Yadong of Xizang plateau, Acta Geophysica Sinica, 24 (2), 156-170.

Jacob T., J. Wahr, W. T. Pfeffer & S. Swenson, Recent contributions of glaciers and ice caps to sea level rise, Nature, 2012, 482, 514-518, doi: 10.1038/nature10847.

Jiang Y., T. H. Dixon and S. Wdowinski (2010), Accelerating uplift in the North Atlantic region as an indicator of ice loss, Nature Geoscience, 3, 404-407, doi: 10.1038/NGEO845.

Jolivet, R., P. S. Agram, N. Y. Lin, M. Simons, M.-P. Doin, G. Peltzer and Z. Li (2014), Improving InSAR geodesy using global atmospheric models, Journal of Geophysical Research, 119 (3), 2324-2341, doi: 10.1002/2013JB010588.

Jonsson, S., H. Zebker, P. Segall, and F. Amelung (2002), Fault Slip Distribution of the 1999 Mw7.1 Hector Mine Earthquake, California, estimated from Satellite Radar and GPS Measurements, Bull. Seismol. Soc. Am., 92, 1377-1389.

Jónsson S. (2008), Importance of post-seismic viscous relaxation in southern Iceland, Nature Geoscience, 1, 136-139, doi:10.1038/ngeo105.

Joughin I. (2002), Ice-sshet velocity mapping: A combined interferometric and speckle-tracking approach, Annals of Glaciology, 34, 195-201, doi:10.3189/17275640278187978.

Joughin, I., I. Howat, B. Smith, T. Scambos (2011), MEaSUREs Greenland Ice Velocity: Selected Glacier Site Velocity Maps from InSAR. Boulder, Colorado, USA: National Snow and Ice Data Center. Digital media.

Kaufmann, G. and F. Amelung (2000), Reservoir-induced deformation and continental rheology in vicinity of Lake Mead, Nevada , Journal of Geophysical Research, 105 , B7, 16,341, doi: 10.1029/2000JB900079.

Khan S. A., J. Wahr , L. A. Stearns, G. S. Hamilton, T. van Dam, K. M. Larson, and O. Francis (2007), Elastic uplift southeast Greenland due to rapid ice mass loss, Geophysical Research Letters, 34, L21701, doi:10.1029/2007GL031468.

Khan S. A., J. Wahr, M. Bevis, I. Velicogna and E. Kendrick (2010), Spread of ice mass loss into northwest Greenland observed by GRACE and GPS, Geophysical Research Letters, 37, L06501, doi: 10.1029/2010GL042460.

Krabill, W. B., IceBridge ATM L2 Icessn Elevation, Slope, and Roughness, (May 1995; May to June 2000; May 2005; May 2011). Boulder, Colorado USA: National Snow and Ice Data Center. Digital media, 2011.

Kuipers Munneke P., S. Ligtenberg, B.P.Y. Noël, I.M. Howat, J.E. Box, E. Mosley-Thompson, J.R. McConnell, K. Steffen, J.T. Harper, S.B. Das, M.R. Van Den Broeke (2015) Elevation change of the Greenland Ice Sheet due to surface mass balance and firn processes, 1960–2014, Cryosphere, 9 (6) (2015), pp. 2009–2025 http://dx.doi.org/10.5194/tc-9-2009-2015

LaFemina P. C., T. H. Dixon, R. Malservisi, T. Árnadóttir, E. Sturkell, F. Sigmundsson, and P. Einarsson (2005), Geodetic GPS measurements in south Iceland: Strain accumulation and partitioning in a propagating ridge system, Journal of Geophysical Research, 110, B11405, doi:10.1029/2005JB003675.

Lasserre C., G. Peltzer, F. Crampe, Y. Klinger, J. Van der Woerd, and P. Tapponnier (2005), Coseismic deformation of the 2001 Mw = 7.8 Kokoxili earthquake in Tibet, measured by synthetic aperture radar interferometry, Journal of Geophysical Research, 110, B12408, doi: 10.1029/2004JB003500.

Lenaerts J. T., J. H. van Angelen, M. R. van den Broeke, A. S. Gardner, B. Wouters, and E. van Meijgaard (2013), Irreversible mass loss of Canadian Arctic Archipelago glaciers, Geophysical Research Letters, 40, 870-874, doi: 10.1002/grl.50214.

Li L., J. Li, X. Yao, J. Luo, Y. Huang and Y. Feng (2014), Changes of the three holy lakes in recent years and quantitative analysis of the influencing factors, Quaternary International, 1-7, doi: 10.1016/j.quaint.2014.04.051.

Li. J., A. S. Gardner, M. Gibb (2014), Mapping extent changes of the Barnes ice cap since the Little Ice Age, Abstract C31B-0284 presented at 2014 Fall Meeting, AGU, San Francisco, Calif., 15-19 Dec.

Li J., H. J. Zwally (2011), Modeling of firn compaction for estimating ice-sheet mass change from observed ice-sheet elevation change, Annals of Glaciology, 52(59), doi: 10.3189/172756411799096321.

Liao J., G. Shen and Y. Li (2013), Lake variations in response to climate change in the Tibetan Plateau in the past 40 years, International Journal of Digital Earth, 6:6, 534-549, doi: 10.1080/17538947.2012.656290.

Lin, Y. N., Andrew, P. K., and Avouac, J., 2010. PCAIM joint inversion of InSAR and ground-based geodetic time series: Application to monitoring magmatic inflation beneath the Long Valley Caldera. Geophysical Research Letters, 37, L23301, doi: 10.1029/2010GL045769.

Liu L., J. Wahr, I. Howat, S. A. Khan, I. Joughin and M. Furuya (2012), Constraining ice mass loss from Jakobshavn Isbræ (Greenland) using InSAR-measured crustal uplift, Geophysical Journal International, doi: 10.1111/j.1365-246X.2011.05317.x.

Lohman R. B. and M. Simons (2005), Some thoughts on the use of InSAR data to constrain models of surface deformation: Noise structure and data downsampling, Geochemistry, Geophysics, Geosystems, 6-1, Q01007, doi: 10.1029/2004GC000841.

Marshall, S. J., H. Björnsson, G. E. Flowers, and G. K. C. Clarke (2005), Simulation of Vatnajökull ice cap dynamics, Journal of Geophysical Research, 110, F03009, doi:10.1029/2004JF000262.

Mashinsky E. I. (2003), Differences between static and dynamic elastic moduli of rocks: physical causes, Russian Geology, 44 (9), 953-959.

McWilliams J. (1972), Large Saltwater-Disposal Systems at East Texas and Hastings Oil Fields, Texas, AAPG special Volumes, A075, 331-339.

Mechie J., S. V. Sobolev, L. Ratschbacher, G. Bock, A. G. Jones, K. D. Nelson, L. D. Brown, and W. Zhao (2004), Precise temperature estimation in the Tibetan crust from seismic detection of the α-β quartz transition, Geology, 32, 7, 601-604, doi: 10.1130/G20367.1.

Meier M. F., M. B. Dyurgerov, U. K. Rick, S. O'Neel, W. T. Pfeffer, R. S. Anderson, S. P. Anderson, A. F.Glazovsky (2007), Glaciers dominate eustatic sea-level rise in the 21st century, Science, 317, 1064, doi:10.1126/science.1143906.

Menke W. (1989), Geophysical data Analysis: Discrete Inverse Theory (revised edition), Academic Press, Inc..

Meyer F. (2011), Performance requirements for ionospheric correction of low-frequency SAR data, IEEE Transaction on Geoscience and Remote Sensing, 49(10), 3694-3702, doi: 10.1109/TGRS.2011.2146786.

Mitrovica J. X., G. A. Milne and J. L. Davis (2001), Glacial isostatic adjustment on a rotating earth, Geophysical Journal International, 147, 562-578.

Nof R. N., A. Ziv, M.-P. Doin, G. Baer, Y. Fialko, S. Wdowinski, Y. Eyal, and Y. Bock (2012), Rising of the lowest place on Earth due to Dead Sea water-level drop: Evidence from SAR interferometry and GPS, Journal of Geophysical Research, 117, B05412, doi: 10.1029/2011JB008961.

Ozawa, T., and Ueda, H., 2011. Advanced interferometric synthetic aperture radar (InSAR) time series analysis using interferograms of multiple-orbit tracks: A case study on Miyake-jima. Journal of Geophysical Research, 116, B12407, doi: 10.1029/2011JB008489.

Pagli, C., F. Sigmundsson, B Lund, E. Sturkell, H. Geirsson, P. Einarsson, T. Árnadóttir and S. Hreinsdottir, (2007a), Glacio-isostatic deformation around the Vatnajökull ice cap, Iceland, induced by recent climate warming: GPS observations and finite element modeling, Journal of Geophysical Research, 112, B08405, doi:10.1029/2006JB004421.

Pagli C., F. Sigmundsson, R. Pedersen, P. Einarsson, T. Árnadóttir and K. L. Feigl (2007b), Crustal deformation associated with the 1996 Gjalp subglacial eruption, Iceland: InSAR studies in affected areas adjacent to the Vatnajökull ice cap, Earth and Planetary Science Letters, 259, 24-33, doi: 10.1016/j.epsl.2007.04.019.

Pagli, C., and F. Sigmundsson (2008), Will present day glacier retreat increase volcanic activity? Stress induced by recent glacier retreat and its effect on magmatism at the Vatnajökull ice cap, Iceland, Geophysical Research Letters, 35, L09304, doi:10.1029/2008GL033510.

Pan, E. (1989), Static response of a transversely isotropic and layered half-space to general dislocation sources, Physics of the Earth and Planetary Interiors, 58, 103-117.

Peltier W. R. (1974), The Impulse Response of a Maxwell Earth, Reviews of Geophysics and Space Physics, 12, 4, 651-665.

Peltzer et al., Evidence of nonlinear elasticity of the crust from the Mw7.6 Manyi (Tibet) earthquake (1999), Science, 286, 272, doi: 10.1126/science.286.5438.272.

Pinel V., F. Sigmundsson, E. Sturkell, H. Geirsson, P. Einarsson, M. T. Gudmundsson and T. Hognadottir (2006), Discriminating volcano deformation due to magma movements and variable surface loads: application to Katla subglacial volcano, Iceland, Geophysical Journal International, 169, 325-338, doi: 10.1111/j.1365-246X.2006.03267.x.

Popovics J. S., J. Zemajtis and I. Shkolnik (2008), A study of static and dynamic modulus of elasticity of concrete, ACI-CRC Final Report (October 2008).

Pritchard H. D., R. J. Arthern, D. G. Vaughan & L. A. Edwards (2009), Extensive dynamic thinning on the margins of the Greenland and Antarctic ice sheets, Nature, 461, 971-975, doi: 10.1038/nature08471.

Qiao X., S. Yang, R. Du, L. Ge and Q. Wang (2011), Coseismic slip from the 6 October 2008, Mw6.3 Damxung earthquake, Tibetan plateau constrained by InSAR observations, Pure and Applied Geophysics, 168, 1749-1758, doi: 10.1007/s00024-010-0190-1.

Ramillien G., A. Lombard, A. Cazenave, E. R. Ivins, M. Llubes, F. Remy and R. Biancale (2006), Interannual variations of the mass balance of the Antarctica and Greenland ice sheets from GRACE, Global and Planetary Change, 53, 198-208, doi: 10.1016/j.gloplacha.2006.06.003.

Rignot E., I. Velicogna, M. r. van den Broeke, A. Monaghan and J. Lenaerts (2011a), Acceleration of the contribution of the Greenland and Antarctic ice sheets to sea level rise, Journal of Geophysical Research, 38, L05503, doi: 10.1029/2011GL046583.

Rignot E., J. Mouginot, B. Scheuch (2011b), Ice flow of the Antarctic ice sheet, Science, 333, 1427, doi: 10.1126/science.1208336.

Rignot E., S. Jacobs, J. Mouginot, B. Sceuchl (2013), Ice-Shelf Melting Around Antarctica, Science, 341, 266, doi: 10.1126/science.1235798.

Rinaldi, A., Rutqvist, J., 2013. Modeling of deep fracture zone opening and transient ground surface uplift at KB-502 CO2 injection well, In Salah, Algeria. International Journal of Greenhouse Gas Control, 12, 155-167, doi: 10.1016/j.ijggc.2012.10.017.

Rohmer, J., Raucoules, D., 2012. On the applicability of persistent scatterers interferometry (PSI) analysis for long term CO2 storage monitoring. Engineering Geology 147-148, 137-148, doi: 10.1016/j.enggeo.2012.07.010.

Rosen P. A., S. Hensley, G. Peltzer, and M. Simons (2004), Updated Repeat Orbit Interferometry package released. Eos Trans. AGU, 85, 35.

Rutqbist, J., Vasco, D. W., and Myer, L., 2010. Coupled reservoir-geomechanical analysis of CO2 injection and ground deformations at InSalah Algeria. International Journal of Greenhouse Gas Control, 4, 225-230, doi: 10.1016/j.ijggc.2009.10.017.

Rucci, A., Vasco, D. W., and Novali, F., 2010. Fluid pressure arrival-time tomography: Estimation and assessment in the presence of inequality constraints with an application to production at the Krechba field, Algeria. Geophysics, 75(6), O39-O55, doi: 10.1190/1.3493504

Rucci, A., Vasco, D. W., and Novali, F., 2013. Monitoring the geological storage of carbon dioxide using multicomponent SAR interferometry. Geophysical Journal International, 199(1), doi: 10.1093/gji/ggs112.

Ryder I., B. Parsons, T. J. Wright and G. J. Funning (2007), Post-seismic motion following the 1997 Manyi (Tibet) earthquake: InSAR observations and modeling, Geophysical Journal International, 169, 1009-2027, doi: 10.1111/j.1365-246X.2006.03312.x.

Samsonov, S., and d'Oreye N., 2012. Multidimensional time-series analysis of ground deformation from multiple InSAR data sets applied to Virunga Volcanic Province. Geophysical Journal International, 191, 1095-1108, doi: 10.1111/j.1365-246X.2012.05669.x.

Sigmundsson F. (1991), Post-glacial rebound and asthenosphere viscosity in Iceland, Geophysical Research Letters, 18, 6, 1131-1134, doi: 10.1029/91GL01342.

Sigmundsson F., P. Einarsson (1992), Glacio-isostatic crustal movements caused by historical volume change of the Vatnajökull ice cap, Iceland, Geophysical Research Letters, 19, 21, 2123-2126, doi: 10.1029/92GL02209.

Shanker P., and H. Zebker (2009), Sparse two dimensional phase unwrapping using regular grid methods, IEEE Geosci. and Remote Sensing Letters, 6 (2), pp. 327-331.

Shepherd A. et al. (2012), A reconciled estimate of ice-sheet mass balance, Science, 338, 1183-1189, doi: 10.1126/science.1128102.

Shi, J., Sinayuc, C., Durucan, S., and Korre, A., 2012. Assessment of carbon dioxide plume behavior within the storage reservoir and the lower caprock around the KB-502 injection well at In Salah. International Journal of Greenhouse Gas Control, 7, 115-126, doi: 10.1016/j.ijggc.2012.01.002.

Slobbe D. C., P. Ditmar and R. C. Lindenbergh (2009), Estimating the rates of mass change, ice volume change and snow volume change in Greenland from ICESat and GRACE data, Geophysical Journal International, 176, 95-106, doi: 10.1111/j.1365-246X.2008.03978.x.

Sneddon, I. N. (1951), Fourier transforms, McGraw-Hill, 542 pp.

Snieder and Trampert (1999), Inverse Problems in Geophysics, reprinted from Wavefield Inversion, 119-190, Ed. A. Wirgin, Springer Verlag, New York.

Sørensen L. S., S. B. Simonsen, K. Nielsen, P. Lucas-Picher, G. Spada, G. Adalgeirsdottir, R. Forsberg and C. S. Hvidberg (2011), Mass balance of the Greenland ice sheet (2003-2008) from ICESat data – the impact of interpolation, sampling and firn density, The Cryosphere, 5, 173-186, doi:10.5194/tc-5-173-2011.

Steckler M. S., S. L. Nooner, S. H. Akhter, S. K. Chowdhury, S. Bettadpur, L. Seeber and M. G. Kogan (2010), Modeling Earth deformation from monsoon flooding in Bangladesh using hydrographic, GPS, and Gravity Recovery and Climate Experiment (GRACE) data, Journal of Geophysical Research, 115, B08407, doi: 10.1029/2009JB007018.

Sudhaus, H. and S. Jonsson (2009), Improved source modelling through combined use of InSAR and GPS under consideration of correlated data errors: application to the June 2000 Kleifarvatn earthquake, Iceland, Geophys. J. Int, 176, 389-404, doi: 10.1111/j.1365-246X.2008.03989.x.

Sun J., K. M. Johnson, Z. Cao, Z. Shen, R. Burgmann and X. Xu (2011), Mechanical constraints on inversion of coseismic geodetic data for fault slip and geometry: Example from InSAR observation of the 6 October 2008 Mw 6.3 Dangxiong-Yangyi (Tibet) earthquake, Journal of Geophysical Research, 116, B01406, doi: 10.1029/2010JB007849.

Tamburini, A., Bianchi, M., Giannico, C., and Novali, F., 2010. Retriving surface deformation by PSInSARTM reservoir monitoring. International Journal of Greenhouse Gas Control, 4, 928-937, doi: 10.1016/j.ijggc.2009.12.009.

Tao W., Z. K. Shen, Y. G. Wan et al., Crustal elasticity contrast across the East Kunlun fault in northern Tibet, inferred from InSAR measurements of the 2001 Mw 7.8 Kokoxili earthquake, Chinese Journal of Geophysics (in Chinese), 2007, 50 (3) : 744～751

Tedesco M., X. Fettweis, T. Mote, J. Wahr, P. Alexander, J. E. Box, and B. Wouters (2013), Evidence and analysis of 2012 Greenland records from spaceborne observations, a regional climate model and reanalysis data, The Cryosphere, 7, 615-630, doi: 10.5194/tc-7-615-2013.

Tedesco M., J. E. Box, J. Cappelen, X. Fettweis, T. Mote, R. S. W. van de Wal, C. J. P. P. Smeets, and J. Wahr (2015), Greenland ice sheet, Arctic report card at NOAA: update for 2014.

Tiampo K. F., P. J. Gonzalez, S. S. Samsonov (2013), Results for aseismic creep on the Hayward fault using polarization persistent scatterer InSAR, Earth and Planetary Science Letters, 367, 157-165, doi: 10.1016/j.epsl.2013.02.019.

van Dam T., J. Wahr and D. Lavallee (2006), A comparison of annual vertical crustal displacements from GPS and Gravity Recovery and Climate Experiment (GRACE) over Europe, Journal of Geophysical Research, 112, B03404, doi:10.1029/2006JB004335.

Vasco, D. W., Rucci, A., Ferretti, A., Novali, F., 2008. Reservior mornitoring and characterization using satellite geodetic data: interferometric synthetic aperture radar observations from the Krechba field, Algeria. Geophysics, 73 (6), WA113-WA112.

Vasco, D. W., Rucci, A., Ferretti, A., Novali, F., Bissell, R. C., Ringrose, P. S., Mathieson, A. S., and Wright, I. W., 2010. Satellite-based measurements of surface deformation reveal fluid flow associated with the geological storage of carbon dioxide. Geophysical Research Letters, 37, L03303, doi: 10.1029/2009GL041544.

Velicogna I. & Wahr J. (2006), Acceleration of Greenland ice mass loss in spring 2004, Nature, 443, 329-331, doi:10.1038/nature05168.

Wahr, J., S. A. Khan, T. van Dam, L. Liu, J. H. van Angelen, M. R. van den Broeke and C. M. Meertens (2013), The use of GPS horizontals for loading studies, with applications to northern California and southeast Greenland, Journal of Geophysical Research, 118 (4), 1795-1806, doi: 10.1002/jgrb.50104.

Wang, H., L. Xiang, P. Wu, H. Steffen, L. Jia, L. Jiang, and Q. Shen (2013), Effects of the Tibetan Plateau crustal structure on the inversion of water trend rates using simulated GRACE/GPS data, Terr. Atmos. Oceanic Sci., 24(4), 505–512.

Wauthier, C., V. Cayol, F. Kervyn, N. d'Oreye (2012), Magma sources involved in the 2002 Nyiragongo eruption, as inferred from an InSAR analysis, Journal of Geophysical Research, 177 (B5), doi: 10.1029/2011JB008257.

Weakliem, D. L., 1999. A critique of the Bayesian Information Criterion for model selection. Sociological Methods & Research, 27(3), doi: 10.1177/0049124199027003002.

Wouters B., D. Chambers and E. J. O. Schrama (2008), GRACE observes small-scale mass loss in Greenland, Geophysical Research Letters, 35, L20501, doi:10.1029/2008GL034816.

Wu, P., (1992), Deformation of an incompressible viscoelastic flat earth with power-law creep: a finite element approach, Geophysical Journal International, 108, 35-51.

Xia J., R. D. Miller and Y. Xu (2008), Data-resolution matrix and model-resolution matrix for Rayleigh –wave inversion using a damped least-squares method, Pure and Applied Geophysics, 165, 1227-1248, doi:10.1007/s00024-008-0364-2.

Yamaoka, K., Nakagawa, T and Uno, T., 1978. Application of Akaike's Information Criterion (AIC) in the evaluation of linear pharmacokinetic equations. Journal of Pharmacokinetics and Biopharmaceutics, 6(2).

Yang Q., S. Wdowinski, T. Dixon (2013), Annual variation of coastal uplift in Greenland as an indicator of variable and accelerating ice mass loss. (in press)

Yang, Q., W. Zhao, T. H. Dixon, F. Amelung, W. S. Han and P. Li (2015), Monitoring ground deformation due to CO2 injection at an enhanced oil recovery site, west Texas, submitted to International Journal of Greenhouse Gas Control.

Yang T., S. Yang (2005), P-wave velocity structure of the crust and uppermost mantle beneath Iceland from local earthquake tomography, Earth and Planetary Science Letters, 235, 597-609.

Yin, Z., J. Teng and H. Liu (1990), The 2-D crustal structure study in the Yadong-Damxung region of the Xizang plateau, Bulletin of the Chinese Academy of Geological Sciences (in Chinese), 21, 239-244.

Zhang G., H. Xie, S. Kang, D. Yi and S. F. Ackley (2011), Monitoring lake level changes on the Tibetan plateau using ICESat altimetry data (2003-2009), Remote Sensing of Environment, 115, 1733-1742, doi: 10.1016/j.rse.2011.03.005.

Zhang, L., Ding, X., and Lu, Z., 2011. Modeling PSInSAR time-series without phase unwrapping. IEEE Trans. On Geoscience and Remote Sensing, 49(1), doi: 10.1109/TGRS.2010.2052625.

Zhao W., et al. (1993), Deep seismic-reflection evidence for continental underthrusting beneath southern Tibet, Nature, 366, 557-559.

Zhao W., J. Mechie, L. D. Brown, J. Guo, S. haines, T. Hearn, S. L. Klemperer, Y. S. Ma, R. Meissner, K. D. Nelson, J. F. Ni, P. Pananont, R. Rapine, A. Ross and J. Saul (2001), Crustal structure of central Tibet as derived from project INDEPTH wide-angle seismic data, Geophysical Journal International, 145, 486-498.

Zhao, W., Amelung, F., Dixon, T. H., 2011. Monitoring Ground Deformation on Carbon Sequestration Reservoirs in North America. Proceedings of ESA Fringe Workshop.

Zhao W., F. Amelung, T. H. Dixon, S. Wdowinski, R. Malservisi (2014), A method for estimating ice loss from relative InSAR observations: Application to the Vatnajökull ice cap, Iceland, Geochemistry, Geophysics, Geosystems, 15 (1), 108-120, DOI: 10.1002/2013GC004936.

Zwally H. J. et al. (2011), Greenland ice sheet mass balance: distribution of increased mass loss with climate warming; 2003-07 versus 1992-2002, Journal of Glaciology, 57 (201), doi: 10.3189/002214311795306682.

Appendix A

No. of int.	Date 1	Date 2	Bperp (m)	No. of int.	Date 1	Date 2	Bperp (m)
1	20120524	20120804	-16	31	20130730	20141005	59
2	20120804	20121015	-189	32	20130823	20130916	-74
3	20120804	20130730	-148	33	20130823	20131010	-145
4	20120804	20130823	-137	34	20130823	20131103	79
5	20120804	20130916	-212	35	20130823	20140911	31
6	20120921	20121015	221	36	20130823	20141005	48
7	20120921	20130730	262	37	20130916	20131010	-71
8	20120921	20130823	273	38	20130916	20140911	106
9	20120921	20130916	199	39	20130916	20141005	122
10	20120921	20131010	127	40	20131010	20131103	224
11	20120921	20140911	304	41	20131010	20140911	177
12	20121015	20130119	32	42	20131103	20131221	-97
13	20121015	20130308	-14	43	20131103	20140207	-144
14	20121015	20130401	-23	44	20131221	20140207	-47
15	20121015	20130730	41	45	20140911	20141005	16
16	20121015	20130823	52	46	20140911	20141216	97
17	20121015	20130916	-22	47	20141005	20150202	83
18	20121015	20131010	-94	48	20141005	20150226	-15
19	20121015	20140911	83	49	20141005	20150322	65

20	20121015	20141005	100	50	20141216	20150202	3
21	20130119	20130308	-45	51	20141216	20150226	-95
22	20130119	20130401	-55	52	20141216	20150322	-16
23	20130119	20130425	252	53	20141216	20150415	-11
24	20130308	20130401	-9	54	20150202	20150226	-98
25	20130308	20130425	297	55	20150202	20150322	-18
26	20130401	20130425	306	56	20150202	20150415	-14
27	20130730	20130823	11	57	20150226	20150322	79
28	20130730	20130916	-63	58	20150226	20150415	84
29	20130730	20131010	-135	59	20150322	20150415	5
30	20130730	20140911	42				

Table S3.1. *Interferogram list (each record includes 2 dates representing the master and slave) use for time-series analysis. Bperp represents the length of perpendicular baseline.*

Appendix B

Petermann Icesat Source Data

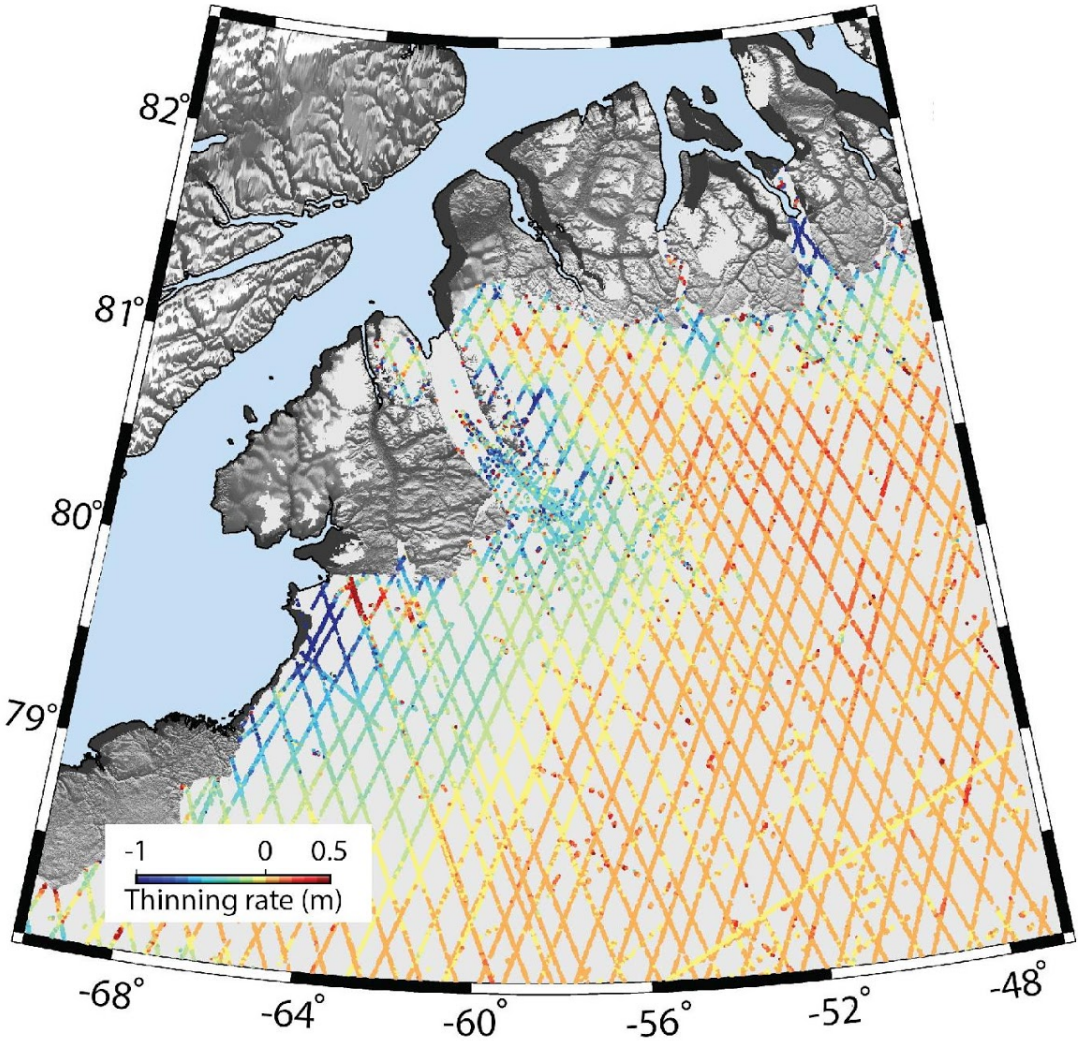

Figure 4.3. Ice thinning rate (2003 – 2010) at Petermann glacier. All points represent the Icesat foot prints.

Appendix C

Codes Developed for This Dissertation

1. **3D InSAR Time-Series (used in chapter 2)**

This matlab code is used for multi-dimensional InSAR time-series inversion (this version only works for 2 tracks case with 1 ascending and 1 descending). The main file is interferograms2timeseries_3D.m. It calls Make_designMatrix_3D.m to build the design matrix of the multi-dimensional SBAS. CalcDateList.m calculates a datelist(in date format) and dayslist(in integer) of all the epochs in the data set. yymmdd2y.m changes date format time to a decimal year. convert_unit.m changes unit between radar phase (rad) and ground displacement (m, cm or mm).

The inputs for interferograms2timeseries_3D.m are: 1) A interferogram list structure with fields of data(the phase), first_x(the left longitude), first_y(the up latitude), x_step(longitude resolution in degree), y_step(latitude resolution in degree), Unit (unit of phase usually in rad); 2) look angle list structure in order of interferogram; 3) azimuth angle list structure in order of interferogram; 4) number of data on the first track (notice: the order of interferogram list should be first

track first); 5) days before the first overlapping date (e.g. if the first date on track1 is Oct.1, and first date on track2 is Oct.15, this value should be 14); 6) similar to 5, days after the last overlapping date; 7) a interferogram list structure or data from track1

The code has been tested using matlab 2010a,b, 2011b, 2012a on centOS cluster and mac OS.

2. Glacier package (used in chapter 3 & 4)

This is a python class used for ice mass loss modeling based on InSAR data. It includes simulator or reader of a ice cap geometry (outline and area), simulator of loading history based on distance from the ice cap edge, reader of InSAR data outside of ice cap, geo-coordinate - SAR coordinate convertor, altimetry measurement simulator, quadtree decompositor, forward model, inverse model using constrained least square.

3. ElasticSAR package (used in chapter 5)

This python code is used for layered elastic modeling from InSAR time-series outputs. Users need to create a working directory, under working dir make a dir for "InSAR" and dir for "Model", then prepare a parameter text file (an example is included in the package). Two uitility libraries are included also -- Rsmas_Utilib.py and ElasticSAR.py

Users need to have numpy, scipy, mpi4py, matplotlib, gdal and osgeo pre-installed with proper environment setting.

4. **Pseudo 3D Unwrapping (used in chapter 5)**

This python code is used for unwrapping InSAR interferogram based on a pre-selected spare points network. User needs to have SNAPHU installed because the unwrapping kernel will be still SNAPHU. The code does a masking on each interferogram based on the pre-defined mask file. Then it interpolates the interferograms using nearest-neighbor algorithm. The unwrapped interferogram is sent to SNAPHU after interpolation. Another making step will be implemented after unwrapping to take out those points generated by nearest-neighbor interpolation.

Users need to setup a parameter list file specifying parameters like the working path, string character of interferogram(e.g. if you want to unwrap 4rlks interferogram), SNAPHU options and so on. An example of the parameter file is included in the package. Now the code supports roipac and NSBAS formats. User can easily extend to a new format. The code also requires a utilities library which has been included in the package.

5. **APS & Ramp Removal Wrapped (used in chapter 5)**

This python code is used to remove elevation correlated atmospheric delay as well as any global 2D polynomial (first or second order) ramp within wrapped interferogram. To remove these noises before unwrapping, it can potentially improve the quality of phase unwrapping.

Users need to have roi_pac format flattened and multi-looked interferograms.